ELECTRICAL CHARACTERIZATION OF GRAPHENE CHEMICAL SENSORS

by

JongBong Nah
A Dissertation
Submitted to the
Graduate Faculty
of
George Mason University
in Partial Fulfillment of
The Requirements for the Degree
of
Doctor of Philosophy
Electrical and Computer Engineering

Committee:

_____ Dr. Rao V. Mulpuri, Dissertation Director

_____ Dr. Qiliang Li, Committee Member

_____ Dr. Alok Berry, Committee Member

_____ Dr. John A. Schreifels, Committee Member

_____ Dr. Monson H. Hayes, Department Chair

Date:_____ Summer Semester 2022
George Mason University
Fairfax, VA

Electrical Characterization of Graphene Chemical Sensors

A Dissertation submitted in partial fulfillment of the requirements for the degree of Doctor of Philosophy at George Mason University

by

JongBong Nah
Master of Science
Old Dominion University, 2012
Bachelor of Science
George Mason University, 2007

Director: Rao V. Mulpuri, Professor
Department of Electrical and Computer Engineering

Summer Semester 2022
George Mason University
Fairfax, VA

DEDICATION

I dedicate this dissertation to my parents Pyung Kyoon Nah, Keum Ja Nah, Min Ji Kang's family and lastly, my lovely wife Sara Park, for their love, endless support, and encouragement.

ACKNOWLEDGEMENTS

I would like to express my sincere gratitude to many people who helped me during the period of my PhD studies. Foremost, I am very grateful to Dr. Rao Mulpuri for giving me the opportunity to pursue PhD under his supervision. His extremely supportive and encouraging nature has given me immense confidence in successfully completing this project. Special thanks to Dr. Alok Berry and Prof. Qiliang Li Wright for their constant guidance and support throughout my PhD work. I feel extremely fortunate to have worked with the finest advisor that one could possibly hope for.

A big thank you to our collaborators at U.S. Naval Research Laboratory (NRL). In particular, I am grateful to Dr. Evgeniya Lock for giving me the opportunity to have a great experience at NRL. It was a great pleasure and a wonderful experience working with some of the eminent scientists in the field of graphene research.

During my stay at NRL, there were several people who helped me in successfully completing this experiments. Especially, I would like to give my sincere appreciations to Dr. Keith Perkins. Thank you for your inexhaustible patient and support in both my professional and personal development, without his motivation and encouragement I would not have managed this research project. A special acknowledgement is due Dr. Rachael Myers-Ward, Dr. Anindya Nath, Dr. Anthony Boyd, Dr. David Kurt Gaskill, Dr. Michael Osofsky and Jenifer Hajzus.

Finally, I am short of words to express my deepest gratitude to my family, friends and my wife, whose continuous love, sacrifice, support, and encouragement have allowed me to pursue my ambitions.

TABLE OF CONTENTS

LIST OF TABLES

LIST OF FIGURES

ABSTRACT

ELECTRICAL CHARACTERIZATION OF GRAPHENE CHEMICAL SENSORS

JongBong Nah, PhD

George Mason University, 2022

Dissertation Director: Dr. Rao V. Mulpuri

Chemiresistive graphene sensors are promising for chemical sensing applications due to their simple device structure, high sensitivity, potential for miniaturization, low-cost, and fast response. The graphene films used in this work were grown on the Si face of semi-insulating, on-axis 6H-SiC substrates by Si sublimation at high temperature in a chemical vapor deposition reactor. The graphene films were used to fabricate devices with different geometries using oxygen plasma etching, followed by e-beam evaporation to form Ti/Au (10 nm/100 nm) contacts. The geometries included engineered defects of different sizes and shapes. The engineered defects of interest include 2D patterns of squares, stars, and circles, and 1D patterns of slots parallel and transverse to the contacts. The films were functionalized using N-ethylamino-4-azidotetrafluorobenzoate (TFPA-NH2) as a chemical linker, then zinc oxide nanoparticles (50 – 80 nm) were attached.

In this study, first, the resistance and low frequency noise of devices were measured with and without ZnO nanoparticle functionalization. We find that, relative to pristine

graphene devices, ZnO nanoparticle functionalization leads to reduced contact resistance but increased sheet resistance. In addition, in general, functionalization lowers $1/f$ current noise on most of the devices. The strongest correlations between noise and engineering defects, where normalized noise amplitude as a function of frequency f is described by a model of $A_N f^{-\gamma}$, are that γ increases with graphene area and contact area, but decreases with device total perimeter, including internal features. We did not find evidence of a correlation between the scalar amplitude, A_N, and the device channel geometries. In general, for a given device area, the least noise was observed on the least-etched device.

In this work, the detection of decane, propyl benzene, thiophene and octanethiol by graphene-based sensors functionalized with and without ZnO has been extensively studied by modeling of devices with first-principles calculations based on density functional theory (DFT). The electronic properties of the pristine graphene and ZnO functionalized graphene were investigated in terms of the total density of states (TDOS) and projected density of states (PDOS). The simulation results showed that ZnO functionalized graphene provides a more energetically favorable surface for the adsorption of thiophene and octanethiol than the pristine graphene.

In this work, the sensing properties of the devices were investigated for the decane, propyl benzene, thiophene, and octanethiol with and without ZnO nanoparticle functionalization. The ZnO functionalized devices showed the strongest response to thiophene and octanethiol vapor compared to the pristine graphene devices. Additionally, engineered defects onto graphene showed a marked improvement in sensitivity to thiophene and octane thiol vapors compared to unpatterned graphene. Furthermore, neither

the pristine nor ZnO functionalized graphene sensors demonstrated significant response to decane or propyl benzene vapors. Based on these results, graphene sensor devices (with and without functionalization) were sensing chemicals that have sulfur atoms (S) rather than hydrocarbon molecules (C and H). There is no strong evidence of a correlation between the conductance and the device active (graphene) area or the contact area. On the other hand, we do see strong correlation and inverse correlation between the perimeter and conductance. As a result, engineered defects and functionalization with metal oxides significantly enhance the performance of graphene chemical vapor sensors.

In high noise environments, acquiring sensor measurements accurately is difficult, especially when signals are weak compared to the noise levels. In these cases, linear filtering is not an appropriate technique for processing the signal and unique methods should be considered for extracting signal data. In this work, a simple and portable analog lock-in amplifier (LIA) circuit is designed for gas sensing. The LIA uses the phase detection (PD) technique to single out the data signal at a specific frequency. In PD-based techniques, signals at frequencies other than the reference signal are rejected and, therefore, do not influence the required signal data significantly. For the LIA, the reference sensor excitation is a 2 KHz 70 mV_{rms} sinusoidal signal from the function generator, which is a part of the designed circuit. A low pass filter (LPF) after the PD circuit was then used to cancel high frequency noise and extract the absolute mean value of the data signal. In this work, PSPICE simulations were carried out using actual commercial IC models. This LIA circuit design enables one to acquire sensor measurements accurately in extremely noisy environments.

CHAPTER 1 : INTRODUCTION

1.1 Allotropes of Carbon

Carbon is one of the most abundant elements in the universe and is responsible for the formation of all organic structures, including the naturally occurring life on Earth. There are over 95% of known chemical compounds made of carbon, where carbon can form bonds with electronegative and electropositive atoms [1-2]. The carbon atoms possess an exceptional versatility in bonding among themselves, even without interaction with other elements, resulting in many interesting allotropes. Two of the most well-known carbon materials, graphite and diamond, give an excellent demonstration of how different bonds can be made by this element [1-2]. Although they contain the same element, these two materials exhibit substantially different chemical, electrical, and mechanical properties. Diamond, for example, is transparent, electrically insulating, and one of the strongest materials ever discovered. Graphite, however, is opaque, highly conductive, and among the softest materials. The differences in properties between these materials, despite being made from the same element, are due to the different arrangements of the carbon atoms. Several other carbon allotropes (materials entirely composed of carbon atoms) have been discovered recently, which differ from one another only by the way the carbon atoms are arranged [3]. In terms of their hybridization of carbon atomic orbitals, there are three types of carbon allotropes [4]. Diamond materials are formed when all carbon atoms are

bonded in a sp^3 hybridization, while graphitic materials are formed when all carbon atoms are bonded together in sp^2 hybridization. Amorphous carbon is third type of carbon allotrope, which is composed of mixtures of sp^2 and sp^3 hybridized carbon atoms. Figure 1.1 provides a schematic representation of the different allotropes of carbon. Despite their interest, diamond and amorphous carbon are only mentioned briefly in this chapter and are not examined further.

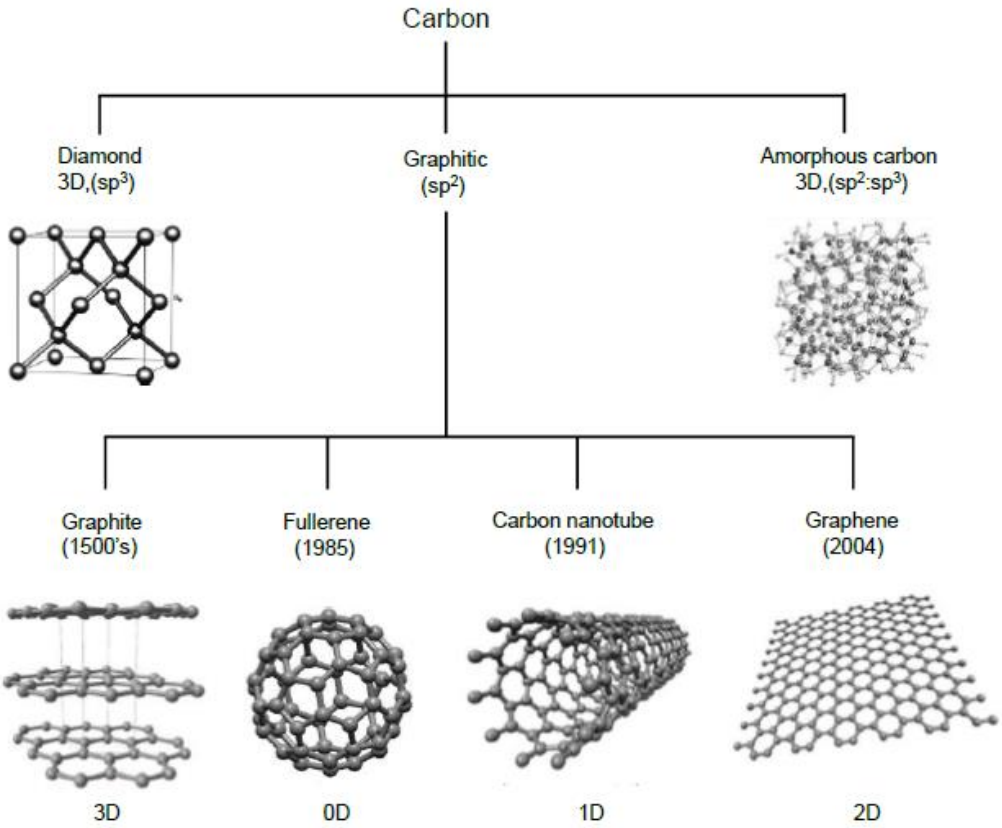

Figure 1.1: The dimensionality and hybridization of the various carbon allotropes as shown in this diagram [9].

1.2 Graphitic Materials

A graphite is a special type of allotrope with sp^2 hybridized carbon atoms as mentioned before. These materials can be in any dimensional form, from zero-dimensional fullerene to three-dimensional graphite. These are commonly called graphitic materials since graphite is the most famous and best-known representative [4].

1.2.1 Graphite

In the early 1500's, graphite was discovered as a naturally occurring allotrope of carbon [5]. As shown in the Figure 1.1, graphite is composed of hexagonal rings of covalently bonded carbon atoms stacked on top of one another. These hexagonal carbon planes are bonded together by weak Van der Waals forces, which allow the in-plane bond strength to be several orders of magnitude greater than the interlayer bonding. As an example, the in-plane bond length for carbon atoms is 1.42 Å, while interlayer carbon bonds are 3.35 Å [5]. Graphite layers can slide over each other due to the weak bonding between interlayer carbon atoms, making it useful for applications such as pencil leads and lubricants [6]. The material is also used in nuclear reactors to control the fission reaction speed as well as an electrode for batteries [7].

1.2.2 Fullerene and Carbon Nanotubes

Kroto *et al*. discovered fullerene (C_{60}), also known as buckyballs or buckminsterfullerene, in 1985 and were awarded the Nobel Prize in chemistry for their work in 1996 [8]. A fullerene is a zero-dimensional molecule with discrete quantum states

in which the carbon atoms are organized into a hollow sphere with hexagonal and pentagonal rings as shown in Figure 1.1 [9]. The carbon atoms are sp^2 hybridized in this structure. They are not arranged in a plane like in graphite. Fullerene's geometric structure strains its sp^2 hybridized carbon atoms, resulting in semiconducting or insulating properties.

The second carbon allotrope is the carbon nanotube (CNT), a hollow cylindrical structure formed by carbon atoms bonded together in a hexagonal arrangement, as shown in Figure 1.1 [10]. Despite the controversy surrounding the discovery of CNTs, Sumio Iijima is often credited with their official discovery in 1991 [11]. CNTs can be a single tube called a single-walled nanotube (SWNT), or they can be two or more concentric tubes stacked one inside the other, referred to as multi-walled nanotubes (MWNTs). Quantum states in CNTs are restricted in such a way that electrons can only travel in one dimension, so they can be considered one-dimensional materials. [10-12].

1.2.3 Graphene

The newly discovered allotrope of carbon is a material called *graphene*, in which each carbon atom is bonded to three others to form a honeycomb-like structure as shown in Figure 1.1 [13]. Graphene has a number of unusual properties and plays an important role in understanding the properties of other carbon allotropes. For example, as shown in Figure 1.2, graphene sheets can be stacked upon each other to generate graphite, whereas fullerenes can be created from graphene by curling it up with the introduction of pentagons in a systematic way. The CNTs can be made by rolling up a graphene sheet along a certain

direction. [14]. In spite of the fact that graphene is the mother of all these allotropes, it is the last material that was discovered in the carbon family which gives access to all dimensions. Due to graphene's two-dimensional structure, it has been widely believed that single layer could not exist in a freestanding state [15].

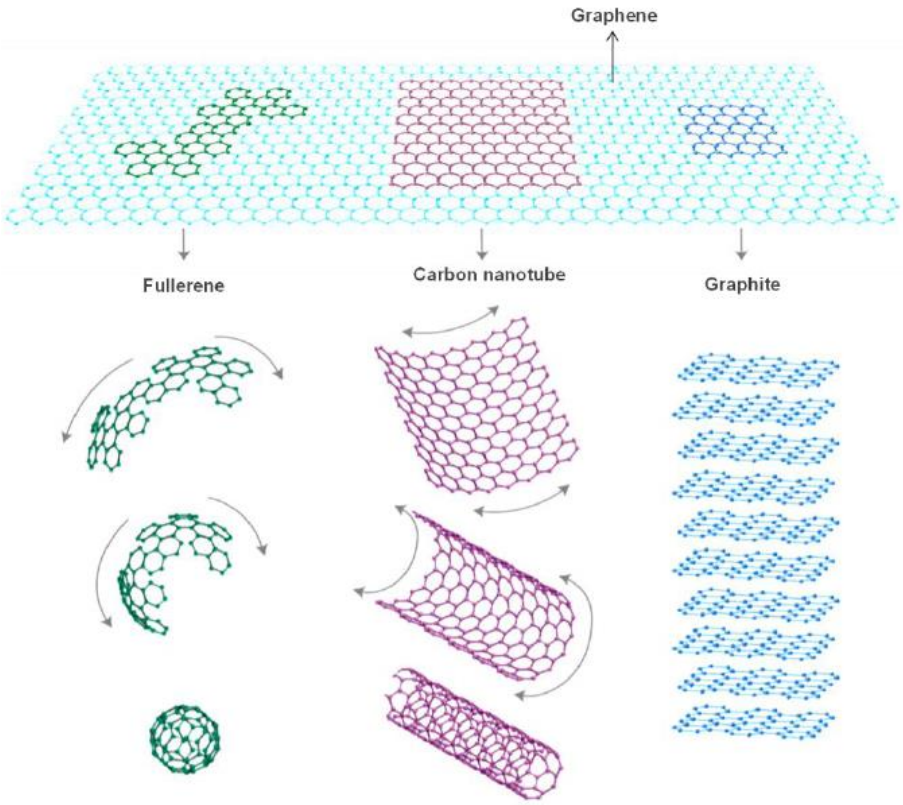

Figure 1.2: All the graphitic carbon allotropes of different dimensions are composed of graphene hexagonal nanosheets [14].

1.3 Motivation: Increasing Market and Potential of Graphene Research

In modern age, semiconductors are the backbone of electronic devices such as transistors, solar cells, diodes, and for making various digital and analog integrated circuits [16-17]. The incessant research on semiconducting materials and fabrication processes resulted in constant progress in the complexity and therefore the speed of semiconductor devices, an impact referred to as Moore's Law [18].

The ease with which its properties can be tuned, its easy fabrication processes, and its abundance have positioned silicon as the most widely used material for semiconducting device applications [18-19]. However, scientists and researchers in the electronics industry are looking for other materials as the potential market for electronics is ever growing. Electronics in papers, walls and clothing are limited simply because silicon cannot easily be painted on a surface, wrapped on a flexible platform, or used to cover large areas. The technology we need is something that can be similar to silicon, which can be produced efficiently and inexpensively at large scale. Graphene, an atom thick layer of carbon atoms, is growing as a promising candidate in semiconductor industry due to its unique physical and electronic properties [20]. The material, graphene, cannot replace the silicon dynasty on its own, but it can be developed as a supplement to silicon by mixing with silicon in the manufacture of some multi-purpose devices for which silicon is insufficient.

Since 2004, graphene has become one of the most research materials for its synthesis, modification, and applications in many fields. This is due to its outstanding overall properties, such as, single-atom thick two-dimensional conjugated structures, room-temperature stability, ballistic transport, and large available surface areas [21-26].

Graphene can serve as an ideal platform to carry other components for specific roles, because of its special structure. The high conductivity and ballistic transport capacity ensure that graphene exhibits very little signal noise when acting as a sensor [27]. It does not require an auxiliary electrical heater due to its excellent chemical stability at room temperature [27]. All of these characteristics of graphene benefit its sensing properties, making it an ideal candidate for gas/chemical detection. Therefore, great efforts have been made in the research of graphene-based chemical/gas sensors, resulting in a giant leap forward in the development of graphene-based chemical sensing devices. We can clearly see that the number of published papers on graphene-based gas/chemical sensor has sharply increased over the period from 2007, as shown in Figure 1.3.

However, despite its great potential as a sensing material, graphene still faces a number of challenges such as homogeneity, large areas, integration of devices, and selective sensor mechanisms. Since its discovery, many efforts have been made to improve its quality and synthesize a homogeneous large area layer [28-30], and more recently, there have also been efforts to functionalize graphene with various elements to improve its sensitivity, selectivity, solubility, and loading capacity [31-38].

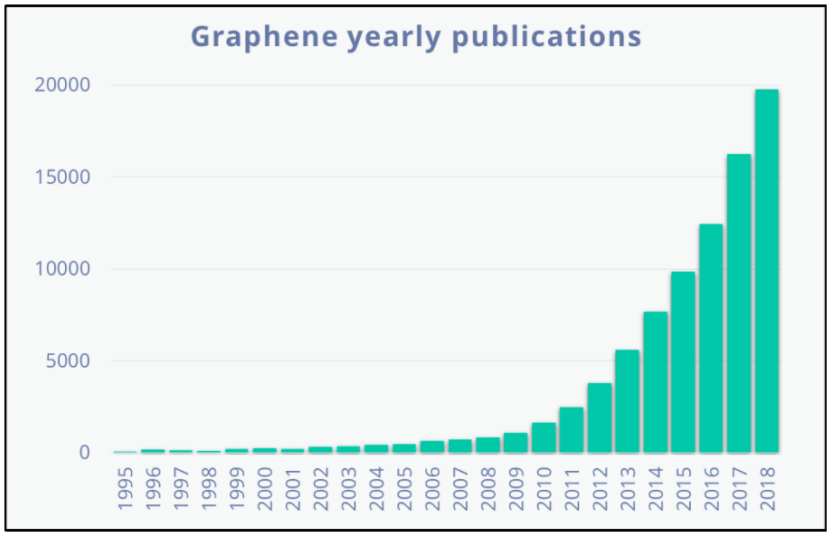

Figure 1.3: The number of scientific articles published per year containing the keyword graphene. Data was collected from *www.sciencedirect.com* on 2nd Nov. 2018.

1.4 Importance of Graphene Based Gas/Chemical Sensors

A variety of serious environmental problems have been attributed to modern advanced technology and industrial development. As an example, the release of various chemical pollutants such as NO_X, SO_X, CO_X, and volatile organic compounds (VOCs) into the atmosphere from various manufacturing industries. Atmospheric pollution can cause serious problems related to human health. For example, it can trigger an illness like asthma.

Acid rain is another example of the consequences of air pollution. Any industrial and private activities lead to the emission of nitric acid and (NO_X) sulfuric acid (SO_X) is the cause of acid rain. As a result, buildings get eroded, water gets contaminated and vegetation is affected, which in turn affects human health [39]. Besides air pollution, release of combustible gases like methane, ethane, butane, hydrogen, and acetylene can

also result in significant explosion risks [40-41]. It is therefore imperative to develop new sensors and technologies to detect and quantify environmental pollutants, particularly toxic and combustible gases, so as to minimize the above mentioned consequences [42].

Gas/chemical sensors have become essential in today's technology-driven society and are used in a wide variety of applications, such as environmental, biomedical, chemical processing, pharmaceuticals, industrial safety, indoor monitoring, and food [43]. Sensors have benefitted from the advances of computers, integrated electronics, new materials, novel designs, and processing tools [44]. Such technological changes can be seen in the development of miniaturized, low-cost, portable, and mass-manufacturable gas/chemical sensors capable of static and continuous measurements even in remote locations [45]. Gas/chemical sensor devices allow the conversion of a chemical or physical property of a specific analyte into a measurable signal whose magnitude is normally proportional to the concentration of the analyte [46]. A typical chemical-sensing system can identify harmful substances and transmit a series of audible and visible warnings, such as flashing lights and alarms, when dangerous levels are detected. The important performance characteristics of a gas/chemical sensor are briefly described below.

- Limit of detection (LOD) - the lowest concentration of the analyte that can be detected by the sensor under given conditions.
- Working temperature – the temperature at which the sensor operates.
- Sensitivity – the change of measured signal per one-unit change in analyte concentration in input, i.e., the slope of a response vs. concentration plot.

- Selectivity – sensor's ability to discriminate between the analytes of a gas mixture and provide detection signal for the target analyte of interest.
- Response time – the time to reach 90% of the final value during analyte exposure.
- Recovery time – the time to reach 10% of the final value during room temperature clean air exposure after it was subjected to analyte exposure.
- Dynamic range – the analyte concentration range between the detection limit and the highest limiting concentration.
- Reliability – the ability of devices to withstand exposure to extreme temperatures, transitions between temperature extremes and excessive humid conditions.
- Stability/Reproducibility – the ability of a sensor to provide reproducible results for a long period retaining the sensitivity, selectivity, response, and recovery time.

For chemical sensors to be successful in real life, sensor devices must be able to demonstrate high sensitivity, strong selectivity, outstanding stability, fast response and recovery times, a very low detection limit, a wide dynamic range, and low costs, along with high resolution and reliability.

1.5 State-of-the-art of Graphene Based Gas/Chemical Sensors

Monitoring harmful gases and chemicals in the environment without the involvement of humans is possible with chemical sensors [47-48]. Chemical sensors work on the principle of analyte molecules adsorbing and desorbing on the sensor surface [48]. Analyte molecules adsorbed on a sensor material usually disrupt its fundamental property

by forming a physical bond or a chemical bond. This results in a change in conductivity, resistance, or capacitance of the material. A highly sensitive and selective sensor material is required to detect such changes, particularly those of low analyte concentrations. The materials must also be inexpensive to operate, easily integrated and, most importantly, compatible with existing fabrication techniques.

Schedin *et al*. [49] first demonstrated the chemical sensing behavior using mechanically exfoliated graphene as shown in Figure 1.4(a). A change in resistivity of graphene was observed after graphene was exposed to different gaseous species including NO_2, NH_3, H_2O, and CO. However, the magnitude of the change and its polarity were found to be strongly dependent on the properties of the gas analytes. The resistivity of graphene increased immediately upon exposure to NH_3, followed by the saturation region (region II). When the chamber was evacuated, a very slow and small change (region III) in resistivity was observed, which indicated that the gas molecules still stick to the graphene surface. However, by annealing at 150˚C under vacuum these devices restored to their original state (region IV). Exposure to NO_2, On the

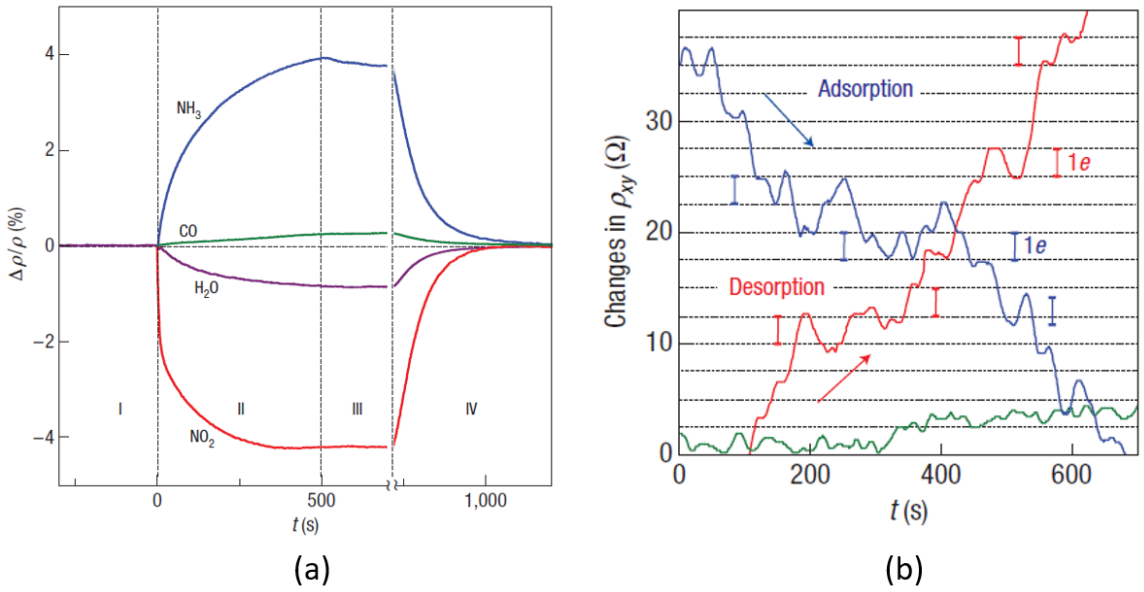

Figure 1.4: (a) Response of exfoliated graphene sensor to electron donating and electron withdrawing gas analytes and (b) monitoring the single molecule detection of NO_2 during adsorption and desorption from the graphene surface. The green curve is the reference [49].

other hand, resulted in a dramatic decrease in graphene sheet resistance, as well as regions of saturation by an adsorbate (region II), slow recovery (region III), and recovery induced by annealing (region IV). An increase or decrease in resistivity corresponds to the electron donating or withdrawing behavior of NO_2 and NH_3, respectively. In addition to these species, H_2O acted as an acceptor, whereas CO and ethanol showed electron donating behavior. This change in carrier type and carrier density is the basic mechanism that governs the operation of all conductivity or resistivity based graphene chemical sensors.

Under the same exposure conditions, simultaneous Hall measurements demonstrated linear relationships between the change in carrier density (Δn) and analyte concentration. However, surprisingly, despite the presence of extra charge carriers, no

degradation in Hall mobility was observed even for carrier densities exceeding 10^{12} cm^{-2}. It contrasts to conventional two-dimensional systems, in which such high densities of charge impurities were found to be detrimental for the ballistic transport. Long term experiments with extremely diluted NO_2 gas showed a distinct and discrete step like changes in resistivity (Figure 1.4(b)), corresponding to single molecules of the gas adsorbing and desorbing from the graphene surface. Such ultra-low detection of gas molecules has sparked immense interest in developing graphene sensors for a wide range of applications.

Pearce *et al.* [50] performed one of the first investigations on the sensing behavior of epitaxial graphene grown on SiC. In particular, the effect of graphene thickness on the response of the sensor to NO_2 gas was investigated at different operating temperatures. When a multi-layer graphene (MLG) based sensor was exposed to NO_2 gas, resistance decreased at all measured temperatures (25˚C to 100˚C). In spite of this, the recovery time was significantly longer when the highest test temperature was used (100˚C), indicating that a strong chemical bond was formed between the adsorbed molecules and the graphene surface. In addition, a significant shift in the sensor base line was also observed while the sensor was in operation, as shown in Figure 1.5(a). The response of the MLG device for NO_2 was several orders of magnitude smaller than the response of the single-layer graphene (SLG), which was thought to be related to the screening effect, where current flows through non-exposed carbon layers in the MLG sensor. In Figure 1.5(b), upon exposure of the SLG device to NO_2 a decrease in resistance, indicating the device has a majority hole carriers (p-type material), is observed at all attempted temperatures and concentrations.

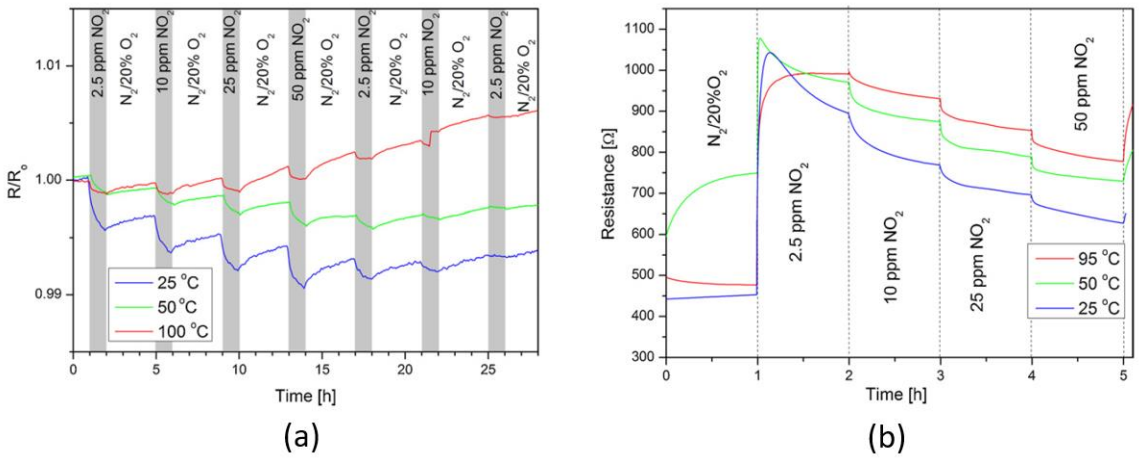

Figure 1.5: (a) Electrical response of multi-layer graphene sensor toward NO_2 at different temperatures and (b) response of single layer graphene to the same gas analytes [50].

Many researchers have reported a significant increase in the sensing ability of graphene via surface functionalization [51-55]. The surface of graphene was functionalized with catalytic metals such as platinum (Pt), Palladium (Pd), and Gold (Au). Johnson *et al.* reported the ammonia (NH_3) sensing behavior of graphitic nanoribbons decorated with platinum nanoparticles [51]. Chu *et al.* used platinum decorated graphene surface to detect H_2 gas in different concentrations [55]. In their study, they observed that when graphene is decorated with platinum nanoparticles, it acted as dopant and increased the conductance of graphene. Other than surface functionalization, the effects of different metal contacts on gas sensing behavior for different types of oxidizing and reducing gas sensing have also been discussed. For example, Pd/Au electrode was investigated on graphene for sensing NO_2 by G. Ko *et al.* [56]. The sensitivity was around 9% for 100 ppm of NO_2 gas for few-layer graphene. Nomani *et al.* used Pt/Ti contact to enhance the selectivity towards NO_2

gas [57]. The NO_2 was detected at a low concentration in the presence of commonly interfering gases such as CO_2, H_2O (saturated vapor), NH_3 (550 ppm), and O_2.

In addition to the graphene functionalization with catalytic metals, graphene functionalization with metal-oxide nanoparticles has been widely employed in industry for chemical sensing applications [58]. The metal oxide nanoparticles can improve the adsorption of chemical species by providing more adsorption sites, enhancing the sensitivity and selectivity of the sensors [59]. The copper oxide nanoparticles (CuO NPs) have attracted great attention due to high electrocatalytic activity property [60-62]. These characteristics make CuO NPs suitable for high performance gas sensing application. The Iron (III) oxide nanoparticles (Fe_2O_3 NPs) which are nontoxic, have outstanding thermal stability have also been used for gas sensing application [63-66]. The Indium tin oxide nanoparticles (ITO NPs) have an n-type semiconducting behavior with a band gap energy of 3.5 – 4.06 eV and has been used for gas sensor application [67-69]. Lastly, the Zinc oxide nanoparticles (ZnO NPs) are appropriate for chemical sensing applications because they are less toxic, optimally conductive, low cost and come in a variety of morphologies [70-72]. They have demonstrated excellent chemical sensing properties [70-72].

Based on all these reports, the resistance change approach (based on the change in conductivity) may be useful in developing graphene-based sensor devices that can detect very low concentrations of target gases. Rymnesteve *et al*. [73] however, used a different technique to understand the sensing mechanism of graphene. They evaluated the sensing response of pristine graphene to a wide range of organic chemicals using low-frequency noise measurements along with resistance measurements. As can be seen in the Figure 1.6(a),

different chemicals produced different noise characteristics (i.e., Lorentzian noise bulges), particularly at low-frequencies (< 100 Hz) that are specific to a chemical type. The noise bulges can be seen more clearly in Figure 1.6(b), where ethanol vapor had a distinctive characteristic noise frequency of 400-500 Hz, when compared with tetrahydrofuran which has a typical noise frequency of 10-20 Hz. The combination of noise measurements with resistance measurements can allow us to derive an understanding of the sensing mechanism behind graphene-based chemical sensors.

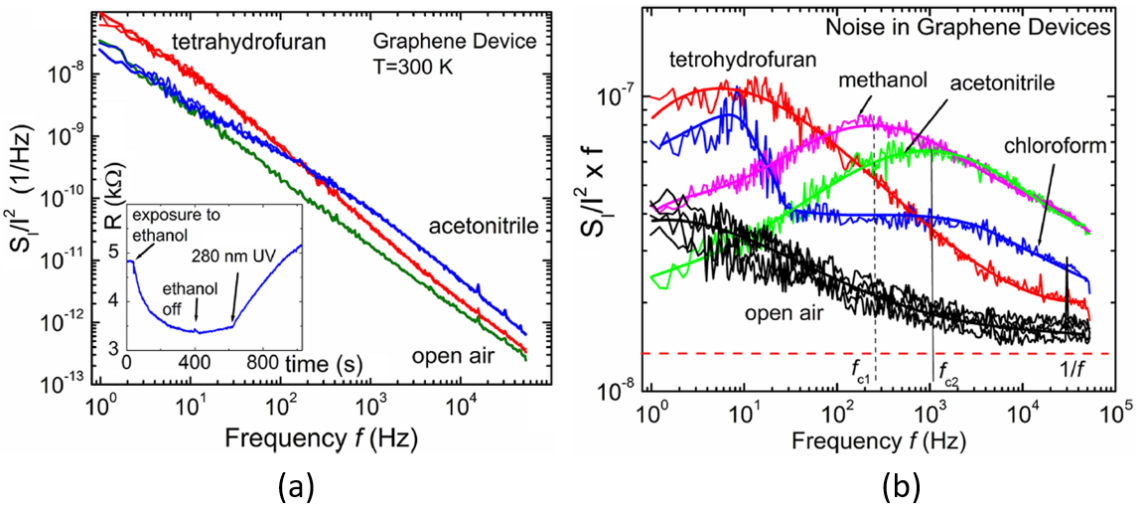

Figure 1.6: (a) 1/*f* noise deviation and appearance of bulges after exposure of different chemical vapors and (b) more pronounced effect of 1/*f* noise bulges showing different characteristics frequencies for different chemical species [73].

1.6 Chapter Outline of the Dissertation

This dissertation is structured into seven chapters, with the first chapter being this introduction. In Chapter 2, a brief background on the electronic and structural properties

of graphene is presented along with the review on different methods used for the graphene synthesis. The influence of metal contacts on the electrical properties of graphene devices, the significance of graphene surface functionalization for the development of graphene based chemical sensors and different types of electrical noise are discussed in detail. In Chapter 3, device resistance and low frequency electrical noise measurement results obtained in this work on the pristine graphene and the ZnO nanoparticle functionalized graphene are presented for different device geometries. In Chapter 4, design and computation of molecular models of graphene and metal-oxide nanosheet using density functional theory (DFT) are presented. The computational methods are discussed in detail. The adsorption properties of target gases (decane, propylbenzene, thiophene, and octanethiol) including adsorption configurations and energetics have been studied. The electronic structure of the designed sensors before and after target gas adsorption have been demonstrated and analyzed. The DFT results are compared with the experimental results in this chapter. In Chapter 5, results on pristine graphene and ZnO functionalized graphene chemiresistive sensor devices with different geometries exposed to vapors of decane, propylbenzene, thiophene, and octanethiol are presented and discussed. In Chapter 6, simple and portable analog lock-in amplifier (LIA) circuit is designed for gas sensing application. In this work PSPICE simulations were carried out using actual commercial IC models. Finally, Chapter 7 the key conclusions from the results of this work are presented. In addition, a future outlook on the development of graphene chemical sensors and the strategies required for the commercialization of graphene sensor technologies is discussed.

CHAPTER 2 : BACKGROUND INFORMATION

2.1 Introduction

Graphene has been attracting enormous scientific attention from physicists, chemists, material scientists and engineers due to its wide range of potential applications. The term *graphene* was first defined as individual carbon layers in graphite intercalation compounds in 1994 [74]. Graphene had been studied theoretically in band structure calculations as a single layer of graphite long before the name was given to it [75]. Furthermore, Peierls and Landau showed that thermal fluctuations in low-dimensional crystals cause atom displacements comparable to interatomic distances at arbitrary temperatures, resulting in thermodynamic instability and eventually curling into carbon soot [76]. In experiments, the only trace of graphitic layers was found on the surface of SiC after the substrate was heated in vacuum [77-80]. In spite of the fact that graphite is technically composed of monolayers of hexagonally arranged carbon atoms, or graphene, it was long believed that such a 2D crystal was thermodynamically unstable and therefore impossible to isolate experimentally [81-82]. In 2004, Manchester University researchers became the first to isolate monolayers of graphite using a mechanical exfoliation method at room temperature [13]. A single layer of graphene is formed using adhesive tape repeatedly peeling of carbon layers from highly oriented pyrolytic graphite, which they then transferred to a SiO_2/Si substrate. Graphene is not only the first truly two-dimensional crystalline material to be discovered but also is the thinnest material, being one atom thick. Monolayer and few-layer graphene have been identified by optical and atomic force

microscope (AFM) imaging techniques [13]. In 2010, Andre Geim and Konstantin Novoselov, the leaders of the University of Manchester team, were awarded the Nobel Prize in Physics, and their work became the basis for an intensive period of graphene research. It was less than a year after their initial discovery that Geim and Novoselov achieved the first electrostatic transport measurement on monolayer graphene, and observed a similar behavior as that seen in few-layer graphene [83]. The discovery of this two-dimensional material led to the discovery of many other materials, including molybdenum disulfide (MoS_2), boron nitride (BN), tungsten disulfide (WS_2), molybdenum diselenide ($MoSe_2$), tungsten diselenide (WSe_2), and many more [84]. Even though they all possessed intriguing properties, none of these materials received the same level of attention or interest as graphene.

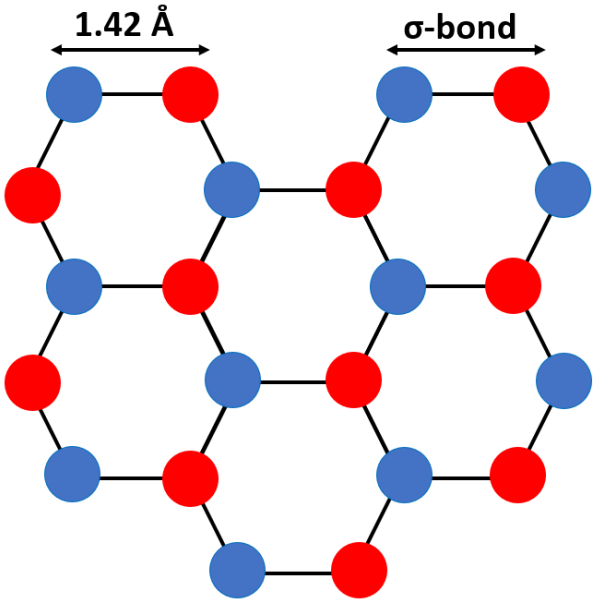

Figure 2.1: Illustration of the hexagonal lattice of graphene.

Graphite is made up of a periodic arrangement of individual graphene layers stacked into a hexagonal structure held together by van der Waals forces with an interlayer spacing of 3.4 Angstroms (Å). Graphene or single layer graphene (SLG) or monolayer graphene all represent one sheet of sp^2 bonded carbon atoms, in which each carbon atom is covalently bonded to three nearest neighboring atoms in the plane with a C-C distance of 0.142 nm to form a hexagonal lattice structure, as shown in the Figure 2.1. Two layers of graphene are present in bilayer graphene (BLG), while three layers of graphene are present in trilayer graphene (TLG). A few layer graphene (FLG) represents a stack of four to five layers of graphene, whereas a multilayer graphene (MLG) is composed of six to ten layers of graphene. The term pristine graphene in this thesis refers to graphene in an undoped, unstrained, and unperturbed state.

2.2 Graphene Properties

It is remarkable that graphene, despite its simple structure, exhibits a range of material properties that surpass any other material that has been measured so far. Due to the strong covalent bonds between the in-plane carbon atoms of the graphene sheet, graphene has exceptional mechanical strength to the point that it is stronger than diamond at the same thickness with a Young's modulus of 1 TPa and an intrinsic strength of 130 GPa [85]. In addition to its hardness, it is the only crystal which can be elastically stretched by 20% in one dimension without breaking [85]. Furthermore, graphene has the advantage of being highly transparent (97.7%) [86], while it is also so dense that not even helium atoms can pass through it [87]. Graphene's two-dimensional nature also makes it an ideal material with the largest specific surface area, as high as 2630 m^2/g [88]. Graphene also

has an exceptionally high thermal conductivity of up to 5000 W mK^{-1} [89], which is better than CNTs (3500 W mK^{-1}) and diamond (2500 W mK^{-1}), while its electrical resistivity of 1.0×10^{-6} Ω-cm is better than well-known conducting materials such as Ag (1.59×10^{-6} Ω-cm) and Cu (1.68×10^{-6} Ω-cm) [90]. Graphene is currently being investigated for resistance standard measurements in metrology, where graphene grown on SiC has been found to have superior resistance accuracy than conventional GaAs heterostructures [91]. When it comes to carrier mobility, graphene is by far the best material with a mobility of over 200,000 cm^2 V^{-1} s^{-1} at room temperature [92-93].

2.3 Electronic Structure of Graphene

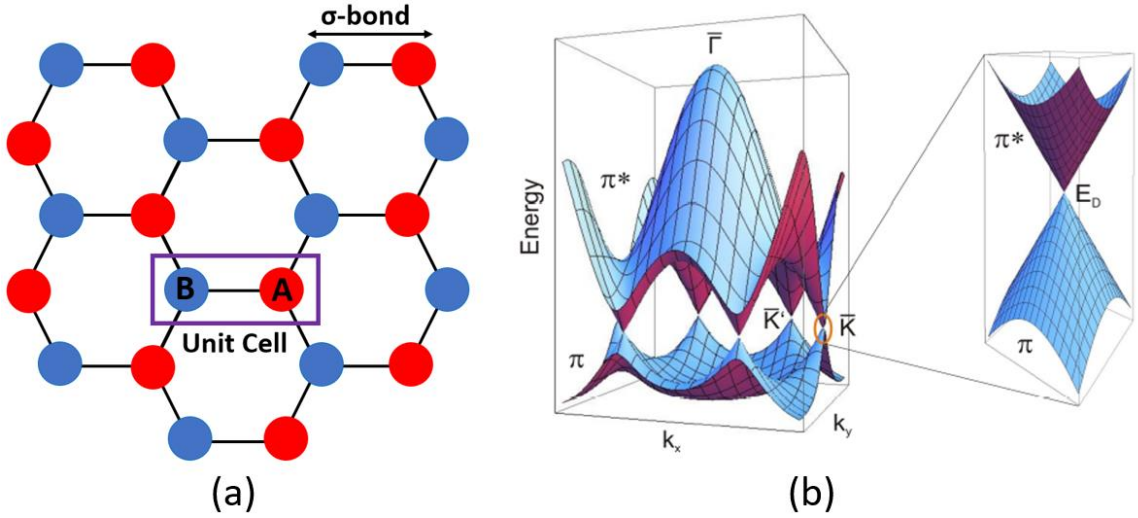

Figure 2.2: Illustration of (a) the hexagonal lattice structure of graphene showing unit cell with two carbon atom A and B. (b) Electronic band structure of graphene, obtained using a tight-binding approximation for nearest neighbor hopping only [95].

The remarkable properties of graphene, particularly its electronic properties are due to its honeycomb structure and exhibit a basis with two carbon atoms A and B per unit cell as shown in Figure 2.2(a). There are four valence electrons on the carbon atom, of which three are bonded to three nearest neighboring carbon atoms by strong σ (sigma) bonds. While electrons in these bonds do not contribute to electron transport, they do provide the graphene sheet with a remarkable mechanical strength. All of the unusual electronic properties of graphene arise from the fourth valence electron. In the graphene plane, this conduction electron oscillates up and down perpendicularly to produce a p_z orbital. Due to the short bonding distance between the carbon atoms, the p_z orbital of one carbon atom is overlapping with the p_z orbital of a neighboring carbon atom leading to delocalized electron π-bands [94]. As shown in Figure 2.2 (b), a tight-binding calculation can be used to address the electronic properties of graphene by calculating the π-band structure. Even though graphene was discovered in 2004, Wallace *et al.* [95] calculated the electronic band structure as early as in 1947. The calculation of the band structure in Figure 2.2(b) indicates an unusual structure in which the lower valence band (π) and the upper conduction band (π*) meet at the K and K′ points. This crossing point is called the Dirac point (E_D). An undoped graphene has the Fermi energy (E_F) exactly located at E_D, where both the conduction and valance bands overlap smoothly without repulsion or bandgap opening. Thus, graphene is usually described as a semiconductor with a zero bandgap, or to be more precise, as a semi-metal [96]. As can be seen in Figure 2.2(b), π-bands exhibit linear dispersion around the E_D with an energy $E = \hbar v_F|k|$, where ħ is Planck's constant, v_F is Fermi velocity and k is the wave vector measured from K. Unique to graphene and one of the

reasons for graphene's high charge carrier mobility is Fermi velocity, $\nu_F \sim 10^6$ m/s, which is constant for charge carriers in graphene [97].

The linear energy dispersion quickly gives rise to an analogy with photons, massless elementary particles that travel with constant velocity and also exhibit a linear energy dispersion relationship [98]. This relationship leads to a stark difference in the way that charge carriers in graphene behave as compared to conventional metals and semiconductors. Thus, electrons in graphene exhibit the same behavior as photons or ultra-relativistic particles such as neutrinos with an energy-independent ν_F that is 300 times smaller than the speed of light [98]. Due to the absence of bandgap, graphene exhibits an ambipolar behavior, where the charge carrier can be continuously tuned between electrons to holes with carrier concentrations as high as 10^{13} cm^{-2}. The electronic properties of graphene also change dramatically as graphene thickness increases. Figure 2.3 shows an evolution of graphene band structures calculated using tight binding calculations for monolayer and few-layer graphene [97-99]. As can be seen in the Figure 2.3, the bilayer graphene exhibits parabolic bands that touch at the Dirac point, exhibiting the semi-metallic behavior similar to monolayer graphene. When it comes to trilayer or few layer graphene, the band structure

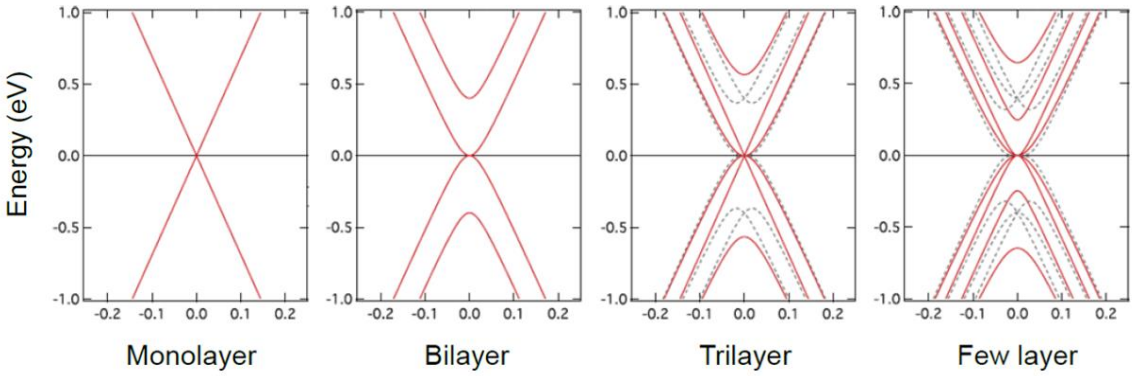

Figure 2.3: The band structure of graphene changes with increasing thickness [99].

is not only determined by the number of layers, but also by the sequence in which they are stacked. Every new layer adds two π-bands to the existing band structure, increasing its complexity and ultimately approaching the structure of graphite.

2.4 Synthesis of Graphene

Graphene has exceptional electrical properties that make it attractive for future applications in electronics, such as ballistic transistors, sensors, field emitters, integrated circuits (ICs) and transparent electrodes [100]. The majority of these interesting applications require single-layer graphene on a suitable substrate with a controlled and practical band gap, both of which are quite difficult to control and attain. Also, the development of graphene-based electronics is dependent on mass production of the material. There are several methods to produce graphene such as mechanical cleaving, mechanical and liquid-phase exfoliation, laser ablation and photo-exfoliation, chemical vapor deposition (CVD) on metal substrates, epitaxial growth on SiC, molecular beam

epitaxy (MBE) and metal-catalyzed crystallization of amorphous carbon [100-104]. Nevertheless, the majority of research attention has been focused on mechanical exfoliation, CVD graphene growth, and epitaxial graphene growth on SiC.

2.4.1 Mechanical Exfoliation

The process of mechanical exfoliation results in the highest quality graphene in terms of structural integrity and electronic performance. In this process, graphene is separated by peeling off a layer repeatedly from commercially available Highly Oriented Pyrolytic Graphite (HOPG) sheet by using scotch tape as shown in Figure 2.4(a) [105]. After they have been exfoliated, the graphene flakes are transferred onto SiO_2 surfaces for characterization and device fabrication. The thickness of these transferred graphene flakes

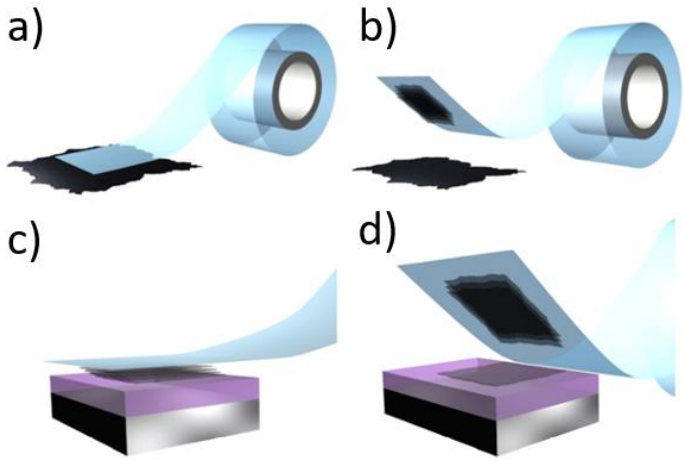

Figure 2.4: Illustration of the micromechanical exfoliation of 2D crystals. (a) Adhesive tape is pressed against a 2D crystal so that the top few layers are attached to the tape (b). (c) The tape with crystals of layered material is pressed against a surface of choice. (d) Upon peeling off, the bottom layer is left ono the substrate [105].

can be easily identified from the variation in contrast of different layers in an optical microscope.

The largest flake sizes are currently limited to millimeters [106] by this technique, so it is not suitable for large-scale industrial applications. Even so, the quality of graphene which is produced through mechanical exfoliation is superior to that produced by other methods. At room temperature, suspended single layer graphene devices achieve mobilities exceeding 200,000 $cm^2 \cdot V^{-1} \cdot S^{-1}$ [92-93], while as-fabricated unsuspended graphene devices are typically capable of mobilities ranging from 10,000 to 20,000 $cm^2 \cdot V^{-1} \cdot S^{-1}$ [107]. The ability to achieve excellent crystal quality as well as the low cost of producing flakes makes mechanical exfoliation the preferred method for research purpose to demonstrate proof-of-concept devices and to develop an in-depth understanding of chemical, electrical, mechanical, and optical properties of graphene.

2.4.2 Chemical Vapor Deposition (CVD) Growth on Metals

The Chemical Vapor Deposition (CVD) grown graphene on metal substrates is one of the most successful growth techniques developed for mass production. As a result of CVD, polycrystalline graphene is formed by decomposing a carbon precursor (methane or ethanol) at 1000º C and segregating carbon atoms on a foil of a transition metal with low

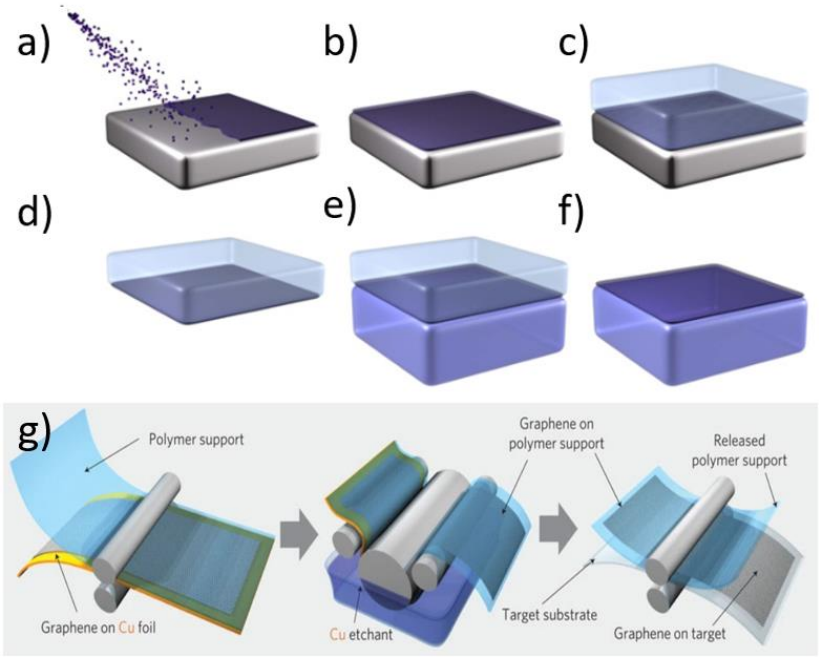

Figure 2.5: The transfer of chemical vapor deposition (CVD) grown 2D crystals. (a), (b) 2D crystals are grown by CVD on a surface of a metal. (c) A sacrificial layer (i.e., PMMA) is deposited on top of the 2D crystal. (d) The metal is etched away, leaving 2D crystal stuck on the sacrificial layer. (e) The sacrificial layer, together with the 2D crystal is transferred onto the substrate of choice. (f) The sacrificial layer is removed (g) Roll-to-Roll production of CVD graphene [105, 113].

solubility for carbon (in most cases, copper), with a smooth surface [108]. To make graphene usable, the metal substrate must first be separated. A transfer polymer, usually poly(methyl methacrylate) (PMMA) is spun on graphene to provide an alternative substrate. The metal substrate is then etched away, allowing graphene to be placed on any suitable substrate. The transfer of 2D crystals grown by CVD is shown in Figure 2.5 [105]. In some reports graphene is simply peeled from the metal using a poly(dimethyl siloxane) (PDMS) polymer, which allows further reuse of the metal substrate [109]. However, the

mechanical stress of the peeling process can cause damage to the graphene, especially if it is done by manual operation.

The growth of graphene has been demonstrated on a variety of metals, including Pt, Cu, Au, Rh, Ir, Ni, Co and Ru. [110-112]. The growth on Pt, Au, and Ir is relatively costly for commercial production, compared to metals like Ni and Co, therefore most studies were done on these metals. Furthermore, Ni and Co have less than 2% mismatches in their lattices with graphene. Yet, the thickness of graphene films grown on these metal films is highly variable and highly inhomogeneous. The major advantage of growing graphene on Cu is that the growth is self-limited, that is, it stops once the Cu surface is fully covered with graphene [108]. This technique leads to the formation of single layer graphene uniformly on a Cu surface, with only 5% of the surface containing bilayer or trilayer graphene. Obtaining such a controlled thickness over large area was mainly possible because of the low carbon solubility and mild catalytic activity of copper. Following the initial work, graphene growth on Cu was scaled up to an incredible 30 inches using roll-to-roll process as shown in Figure 2.5 [113]. A Cu based CVD growth method is attractive for mass production due to the relatively cheap nature of Cu, as well as the high yield of reasonably good quality graphene films. A CVD grown graphene is currently being evaluated for non-electrically active applications such as transparent conducting electrodes for touch screens displays, solar panels, and flexible electronic applications.

Even though graphene grows uniformly over a large surface area, there are a few challenges and drawbacks associated with it for electronic applications. First, there is an order of magnitude difference in thermal expansion coefficient between graphene and Cu,

which causes graphene film wrinkling at the cooling stage of the growth process. The wrinkles are defective in nature, which degrades a device's performance through defect scattering, similar to the effect of grain boundaries seen in conventional materials [114]. In addition, as the growth is performed on conductive metal substrates, transfer of graphene film to other insulating substrates such as SiO_2 is required for using in electronic device applications. When the PMMA resist is used as a support during transfer, it significantly contaminants the graphene film with resist residues even after its removal and therefore high temperature thermal annealing is required for cleaning the as-transferred graphene films [115]. Additionally, graphene films may be broken or damaged during the transfer process, which might compromise the quality of the final transferred layers.

2.4.3 Epitaxial Growth on SiC

Graphene from silicon carbide (SiC) decomposition is a high-quality graphene source discovered by W. de Heer *et al* [116]. This is known as epitaxially grown graphene. It is based on the thermal decomposition of the hexagonal single crystal SiC by sublimation of Si atoms at high temperatures in ultra-high vacuum (UHV) or argon atmosphere conditions as shown in the Figure 2.6 [117]. This method has the benefit of being able to use insulating SiC substrates for the graphene growth, thereby avoiding additional transfer and cleaning steps [104, 118]. The {0001} surfaces of the hexagonal SiC single crystal have both Si-faces (0001) and C-faces ($000\bar{1}$). The Si-face is usually preferred for obtaining better homogeneous growth of graphene. Moreover, the epitaxial

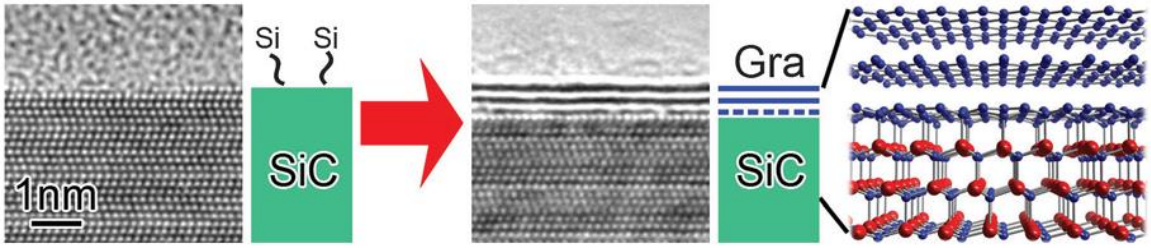

Figure 2.6: Basics of graphene growth by thermal decomposition of SiC, together with the structural model of bilayer graphene on SiC. Shown as the blue broken line is the buffer layer [121].

graphene growth on the Si-surface results in the formation of a carbon buffer layer that is electrically inert [119-120]. Typical growth temperatures and pressures for the Si-face are 1600 ºC and 100 mbar, while for the C-face they are 1450 ºC and $1e^{-4}$ mbar in an argon atmosphere [122]. As a result of this thermal process, a few-layer graphene is formed on the Si-face and a thicker graphene stack is formed on the C-face, although in some cases high-quality graphene monolayers have been obtained on the C-face as well [123]. During Si desorption, the surface of SiC forms narrow terraces of graphene a few micrometers wide, which are linked by steps with higher electrical resistance.

Graphene growth on SiC depends on several growth parameters, including gas pressure, temperature, and growth time. In this way, epitaxial graphene can be formed over a wide range of process conditions. When the pressure of Si above the surface is less than the indicated Si ($\sim 1 \times 10^{-7}$ mbar) vapor pressure, an excess of C will build up on the surface for a given temperature [124]. Under UHV conditions, graphene growth can be accomplished at temperatures as low as about 1200 ºC because the sublimated Si can be

removed by the vacuum system. A higher temperature is required in intermediate vacuum conditions. Inert gases such as argon can be added to further increase the required temperature, since the inert gas increases the Si partial pressure near the surface. Due to this pressure-temperature relationship, the growth rate will increase as the temperature rises, since more Si atoms sublimate, leaving more C atoms on the surface to form graphene. Thus, the graphene growth can be controlled by the choice of temperature, growth time and pressure [124].

2.5 Importance of Metal Contacts on Graphene

Graphene is sensitive to the surrounding environment, which means that any material coming into direct contact with its surface, such as metal electrodes, can have a significant impact on its electronic properties [125]. Electronic devices are inevitably connected to metal contacts, so understanding the electrical characteristics of metal-graphene interfaces is crucial to the performance of graphene devices.

The energy band diagrams of a) metal-semiconductor and b) metal-metal contact interfaces (for comparison) are shown in Figure 2.7 [126]. In the first case, when a metal and a semiconductor come into contact, charge transfer occurs from higher energy state to the lower energy state until the Fermi energy levels of both metal and semiconductor are balanced in thermal equilibrium state. The result is the Schottky barrier, $\Phi_B = \Phi_M - \chi$ at the interface, where Φ_M is the work function of a metal and χ is the electron affinity of the semiconductor. Energy band bending occurs due to the charge transfer, as shown in Figure 2.7(a) and forms a depletion region with a width of W_{dp}. A metal/metal contact, however,

has no potential barrier, so charge carriers transfer directly through the interface, cancelling out the difference in work function. Due to the high carrier density, the small redistribution of the electron cloud can screen out this potential difference. In general, metal screening

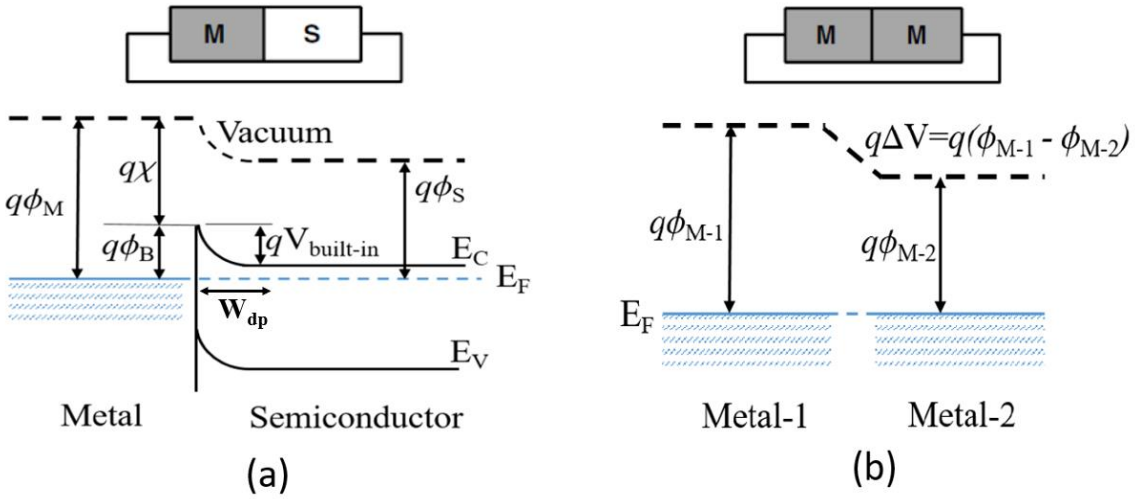

Figure 2.7: Schematic of the interface at (a) metal-semiconductor and (b) metal-metal interfaces [126].

length is typically small (in fractions of nm), as a result the vacuum level changes sharply at the metal-metal interface [126].

The situation is even more complex when a metal is interacted with graphene, since there is no band gap at zero energy and the density of states vanishes at Dirac point (see Figure 2.8(a) and (b)). In the absence of an energy band gap, depletion layer formation and conventional Schottky contacts are prevented. There is a strong limit on current injection from metal to graphene at the Dirac point because of the small density of states (DOS)

[127]. As a result of different work functions, charges transfer through the interface, resulting in graphene's electrical doping. Graphene has a small state density near the Dirac energy, which causes the Fermi level even at a limited charge transfer to shift significantly [127]. When electrons move from metals to graphene (n-doping), the Fermi level shifts upward, but the Fermi level shifts downward when positive carriers (holes) move from metals to graphene (p-doping) [126-127].

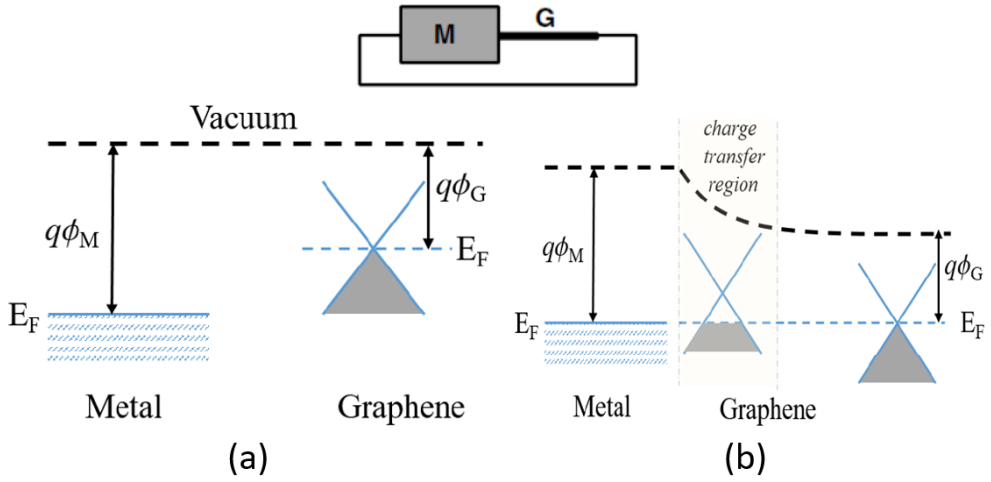

Figure 2.8: Schematic of energy band diagram for the metal-graphene contacts. (a) Representation of separated metal and graphene with its Dirac cone. (b) When metal and graphene are brought in contact, the Fermi levels are aligned. Far away from the metal-graphene contact, the conical point of graphene approaches E_F [126].

It is expected that a crossover from n-doping to p-doping will occur when both sides of the junction have the same doping type but different work functions [128]. In fact, if one of the materials is graphene, the work function difference is not the only parameter since

the chemical interactions at the surface cannot be ignored. In density functional theory calculations, graphene electronic properties can be changed by physisorption at the metal-graphene interface, especially for metals such as Au, Cu, and Pt, or by chemisorption at the metal-graphene interface, such as Ni, Co, and Pd [129-131]. In physisorption, graphene electronic structure is only weakly altered because of weak binding, causing a charge transfer depending on the work functions and a Fermi level shift. In contrast, chemisorption causes a significant change in the electronic structure of graphene due to hybridization between its p_Z states and *d*-states in metal, causing a band gap in graphene and a reduction in its work function [130]. Physisorption or chemisorption of metals is dependent on the degree of filling in the d-orbitals, which determines the stability of the antibonding states, a large number of electrons in the antibonding states destabilizing the hybridization [132].

For instance, in a real system where a finite metal electrode is deposited to cover a graphene sheet (as the case for transport measurements), the Fermi level will be at the Dirac point only when the graphene is free, far from the metal-graphene interface where it is fixed by the metal. The Fermi level difference is accommodated by a charge transfer between the two graphene regions (the free and contacted ones). Based on the Fermi level difference, the band bending can be realized with n-dopants or p-dopants. A suitable choice of metal electrodes makes it possible to engineer p-n junctions in graphene [130]. In addition to doping, metal contacts can also induce compressive strain or tensile strain in graphene due to lattice mismatches, which can influence the electronic properties of graphene [133-134]. Therefore, appropriate selection of metal contacts is of critical importance for the better performance of graphene electronic devices.

2.6 Significance of Graphene Functionalization

Although pristine graphene has many outstanding electronic properties, there are several challenges that need to be addressed before the full potential of graphene can be realized. Graphene, for instance, does not possess a bandgap, so field-effect transistors based on graphene cannot be turned off completely, which eliminates its use in digital electronic applications where high ON/OFF ratios are required [135-137]. Additionally, the highly hydrophobic nature of graphene causes weak metal electrode adhesion, which in turn leads to metal delamination [138]. Furthermore, since graphene is chemically inert, chemical sensors made of pristine graphene typically suffer from weak sensing responses, poor selectivity issues and extremely long recovery times due to the lack of polar functional groups on the surface [49-50, 139]. It is also extremely difficult to chemically interface graphene with other compounds due to this reason. Hence, surface functionalizing graphene is important for enhancing its capabilities and promoting chemical reactions on its surfaces. However, functionalization of graphene is challenging due to the fact that each carbon atom in graphene has a p_z orbital in the direction perpendicular to the base plane, forming a self-passivating π-conjugated system that is highly delocalized [139]. In order to attach a functional species to a thermodynamically stable and chemically inert structure, one must use high energy reactive agents capable of breaking the carbon-carbon π bonds and distort the surrounding lattice structure without damaging the carbon-carbon σ bonds of graphene. In principle, graphene can be functionalized using covalent and non-covalent approaches [140-142].

The covalent functionalization is relatively stable and has been developed for several purposes due to the strong bonding of organic functional groups with the graphene surface [143-144]. For covalent functionalization, highly reactive species, such as hydrogen, chlorine and fluorine, are commonly used. These species possess sufficient energy to overcome the kinetic and thermodynamic barriers associated with the covalent chemical reactions on graphene [145]. According to Figure 2.9, the carbon atoms in graphene change their hybridization from sp^2 to sp^3 [146], which leads to the opening of a band gap [147-148]. This transformation does not just affect the sp^3 carbon atom that is

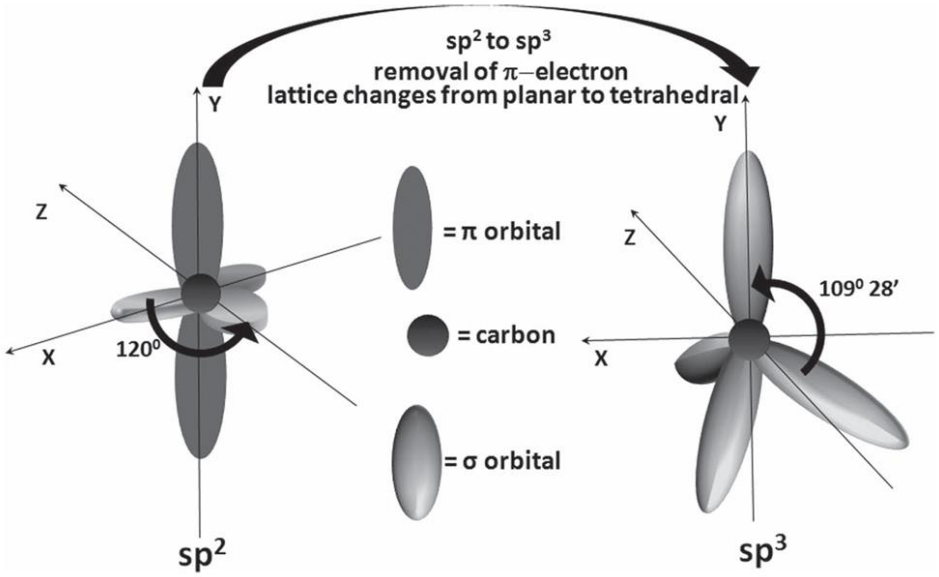

Figure 2.9: Conversion of sp^2 hybridization to sp^3 hybridization leads to removal of the π electron and conversion of the planar lattice to tetrahedral [146].

undergoing reaction, but it also produces a geometric distortion that extends over multiple lattice positions in the structure [146].

Non-covalent functionalization allows the attachment of functional groups to graphene without disrupting its structural properties [143, 149]. The adsorbed molecules interact with the π-electrons of graphene, resulting in the change in electronic and chemical properties of the graphene due to the charge transfer process [149]. A charge transfer or magnitude of doping that occurs on graphene surfaces depends on both the electronic and chemical nature of the analyte being tested. As an example, negatively charged surface areas on graphene will attract molecules with positively charged poles, which strongly adsorb to graphene. As a result of this strong interaction, charge carriers are transferred between the adsorbed analyte and graphene, affecting its charge carrier concentration depending on the analyte type [142, 150]. Even though non-covalent functionalization preserves the structural properties of graphene, the long-term stability of physisorption is always problematic [150]. The weak bond between physisorbed functional groups and graphene leads to their desorption when the device is operated at high bias for several cycles or continuously for a prolonged period [144, 150].

2.7 Type of Electrical Noise

Over the past six decades, electrical noise in semiconductors has been extensively studied, resulting in numerous physical and empirical models that describe a specific type of noise in detail [151-154]. Several electrical noise components are well understood and well defined, for example thermal noise, shot noise, generation-recombination noise [155-156]. One particular component of noise is inconclusive to describe or even to agree on its origin, and that is flicker noise or $1/f$ noise. From the physics perspective, electronic noise

is one of the carrier dynamics that relates to a solid-state scattering process [157]. Charge carriers collide in the scattering process because of lattice vibrations which occur during the transport of charge carriers or during their trapping/de-trapping from the trap sites. It has been known that the scattering elements are channel defects, interface states, oxide traps or contacts [158]. Noise comes in different types and in the frequency domain it has different characteristics depending on the source of noise. The representative basic sources of noise are discussed and explained in this section.

2.7.1 Thermal Noise

The thermal noise, first predicted by Albert Einstein [159], occurs when the electromotive force fluctuates due to Brownian motion of free electrons within a material under thermal equilibrium. The phenomenon was later demonstrated experimentally by J. Johnson [160] and the power spectral density was calculated by H. Nyquist [161]. Therefore, thermal noise is also known as the Johnson, Nyquist, white noise, diffusion noise or velocity fluctuation noise. As a result of carrier scattering, thermal noise is produced by causing the carrier velocity to become randomized as it moves through the material, causing a form of velocity gradient to develop. As the gradient is generated, the surrounding carriers drift into a specific direction, causing a small net current flow which can be measured as the noise power spectrum density (PSD). Under equilibrium conditions, the average energy of this motion is expressed as k_BT / 2 and demonstrates an ultra-fast relaxation time of $\tau \approx 10^{-12}$ s [160-161]. Thus, the observed noise spectrum is frequency

independent, such that $S_A(f)$ is constant throughout the frequency range investigated. In conventional notation, the voltage and current noise power spectral density expressed as:

$$S_V = 4k_B TR \tag{2.1}$$

$$S_I = \frac{S_V}{R^2} = \frac{4k_B T}{R} \tag{2.2}$$

where k_B is the Boltzmann constant, T is the absolute temperature, and R is the resistance. Thermal noise measurement system is often used to calibrate a noise measurement system because it can provide information about the limits of the measurement system as it is temperature related [162].

2.7.2 Shot Noise

A shot noise refers to the random tunneling of a free carrier (electron) through a potential barrier, which is common in device with a Schottky contact or a space-charge region formed by a p-n junction. It is a non-continuous process in which the noise current is generated discretely when the electrons cross a potential barrier randomly and independently. In 1918, W. Schottky first discovered this noise in vacuum tubes and derived the formula for it [163]. Similar to Johnson noise, shot noise is independent of frequency due to short electron transition process and current PSD can be expressed as:

$$S_I = 2qI \tag{2.3}$$

where q is the electron charge, and I is the corresponding leakage current flowing through the potential barrier. A shot noise is also known as white noise similar to Johnson noise

due to its frequency dependence. It is not easy to distinguish Johnson noise from the shot noise, but shot noise is typically much smaller.

2.7.3 Generation/Recombination Noise

Generation-recombination noise (*g-r* noise) is caused by the generation and recombination of charge carriers (i.e., electrons or holes) by trap sites, resulting in conductance fluctuations. In semiconductors, localized states are unable to conduct whereas delocalized states enable electron conduction. These localized states, also called

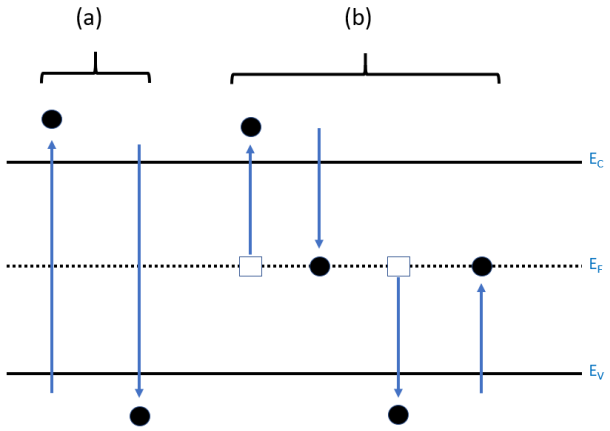

Figure 2.10: Generation-recombination mechanism for the a) direct band to band and b) four possible types of trap assisted carrier transition.

"traps," are caused by defects or impurities in the semiconductor or at the interface. An illustration of these mechanisms can be found in Figure 2.10. The PSD of *g-r* noise is given by a Lorentzian behavior

$$\frac{S_I}{I^2} = \frac{S_R}{R^2} = \frac{S_N}{N^2} = \frac{\overline{\Delta N^2}}{N^2}\left[\frac{4\tau}{1+(2\pi f\tau)^2}\right] \tag{2.4}$$

where N is the averaging number of free carriers, $\overline{\Delta N^2}$ the variance of the fluctuating number of charge carriers, and τ the carrier relaxation time. The relaxation time τ is in the range of 10^{-6} s to 10^{-3} s as a characteristic of traps. In order for the *g-r* noise to be valid, the Fermi energy level is near, within a few kT, to the trap energy level [164]. Trap characteristics are generally influenced by trap energy level and trap spatial position.

2.7.4 1/*f* noise or Low Frequency Noise (LFN)

1/*f* noise is also known as flicker or excess noise with a PSD inversely proportional to the frequency *f*. This phenomenon has sometimes been called low-frequency noise, but it is not entirely accurate since other kinds of noise, such as *g-r* noise, can also be observed in the low-frequency range. In 1925, Johnson found and explained the 1/*f* noise in vacuum tubes, and Schottky gave the first interpretation of it [165]. The phenomenon was finally verified by the Voss and Clarkes' experiment in 1976 [166]. As a result of this experiment, it was found that PSD of the measured 1/*f* noise shows an I^2 dependency with a constant driving current, and the V^2 dependency with a fixed bias voltage. The square current/voltage function of $S_A(f)$ (Note that $S_A(f) \propto I^2$ or V^2 since it is a power unit, followed by $P = I^2R$ or V^2/R notation) implies that the applied external bias does not contribute to measured voltage/current fluctuation, but that instead it reveals the conductance perturbation in the device [166]. Until now, a large number of current noise spectra were

measured with various materials, such as semiconductors, semimetals, metals, superconductors, tunnel junctions, strongly disordered conductors, and so on [167]. It appears that all the results generally followed a trend of a rise in current noise power spectrum with decrease in frequency, 1/*f*. It is generally hard to detect 1/*f* noise at high frequencies because it is hidden by the Johnson noise.

Even though 1/*f* noise is universal and affects various materials, the origin of the noise has been the subject of controversy for decades. The major issues include the following: 1) Mobility vs. Number fluctuations, 2) Superposition of Lorentzian noise for 1/*f* noise, and 3) Surface vs. Bulk origins [168].

1) Mobility vs. Number fluctuations:

An important issue is to understand where the noise in 1/*f* comes from. Conductivity fluctuations can explain the current fluctuations in materials since the conductivity is an inherent property of devices. So, the conductivity σ is defined as [168]

$$\sigma = qn\mu_{drift} \tag{2.5}$$

Where n is the charge carrier density and μ_{drift} is the drift mobility. Two representative models are presented based on the idea of conductance fluctuations. From a physical viewpoint, the number fluctuation is caused by trapping/releasing of carriers at the interface, while the mobility fluctuation is due to phonon scattering within the solid [169]. In conventional MOSFETs, the main 1/*f* noise source has been generally explained by the number fluctuation model. But there are other devices where noise is explained by the mobility fluctuation model. For example, for 0.35 μm *p*-type FETs, the mobility fluctuation

model dominates because the channel is buried [170]. On the other hand, some results support the mobility fluctuation [171-172]. The number fluctuation with charge trapping at the interface does not work in carbon nanotubes, and other explanations such as diffusion or electron-phonon interaction are suggested [171]. The electron-phonon interaction is strongly supported the temperature dependence of 1/*f* noise in single-walled carbon nanotubes [172]. These results show that the noise can be changed and it depends on the devices architecture or conduction mechanism.

2) Superposition of Lorentzian noise for 1/*f* noise:

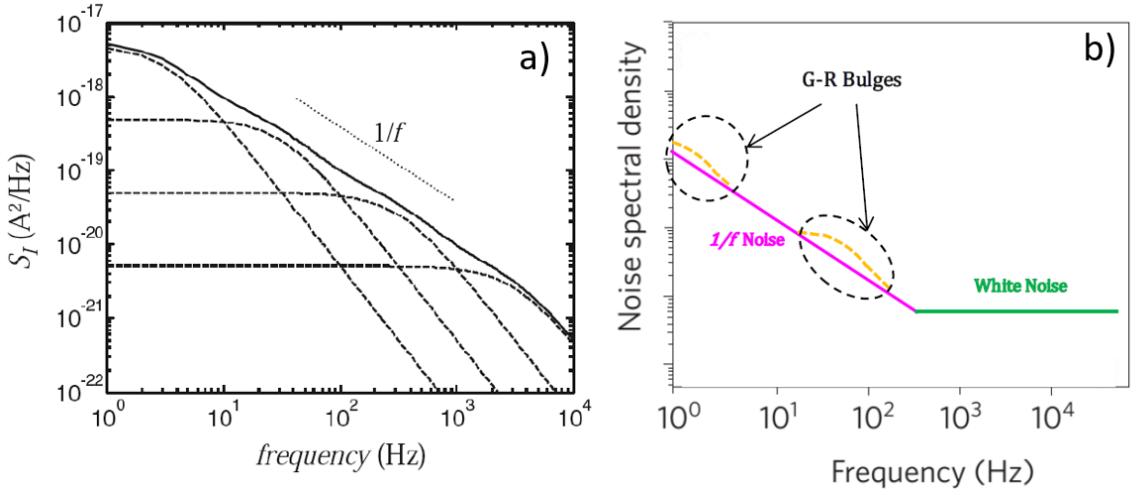

Figure 2.11: (a) 1/*f* noise spectrum composed of several Lorentzian spectral with evenly distribution carrier lifetime. (b) Example of generation-recombination (*g-r*) bulge when the Lorentzian spectrums of *g-r* origin is superimposed onto another 1/*f* noise component [177].

A 1/*f* behavior can be obtained by superposition of Lorentzian noise, as suggested by J. Bernamont and M. Surdin [173-174]. By using multiple Lorentzian spectra, the 1/*f* noise spectrum can only be formed if carrier interactions with specific trap species are separated from carrier generation-recombination processes, and carriers hop minimally from one trap species to another [175-177]. The 1/*f* spectrum produced by the summation of several discrete Lorentzian spectra of different trap species are shown in Figure 2.11(a). A distinct generation-recombination bulge can occur if one trap species dominates the conductance fluctuation process, causing the Lorentzian spectra generated by such species to superimpose on the 1/*f* spectrum, disrupting the 1/*f* dependency of $S_A(f)$ [177]. An illustration of this phenomenon is shown in Figure 2.11(b).

3) Surface vs. Bulk origin:

In general, the arguments for the surface or bulk effect on the 1/*f* noise arise from a controversy regarding the mobility and number fluctuation models. There are two competing theories, including the McWhorter number fluctuation theory which considers the surface effect and the Hooge mobility fluctuation theory for homogeneous bulk such as metals and semiconductors [178]. There is a general belief that surface noise or bulk noise, or both are present depending on the device structure [178-181]. Furthermore, both theories are supported with experimental evidence. The 1/*f* noise behavior in nanomaterial structures might be affected by surface effects due to smaller sizes.

CHAPTER 3 : GRAPHENE GROWTH, FABRICATION, FUNCTIONALIZATION AND DEVICE GEOMETRIES DESCRIPTION

3.1 Graphene Growth, Fabrication, and Functionalization

Epitaxial graphene films were grown on the Si face of semi-insulating, on-axis 6H-SiC substrates by Si sublimation at high temperature in a chemical vapor deposition reactor [182]. As described elsewhere, a photoresist bi-layer method combining LOR and Shipley 1811 photoresists was used with contact printing at $\lambda = 320$ nm in two steps to achieve a clean and patterned post-fabrication graphene active region [183] and low graphene-metal contact resistance [184] after processing. The first step used oxygen plasma etching in two sequential steps of two minutes each at 30Win order to minimize sample heating during the etch. After stripping in a 75 ºC bath of N-methyl pyrrolidinone (NMP), followed by an isopropanol rinse, we applied the second photolithographic process step for patterned e-beam evaporation and lift-off in NMP to form Ti/Au (10 nm/100 nm) contacts. The films were functionalized using N-ethylamino-4-azidotetrafluorobenzoate (TFPA-NH2) as a chemical linker, which results in increased functionality of the graphene films without degradation of its electrical properties [185]. Then, zinc oxide nanoparticles (50–80 nm, US Research Nanomaterials Inc., Houston, TX, USA) were attached [186].

3.2 Device Geometries Description

Graphene devices were fabricated on 8 × 8 mm^2 SiC chips bearing 4 die, each die with 13 sensor devices (schematic shown in Figure 3.1(a)) and 2 to 4 transfer length method (TLM) structures (Figure 3.1(b)) for measuring contact resistance. The various chemiresistive sensor device structures, all built on a common 400 × 400 μm^2 graphene

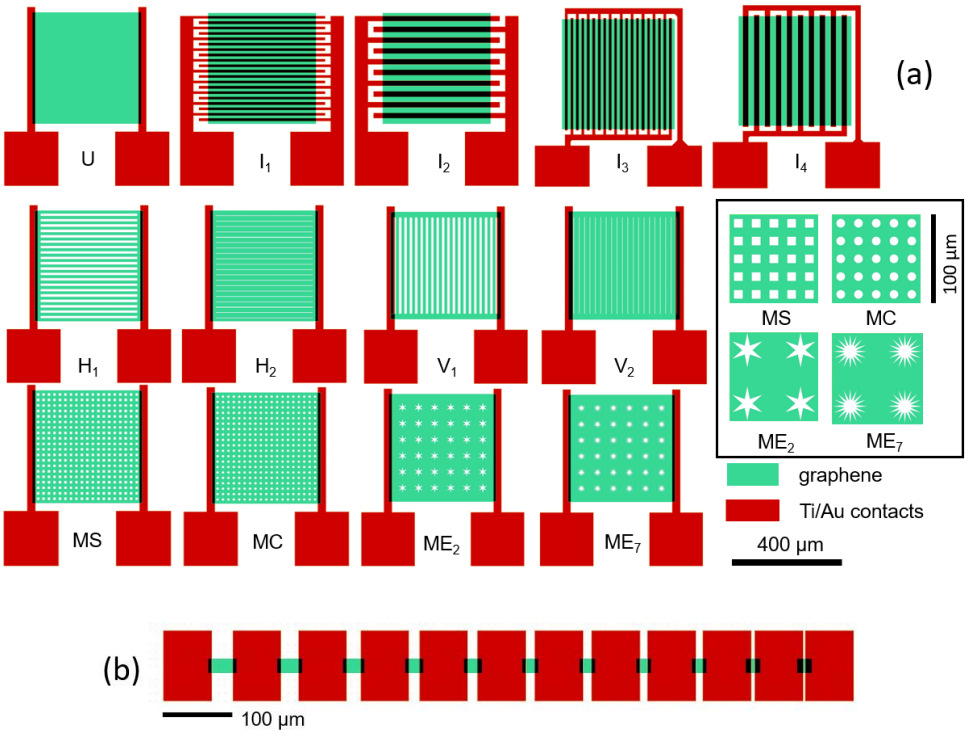

Figure 3.1: (a) Computer-aided design (CAD) schematic of the device designs studied here. Note that four die were printed on a chip (8 x 8 mm^2 area). The devices are classified into four groups based on graphene film patterning: (1) unpatterned (labeled "U") and interdigitated group (labeled "I_1, I_2, I_3, I_4"); (2) patterned with horizontal slots (labeled "H_1, H_2"); (3) patterned with vertical slots (labeled "V_1, V_2"); (4) patterned with 2D patterns (labeled "MS, MC, ME_2, ME_7"). Detail of the 2D patterns is shown in the inset. Descriptions are provided in Table 1. (b) CAD schematic of the TLM structures. The graphene mesas are 20 µm wide, the 70 µm x 100 µm Ti/Au pads overlap the graphene by 5 µm, and the uncovered lengths are 30, 25, 20, 15, 14, 13, 12, 11, 10, 5, and 3 µm.

mesa, can be classified into four groups. The devices, except for the interdigitated group, had the same channel length of 380 µm and varying channel widths. Group 1 consisted of an unpatterned graphene device (U) and devices having interdigitated electrodes, with 10 µm (I_1, I_3) and 20 µm (I_2, I_4) channel lengths and corresponding channel widths of 3600 µm and 7600 µm, respectively. They were printed in either of two orthogonal orientations in order to explore directional dependence of conductivity in the epitaxial graphene. Group 2 consisted of patterned devices with slots aligned with charge transport (henceforth

Table 3.1: Detailed description of the four graphene chemiresistive device group structures shown in Figure 3.1. The terms "horizontal" and "vertical" refer to the graphene pattern with respect to the direction of charge transport, parallel or perpendicular, respectively. "Constricted channel width" refers to the minimum graphene channel width after etching, i.e., overall film width less total hole cross section.

Channel Structure Type	Device Designation	Channel Length, µm	Channel Width, µm (Constricted)	Detailed Description
Group 1: Unpatterned	U	380	410	Horizontal transport
	I_1	10	7600	Vertical transport
	I_2	20	3600	
	I_3	10	7600	Horizontal transport
	I_4	20	3600	
Group 2: Horizontal Slots	H_1	380	210	21 ea. 10 µm strips
	H_2	380	350	20 ea. 17 µm strips, 2 ea. 5 µm strips
Group 3: Vertical Slots	V_1	380	40	2 ea. 20 µm wide strips at either end of set of slots, strips 360 µm long, 10 µm and 17 µm wide, respectively
	V_2	380	40	
Group 4: 2D Patterns	MS	380	220	10×10 µm^2 squares on regular 20 µm pitch grid
	MC	380	210	10 µm dia. Circles on regular 20 µm pitch grid
	ME_7	380	160	416 µm^2 area, 425 µm coded perimeter, on regular 60 µm pitch grid
	ME_2	380	160	480 µm^2 area, 180 µm coded perimeter, on regular 60 µm pitch grid

"horizontal" and identified as H_1, H_2). Group 3 consisted of patterned devices with slots transverse to charge transport (henceforth "vertical" and identified as V_1, V_2). Group 4 consisted of patterned devices with regular 2D hole patterns including 16 point (ME_7) and 6 point stars (ME_2), 10×10 μm^2 squares (MS), and 10 μm dia. circles (MC). The TLM structures were fabricated with contact separations from 3 to 30 μm and a uniform width of 20 μm. The Ti/Au contacts were 70×100 μm^2 rectangles that overlapped 5 μm of the graphene films, thus adding a metal–graphene edge junction of nominally 30 μm at each contact. See Table 3.1 for a detailed description.

CHAPTER 4 : ELECTRICAL CHARACTERIZATION OF GRAPHENE CHEMICAL SENSOR DEVICE HAVING DIFFERENT GEOMETRIES

4.1 Introduction

Graphene has a great potential for vapor sensing applications because of its high electrical conductivity [187-188], large surface-to-volume ratio, high mobility (~200,000 cm^2/Vs), low thermal and $1/f$ noise characteristics [49, 189], and low room temperature contact resistance [190-191]. Graphene sheets (one monolayer thick) possess the remarkable quality that every atom is a surface atom and involved in carrier transport. Thus, even a single vapor adsorption event is transduced into an easily measured change in conductivity [192-193]. This property explains the single molecule detection of gas phase molecules [49]. Even though graphene is extremely sensitive, it is not selective due to its inert nature. This is remedied by functionalization with organic linker molecules, nanoparticles, biomolecules, etc., which enhances the selectivity [143-144, 146, 194-195].

Graphene chemical vapor sensors, fabricated as two-terminal devices exposed to ambient, operate on the principle that their electrical resistance changes in response to changes in ambient molecule concentration and, in particular, to adsorption from chemical vapors. Maintaining a low contact resistance in these devices is crucial for maximizing the relative effect of chemical-exposure-induced changes in device resistance. Published values of graphene–metal Ohmic contact resistance vary considerably depending on the fabrication approach [196-204]. Additionally, graphene has very low intrinsic noise, so any changes produced by defects, both intrinsic (e.g., lattice vacancies) and extrinsic (e.g., engineered holes and the associated edges in addition to the exposed edges of a finite

device), as well as surface functionalization and adsorbates [73], can have a significant impact on the observed low frequency (*LF*) noise behavior. Understanding the noise behavior of electronic devices is important from an application point of view as well because this LF noise determines the smallest amount of information or signal from a device that can be detected, whether a device is functioning as an amplifier, a transducer, or merely a conveyer of information [205]. The LF (<1 Hz) spectral region is typically dominated by what is commonly referred to as $1/f$ or flicker noise, in which the power spectral density (PSD) of electrical fluctuations is inversely proportional to exponentiated frequency, f^{γ}, with γ ranging from 0.5 to 2 but often close to 1 [205–208]. This $1/f^{\gamma}$ noise has been observed in many material systems [209-210]. This LF behavior is typically determined by intrinsic device or material properties, in particular dynamic changes in carrier concentration or carrier mobility associated with trap nature and density, generation-recombination centers, lattice scattering from phonons, transport scattering points associated with impurities and vacancies, and so on. Analysis of LF behavior provides insight into the physical properties of both material and devices [207, 210].

In this work, we carried out electrical conductivity and LF current noise measurements at room temperature in air ambient conditions on large-area monolayer graphene devices with and without ZnO nanoparticle functionalization. Zinc oxide nanoparticles are one of the most widely investigated structures for chemical sensing due to their high thermal and chemical stability. Zinc oxide is an n-type semiconductor with a wide band gap energy of 3.37 eV. It has been reported that ZnO nanoparticles alone, and as part of a graphene composite system, have a high sensitivity towards methane, nitrogen

dioxide, hydrogen, and ammonia, as well as ethanol and acetone [70, 211-212]. Maximizing sensor sensitivity is of paramount importance, and in this work, we explore the relationship among device geometry resistance, and noise for pristine and functionalized devices. The investigated geometries include arrays of squares, circles, holes, and slots transverse or longitudinal to the applied electric field etched into a 0.16 mm^2 mesa. Such a large device size is relevant to sensor applications where it is important to minimize ultra-low frequency noise. A large area device will maximize the number of charge carriers and so minimize $1/f$ noise [207], as well as ultimately minimizing the Poisson noise of adsorbates at low concentrations. Additionally, we explored the impact of contact resistance on LF noise.

4.2 Instruments and Experimental Set-up

A Keithley 236 source measurement unit (SMU) supplying 1 VDC was used to measure device resistance. Two configurations were used for room temperature low frequency noise measurements, from 0.24 Hz to 97.5 Hz and from 0.001 Hz to 1 Hz, as shown in Figure 4.1(a) and 4.1(b), respectively. We measured the current noise of the devices by measuring the voltage across a 3.3 kΩ wire wound precision resistor in series with the sensor device using a spectrum analyzer with an input impedance of 1 MΩ ‖15 pF. A Hann window was applied to each frame prior to the application of a fast Fourier transform (FFT). The resulting frequency data was averaged for at least 5 such scans.

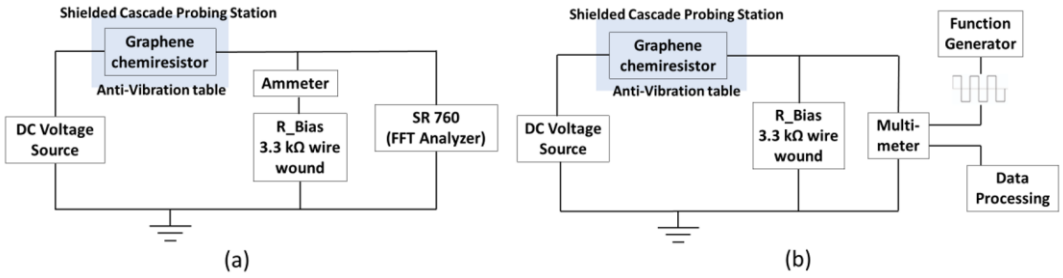

Figure 4.1: SR760 fast Fourier transform (FFT) spectrum analyzer noise measurement setup for graphene devices in a frequency range (a) from 0.24 Hz to 97.5 Hz and (b) from 0.001 Hz to 1 Hz at room temperature. A 3.3 kΩ wire wound resistor converted the induced current into a voltage for sampling either automatically by the SR760 or by an Agilent 34401A multimeter as triggered by an Agilent 33250A function generator.

4.3 Results and Discussion

4.3.1 Resistance Measurements

In this section, we report the resistance properties of pristine and ZnO functionalized graphene films and devices. First, the contact resistance (R_c), sheet resistance (R_{sh}), and contact resistivity (ρ_c) of the graphene films were determined from the TLM structures described above. Next, we measured the devices' total resistance. Finally, we calculated the effective width, contact area, contact resistance, and sheet resistance for the device structures.

In general, the resistance (R) of any material is given by $R = \rho L/A$, where ρ is the bulk resistivity, L is the length, and A is the cross-sectional area (width W × thickness t) of the material in a plane normal to the direction of current flow. For graphene films, we assume that the films are of uniform thickness, so that the cross-section is determined entirely by the effective device width. For the group 2, 3, and 4 devices (Figure 3.1, Table

3.1), the width at the constrictions should dominate the overall measured resistance. A more complete picture of device resistance also considers contact resistance and the effect of the depletion length at the contacts, especially in comparison to the overall channel length. The interdigitated structures I_1 through I_4 offer an opportunity to observe directional dependence of electrical conduction in graphene [213-215]. Transport in I_3 and I_4 is in the same average direction as in the devices other than I_1 and I_2: U, Group 2, Group 3, and Group 4. We present in Figure 4.2 the total resistance (R_T) of the TLM structures plotted against the varying graphene channel lengths for both pristine and functionalized graphene films. The slope of the linear fit in Figure 4.2 gives the channel width a normalized value (R_{sh}/W) of the graphene sheet resistance. The contact resistance, R_c, is extracted from the extrapolated resistance at zero channel length, $2 \times Rc$. The contact resistivity is determined

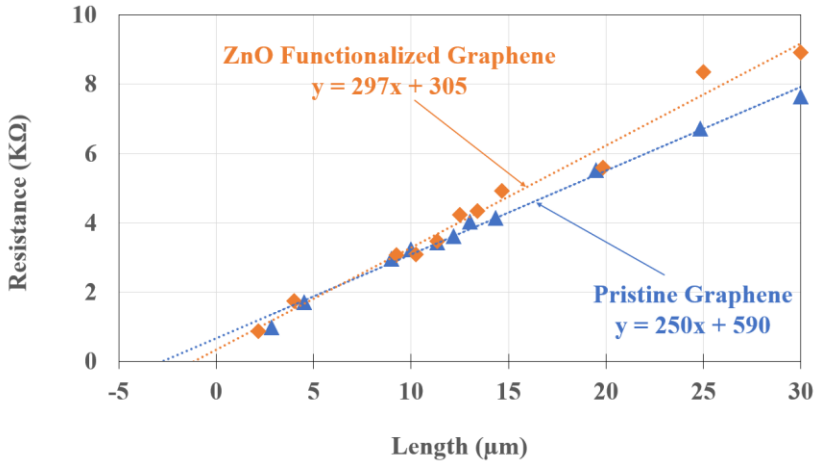

Figure 4.2: Resistance of pristine and ZnO functionalized graphene as a function of distance between metal contacts as measured after fabrication. The dotted lines are the transfer length method (TLM) linear fits.

from the equation $\rho_c = Rc \times W \times L_T$, where L_T is the transfer length, the average distance that an electron travels in the material beneath the contact before it flows up into the contact. The transfer length, L_T, is obtained from the extrapolated length at zero resistance ($-2L_T$ = x-intercept) [216].

The calculated R_c, R_{sh}, L_T and ρ_c for pristine and functionalized graphene films are shown in Table 4.1. There is a substantial decrease in contact resistance (factor of two), and in contact resistivity (factor of 3.5) and a moderate increase in sheet resistance of the functionalized films relative to that of the pristine graphene. This change in R_{sh} is consistent with a previous investigation [185], which also found a substantial decrease in carrier sheet

Table 4.1: Electrical characteristics of pristine and functionalized graphene films with evaporated Ti/Au contacts calculated using the TLM data in Figure 3.3 (contact width = 20 μm, length = 5 μm). Data from ref [193] refers to CVD graphene with Al/Cr/Au contacts, measurements from TLM structures. Data from ref [184] refers to annealed graphene, measurements from TLM structures.

Parameter	Pristine	Functionalized	Ref 193	Ref 184
R_c, Ω-μm	5900 ±800	3050 ± 1800	1497	1075 ± 285
R_{sh}, kΩ/□	5.0 ± 0.1	5.9 ± 0.3	0.952	0.84
L_T, μm	1.2 ± 0.2	0.53 ± 0.1	1.57	1.28
ϱ_c, Ω-cm^2	7.2 x 10^{-5} ± 2.2 x 10^{-5}	2.2 x 10^{-5} ± 2.5 x 10^{-5}	2.35 x 10^{-5}	1.38 x 10^{-5}

concentration to about 4×10^{12} cm^{-2} and an increase in carrier mobility of functionalized films relative to pristine. Following the approach of Nath, et al. [184] we apply the

Landauer-Büttiker model for conductance of a one-dimensional wire to represent the graphene-metal contact resistance as

$$R_C = \frac{1}{T}\frac{h\pi^{1/2}}{4e^2 n^{1/2}} \tag{4.1}$$

where T is the carrier transmission probability, h is Planck's constant, n is the sheet carrier concentration and e is the electron charge underneath the metal [184, 217-218]. For perfect quantum limited contacts, one assumes T = 1 and this gives a lower bound to contact resistance, assuming $n = 4 \times 10^{12}$ cm^{-2}, of about 57 Ω-μm. In our case, the functionalized sheet resistance has increased by 20% compared to pristine graphene. Assuming the previously observed drop in sheet carrier concentration after functionalization to have also occurred here, then the nearly two-fold reduction in contact resistance must be due to increased T, which could be explained by changes in the film work function induced by functionalization that lowers the interfacial barrier height.

Next, we measured R_T of the pristine and functionalized graphene devices (Table 4.2). In general, the R_T values of pristine and functionalized devices are very similar with the exception of the MC, ME_7, and ME_2 devices from Group 4. We found that the structure group, and the specific features within the group, have a much stronger effect on the

Table 4.2: The average device total resistance values (R_T) for pristine and ZnO functionalized graphene device structures (open cells indicate devices not studied).

Groups	Device Designation	Total Resistance R_T (kΩ)	
		Pristine Graphene	ZnO Functionalized
Group 1	U	4.49	5.10
	I_1	0.03 ± 0.003	
	I_2	0.05 ± 0.004	
	I_3	0.06 ± 0.002	
	I_4	0.08 ± 0.007	
Group 2	H_1	8.14 ± 1.46	9.07
	H_2	5.36 ± 1.80	4.93
Group 3	V_1	50.5 ± 15.4	48.9 ± 3.69
	V_2	59.1 ± 19.7	46.6 ± 1.58
Group 4	MS	7.73 ± 2.51	7.24
	MC	6.95 ± 1.89	8.63 ± 0.18
	ME_7	8.84 ± 1.82	11.2 ± 1.26
	ME_2	5.27 ± 0.63	8.31 ± 1.90

measured values. In general, group 3 (V_1, V_2) had the highest R_T values, and group 1 (I_1 - I_4) the lowest. Group 1's unpatterned device U, group 2, and group 4 had similar total R_T values 4.5-9 kΩ. The relatively smaller normalized resistance of the Group 4 devices is not surprising, as some current spreading in the regions between the etched features is to be expected.

Finally, we calculated the effective contact area, the device contact resistance R_C, and the device sheet resistance R_{sh} of pristine and functionalized graphene device structures for the different device geometries. The extrinsic contact resistance R_c (not the intrinsic resistivity) for the actual sensor device is calculated from geometry and values of L_T and

ρ_c calculated from the TLM structures, estimating R_c for each sensor device from ρ_c as derived from the TLM data, the overlapping contact width W_c, and the calculated transfer length L_T from table 4.1 using the relation

$$R_C = \frac{\text{Contact Resistivity}}{\text{Contact Area}} = \frac{\rho_c}{W_C \cdot L_T}. \tag{4.2}$$

Sheet resistance is calculated here simply from $R_{sh} = (R_T\text{-}2R_C) * W_{ch}/L$, where W_{ch} is the effective channel width after accounting for etched features and neglecting lower resistance (i.e., wider) sections (Table 3.1). The resulting values are plotted in Figure 4.3, and given Table 4.3. The R_{sh} of devices I_1, I_2, I_3 and I_4 is quite large compared to the expected value obtained from the TLM structures given in Table 4.1 as well as that of the other devices. Since the typical depletion width in graphene, which would decrease the effective channel length, is quite small, of order 100 nm or less, further work is needed to understand the inconsistency observed here. A desired condition for sensor applications, namely the relative relationship $R_c << R_T$, is realized for all but the interdigitated device geometries in this study.

Table 4.3: Effective contact area calculated from the device channel width and film contact transfer length L_T as derived from TLM data, contact resistance (R_C), and calculated sheet resistance (R_{sh}) of pristine and functionalized graphene device structures after correcting for constricted width values of the different device geometries (open cells indicate devices not studied).

Group	Device Designation	Pristine Graphene			Functionalized Graphene		
		Effective Contact Area (μm^2)	Contact Resistance R_C (kΩ)	Sheet Resistance R_{sh} (kΩ/□)	Effective Contact Area (μm^2)	Contact Resistance R_C (kΩ)	Sheet Resistance R_{sh} (kΩ/□)
Group 1	U	492	0.03	4.8	217	0.02	5.5
	I_1	4800	0.003	16.7	2120		
	I_2	2400	0.006	6.8	1060		
	I_3	4800	0.003	38.8	2120		
	I_4	2400	0.006	12.4	1060		
Group 2	H_1	492	0.03	4.5	217	0.02	5.0
	H_2	492	0.03	4.9	217	0.02	4.5
Group 3	V_1	480	0.03	5.3	212	0.021	5.1
	V_2	480	0.03	6.2	212	0.021	4.9
Group 4	MS	492	0.03	4.4	217	0.02	4.2
	MC	492	0.03	3.8	217	0.02	4.7
	ME_7	480	0.03	3.7	212	0.021	4.7
	ME_2	480	0.03	2.2	212	0.021	3.5

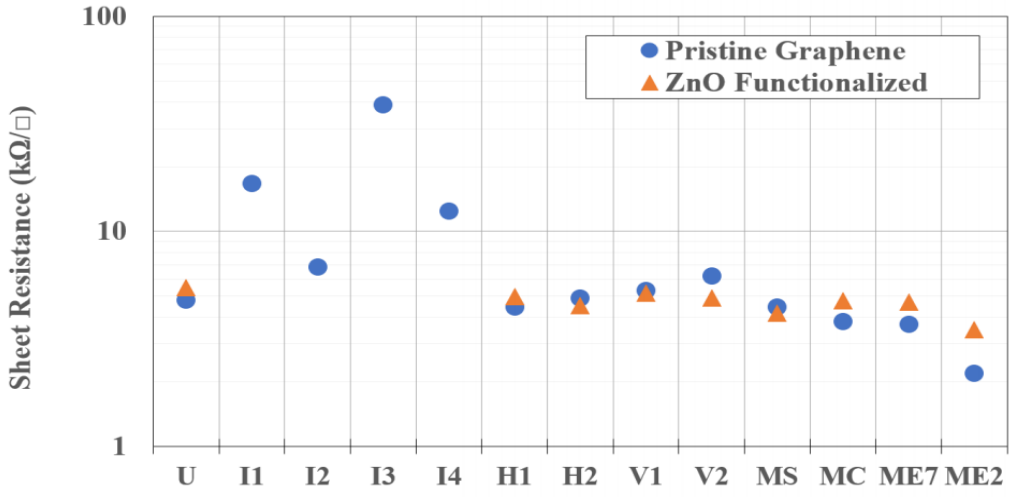

Figure 4.3: Sheet resistance, accounting for internal etched features, of different geometries on pristine and ZnO functionalized graphene as calculated from data extracted from TLM measurements and graphene features.

The effective channel widths (W_{eff}) can be calculated using the relation $W_{eff} = (R_{sh} \times L) / R_{ch}$, where R_{sh} is the sheet resistance calculated from the TLM data (Table 4.1), L is the graphene channel length, and R_{ch} is the channel resistance, $R_T - R_c$. For comparison, the calculated W_{eff} and width values for pristine and functionalized graphene are shown in Table 4.4.

Table 4.4: Summary of coded width and effective width for pristine and ZnO functionalized graphene device structures.

			Effective Width (μm)	
Group	**Device**	**Coded Width (μm)**	**Pristine Graphene Films**	**ZnO Functionalized Graphene Films**
Group 1	U	410	387	389
Group 2	H_1	210	211	200
	H_2	350	323	373
Group 3	V_1	40	34	37
	V_2	40	29	40
Group 4	MS	220	222	256
	MC	210	248	214
	ME_7	160	194	68
	ME_2	160	329	94

The W_{eff} calculations are not applied to the interdigitated devices due to the uncertainty in the effective channel length which is much smaller than the mask channel length L, as explained above. A defect, such as the termination of a crystalline lattice structure at an interface, can contribute a mobile charge and change the number of carriers.

In normal materials, this can increase or decrease the conductivity depending on the type of the added carrier, majority, or minority. Graphene is ambipolar, so the addition of more carriers of either type simply increases the conductivity. A defect can also create a fixed dipole which can scatter charges, lowering mobility and, hence, conductivity if it is in the path of transport. Charges created at defect sites will diffuse away from areas of high concentration (where the defects are) to areas of low concentration (normal film) but usually leave a fixed charge behind which may be partially screened. In the devices discussed here, defects are present from both the structures etched into the graphene as well as when the organic linkers and nanoparticles are added during the functionalization process. The precise nature and impact of each will be addressed in future work.

4.3.2 Low Frequency Noise in Graphene Devices

The current noise of our devices was measured by sampling the voltage developed across a resistor in series with the sensor device when a 1V DC bias was applied across the pair. A wire-wound resistor was used (rather than metal film, *etc.*) to reduce the contribution to the measured noise from that component [219]. The value of the resistor, 3.28 kΩ, was selected to match the average resistance value of all of the devices. In order to obtain a power spectrum $S^2(f_n)$ of the device noise, we note that the discrete Fourier transform of a set of N voltage samples $V_{d,k}$, $k = 0, 1, ..., N-1$, collected across the device at time intervals of width Δ where the device is in series with the resistance R dividing a voltage V:

$$S(f_n) \approx \Delta \sum_{K=0}^{N-1} (V_{d,k}) e^{\frac{2\pi i k n}{N}} = \Delta \sum_{K=0}^{N-1} (1 - V_{R,k}) e^{\frac{2\pi i k n}{N}} = \Delta \left[\sum_{K=0}^{N-1} e^{\frac{2\pi i k n}{N}} - \sum_{K=0}^{N-1} V_{R,k} e^{\frac{2\pi i k n}{N}} \right] \quad (4.3)$$

is equivalent to sampling the voltage across the device $V_{d,n}$ because the first term in the right-hand expression vanishes due to orthogonality, and the negative sign on the second term vanishes when the term is squared during subsequent processing, leaving the following:

$$S(f_n) \approx \Delta \sum_{K=0}^{N-1} V_{R,K} e^{2\pi i k n / N} \quad . \quad (4.4)$$

The voltage data were obtained by sampling at 2.31 Hz over 665 second durations. Work not reported here established a corner frequency of 1-10 Hz, and there was generally no significant power or signal at higher frequencies to be aliased into this frequency range.

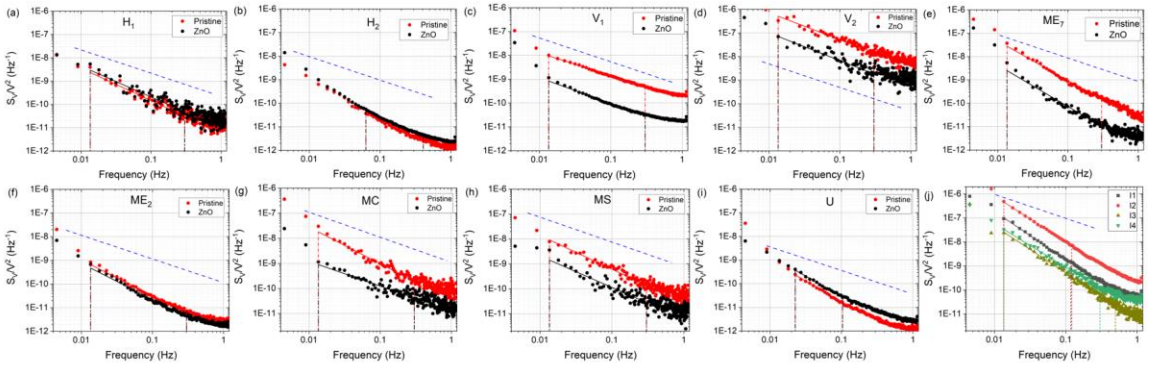

Figure 4.4: Normalized (S_V/V^2) noise data, plotted vs. frequency and for each device: Pristine graphene devices are plotted with black triangles, functionalized devices are plotted with red circles. The four interdigitated devices of pristine graphene I_1-I_4 are also shown. A linear fit to a portion of the power spectrum, and the frequency range over which it was calculated, is shown for each data set. A representative $1/f$ line is also shown on each graph as a blue dashed line; the vertical placement is arbitrary, with no significance.

A Hann window was applied to each frame prior to the transform and the resulting frequency data between 0.00451 and 1.15 Hz was averaged for at least 5 such scans. After normalizing the FFT of each device response by the average voltage across the device, the results are plotted and shown by device in Figure 4.4 along with a linear fit of log S_V/V^2 vs f generally between 0.015 and 0.2 Hz. The observed noise is low compared to other published work [220-224]. However, consideration of an argument of Snow et al. suggests that our observed noise attenuation could be attributed to the increased device size [225].

Low frequency noise in graphene under ambient conditions has been attributed to multiple sources including slow traps, generation/recombination (GR) centers, scattering from impurities, and dynamic changes in the scattering cross-section, presumably due to the chaotic impact on dipole screening of the constrained motion of charge carriers in the 2D film [207]. In order to analyze the performance of graphene-based devices previous studies [205-206] have used the following empirical expression [220] to quantitatively describe the magnitude of the low frequency noise:

$$\frac{S_V}{V^2} = \frac{S_I}{I^2} = \frac{A_N}{f^\gamma} \tag{4.5}$$

where f is the frequency, γ is the frequency scaling exponent and A_N is related to the Hooge parameter α_H through $A_N = N\alpha_H$ where $N = n + p$ [209]. The amplitude A_N is a scalar measure of the $1/f$ noise level and generally reflects the quality of a material or a device, depending on the number of charge carriers and extrinsic parameters such as device channel area and structural and chemical condition of the material: a higher value of A_N usually corresponds to a lower quality device. By comparing devices of similar area as

fabricated from a common material with a common process, we can assume the number of carriers to be roughly comparable across the devices as well.

The A_N and γ values for all devices were calculated by fits to linear portions of the data (generally between 0.01 and 0.5 Hz) shown in Figure 4.4. The objective was not to obtain a rigorously valid exponent, but rather to gain a qualitative sense of the low-frequency noise in the broadest spectral range with minimal sensitivity to narrow band features or higher frequency components (Table 4.5). The wide range of variability in γ is

Table 4.5: The 1/*f* current noise spectra parameters (Hooge and gamma) for pristine and functionalized graphene (open slots indicate devices missing (printing flaws) due to processing issues), and channel-area normalized noise from an extrapolation to 10 Hz. Previous work of Rumyatsev et al. [184] reported channel-area normalized noise ranges between 1×10^{-8} and 1×10^{-7} $\mu m^2/Hz$; values here within that range are shaded (see text).

		A_N		γ		S_V/V^2*L*W_{eff} @ 10 Hz ($\mu m^2/Hz$)	
Group	**Device**	**Pristine**	**Function-alized**	**Pristine**	**Function-alized**	**Pristine**	**Function-alized**
Group 1	U	2.61E-13	5.59E-13	1.8	1.7	5.96E-10	1.61E-09
	I_1	1.86E-11		2		3.68E-09	
	I_2	1.26E-10		1.9		6.57E-08	
	I_3	5.72E-12		2		4.91E-10	
	I_4	1.35E-11		1.8		5.14E-09	
Group 2	H_1	6.02E-12	9.92E-12	1.4	1.3	1.90E-08	3.94E-08
	H_2	7.46E-13	1.30E-12	1.4	1.3	3.58E-09	7.85E-09
Group 3	V_1	1.49E-10	8.18E-12	1	1.1	1.90E-07	8.27E-09
	V_2	3.71E-09	4.51E-10	1.1	1.2	3.22E-06	3.11E-07
Group 4	MS	2.73E-11	6.22E-12	1.4	1.3	9.07E-08	2.60E-08
	MC	3.34E-11	1.29E-11	1.5	1	9.81E-08	1.20E-07
	ME_7	1.88E-11	1.22E-12	1.7	1.8	2.74E-08	1.41E-09
	ME_2	1.04E-12	6.60E-13	1.5	1.5	4.03E-09	2.56E-09

unexpected, indicative of the wide range of possible effects which contribute to noise in these devices. Most researchers reported variability in γ for monolayer graphene devices, but values are near 1 [221-224]. The high values observed here for the largest, unmodified film devices U and I_1-I_4 indicate a large number of slow processes of duration longer than $1/2\pi f$ for frequencies below 1 Hz. The large size of these devices and the extended data acquisition to low frequencies may allow other processes to occur and be observed that have not previously been considered. For comparison of our observed noise to other published work, e.g., Rumyantsev et al. [189], we extrapolate the $1/f$ fit to 10 Hz, where our data is dominated by Johnson noise, and multiply the predicted value of S_V/V^2 by device length and effective width from tables 3.1 and 4.4 to obtain the values given in Table 4.5. In the work of Rumyantsev et al., a similar analysis of multiple, albeit considerably smaller, devices fabricated from exfoliated graphene under a controlled back-gate bias of 0V concluded that area-normalized noise at 10 Hz fell between 1×10^{-8} and 1×10^{-7} $\mu m^2/Hz$. In comparison, we find a generally consistent and systematic variation: Group 1 devices exhibit greatly reduced noise, Group 2 devices exhibit marginally reduced noise, Group 3 devices exhibit increased noise, and Group 4 devices exhibit a wide range of noise levels, overlapping the range of Rumyantsev et al.

To investigate which device feature influences noise the most, we studied the dependence of $1/f$ noise on device geometry, functionalization, effective graphene area, metal contact area, and mesa etched graphene perimeter. The areas and perimeters (internal and external) of graphene mesas measured after etching and metal contact areas were calculated for the geometries shown in Figure 3.1 and described in Table 3.1. From an

inspection of Figure 4.4, it is evident that functionalization generally lowers noise in all but the H_1, H_2, and U devices. These three are also the quietest devices, implying that the factors contributing to noise, and passivated by functionalization, are not present in certain devices (H_1, H_2, and U) but exist in others, specifically V_1, V_2, MC, MS, ME_2, and ME_7. Consideration of these device geometries suggests that while a single trap/excitation, generation/recombination, adsorption/desorption, etc., event can simultaneously induce changes in mobility and carrier concentration $\delta\mu_n$, $\delta\mu_p$, δn, and δp equivalently in the H_1, H_2, and U devices, such changes are *not* equivalent in the V_1, V_2, MC, MS, ME_2, and ME_7 devices, where considerable graphene is spatially remote from the primary transport paths. Thus, the direct effect on mobility through the regions defined as direct paths between electrodes from events outside those paths is minimal while generated charges can easily diffuse into the areas of current flow where drift mobility (and thus, scattering events) are significant. The ME_2 is somewhat exceptional. However, the sparser hole array relative to the MS and MC devices and reduced internal perimeter relative to the low field, high carrier concentration area as compared to the ME_7 device may explain the observed results. These results suggest a rather complex relationship here between mobility and carrier concentration.

In an effort to look for correlations between measurable parameters of graphene area, contact area, and active device perimeter, and noise parameterization terms A_N and γ, we present plots of these in Figures 4.5 (A_N) and 4.6 (γ) for the two sets of devices, pristine and functionalized graphene. Graphene area and perimeter for each device was calculated from the mask data. Contact area was calculated from the width of metal contacts and the

transfer length presented in Table 4.1. There is no strong evidence for correlation with device active (graphene) area or contact area of noise scalar A_N. If one neglects the four interdigitated devices, where the relatively high currents and negligible perimeter relative to area suggests different relevant physical phenomena, there may be a correlation between

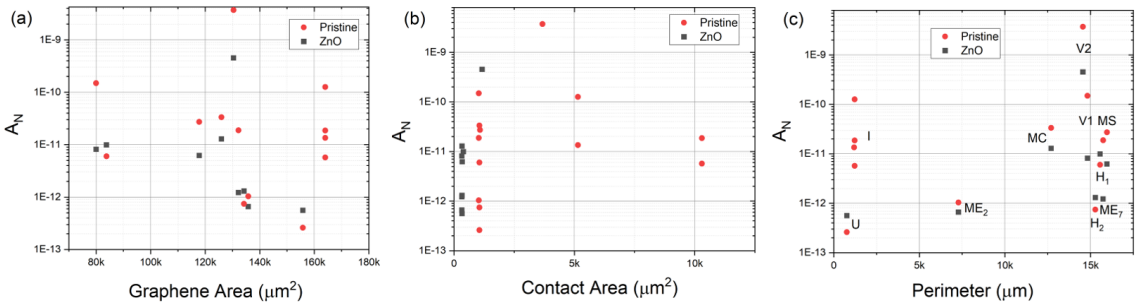

Figure 4.5: Noise scalar A_N plotted against a) graphene area, b) contact area, and c) total perimeter, for both pristine and ZnO functionalized graphene devices.

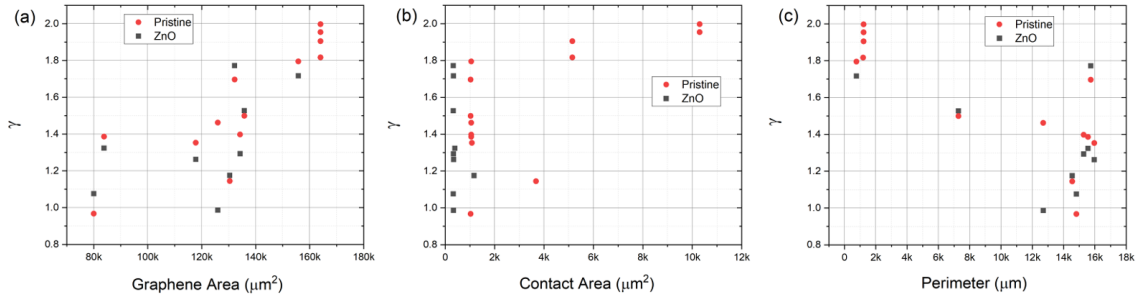

Figure 4.6: Frequency exponent γ plotted against a) graphene area, b) contact area, and c) total perimeter, for both pristine and ZnO functionalized graphene devices.

perimeter and noise scalar A_N. We do see strong correlations between device area and γ and contact area and γ, and an inverse correlation between perimeter and γ. This strongly suggests different mechanisms exist in the generation of noise in the different regions of the film, which can be used to improve sensor design.

Ultimately, the question of which is the optimal sensor design is still unsettled. Although in this work we have addressed the relationship of design to intrinsic device noise, we have not fully examined the relationship of design to extrinsic signal, i.e., chemiresistive response. It may be the case that the noisiest device geometries are also the most sensitive. In any case, a characteristic and reproducible response behavior defined as change in conductance should be achieved rapidly. Furthermore, the design of the sensor should strongly favor detecting perturbations in conductivity induced by adsorption of target species over others. Perturbations due to background or benign chemicals, which are also considered to be noise, should be minimized. Finally, nanoparticles other than 50 - 80 nm dia. ZnO may have different impacts on noise and sensor response. These factors will be explored in future work.

4.4 Conclusions

We have carried out measurements of resistance and low-frequency noise in graphene devices to determine the effects of ZnO nanoparticles functionalization and the engineered defects of the graphene channel. The goal of our work was to understand which device is best suited for chemiresistive sensing applications. For comparison purposes, all of the devices studied had the same graphene mesa area, but with different defects patterns

of interdigitation or etched internal holes. These hole patterns included arrays of coarse and fine long slots etched perpendicular and parallel to the applied field, and two-dimensional arrays of squares, circles, and few and many pointed stars. We find that, functionalization generally lowers noise, with the exceptions being the three quietest devices (H_1, H_2, and U), implying that the factors contributing to noise, and passivated by functionalization, are not present in some geometries but exist in others. The resistance measurements showed that devices with long etched stripes orthogonal to the direction of the applied electric field have the highest resistance, and short and wide channel interdigitated devices have the lowest resistance for both pristine and ZnO functionalized graphene. The graphene-metal Ohmic contact resistances (R_C) demonstrate that ZnO functionalized graphene has lower contact resistance, but higher graphene sheet resistance (R_{sh}) compared to the pristine graphene. There is no strong evidence for a correlation between the scalar noise power and actual graphene channel area, contact area, and total perimeter (including the internal etched hole perimeters). However, there is a strong direct correlation between noise frequency dependence and graphene area and contact area. Furthermore, there is an inverse correlation between noise frequency dependence and perimeter. This work highlights that the electrical and low frequency noise measurements are critical for the selection of appropriate device structure in graphene/ZnO chemical sensors.

CHAPTER 5 : GRAPHENE BASED CHEMICAL SENSOR DEVICES FOR PRECISE SULFUR DETECTION: EXPERIMENTAL RESULTS AND DENSITY FUNCTIONAL THEORY MODELING

5.1 Introduction

Proton Exchange Membrane (PEM) fuel cells are envisioned for generating electricity and heat from natural gas, biomass, and other hydrocarbon fuels because of their intrinsic low noise and environmentally clean and high efficiency operation [226]. Several military applications are considered, such as unmanned aerial vehicles (UAVs), unmanned ground vehicles (UGVs), auxiliary power units and portable power systems for silent camp and silent watch operations, as well as operation on submarines and ships [227-229]. JP8, a widely available fuel used for military aviation, can provide the necessary hydrogen to PEM systems, but it can contain up to 700 parts per million (ppm) of sulfur [230], hindering its direct use as a hydrogen source. Sulfur must be removed from fuel before use in PEM fuel cells as it poisons the reformer catalyst, degrading efficiency and eventually requiring replacement. Desulfurizers are effective, but they eventually saturate and allow sulfur to bleed through. In order to continuously monitor the fuel desulfurization process stream, a low-cost but highly sensitive sulfur content monitoring device is needed.

In the development of new point-source, chemiresistive sensing technologies since 2004, graphene, a honeycomb network of sp^2-hybridized carbon atoms [231], has proven an excellent performer. The properties of graphene that make it ideal for gas sensing applications include its high surface-to-volume ratio, high mobility (~200,000 cm^2/V_s), low electrical noise characteristics, low room temperature contact resistance, mechanical

strength, and general non-reactivity [25-27, 232-236]. Charge transport through graphene is highly sensitive to molecular adsorption, resulting in a change in conductance [192]. Additionally, single molecules of a target gas can be reacted with the atoms in the graphene sheet [193]. These features make graphene an ideal material for detecting gas molecules. Graphene has demonstrated high sensitivity to NO_2, NH_3, H_2, CO_2, SO_2 and H_2S, responding to part-per-billion concentrations [237-249]. The selectivity of a sensitive chemical sensor is nevertheless a challenge, given the wide range of species that can affect film conductivity and the subsequent aggregate film behavior in a complex ambient [143, 146, 194-195, 250]]. In principal, the use of similar but effectively different sensors with different specific responses is one path towards realizing specificity.

In this chapter, we report the results of an investigation comparing the vapor response of two different chemical vapor sensors, one based on pristine epitaxial graphene and a second of ZnO nanoparticle-functionalized graphene. Zinc oxide nanoparticles are among the most studied nanomaterials for chemical sensing because of their high thermal and chemical stability, reduced toxicity, optimal conductivity, low cost, and availability in a variety of morphologies [71-72]. Zinc oxide is an n-type semiconductor with a wide band gap energy of 3.37 eV. It has previously been demonstrated that ZnO nanoparticles alone, as well as when combined with graphene, have a high sensitivity to gases such as methane, nitrogen dioxide, hydrogen, ammonia, ethanol, and acetone [70, 211-212]. We used thiophene (C_4H_4S) and 1-octane thiol ($C_8H_{17}SH$) to represent two chemically distinct sulfur configurations, and an aliphatic hydrocarbon, decane ($C_{10}H_{22}$), and an aromatic hydrocarbon, propyl benzene ($C_3H_7C_6H_5$), to represent components of hydrocarbon fuels.

To further understand the experimental results, Quantum Espresso software was used to generate first-principles calculations within density function theory (DFT) and create molecular models of adsorbate/surface systems and so simulate the device geometry, adsorption energy, and density of states. The DFT provides information about the atomic geometries and the nature of chemical bonding and is thus an invaluable tool for understanding surface adsorption by providing accurate energetic and electronic characteristics [251-254]. To our knowledge, however, DFT calculations and analyses of the sensing capability of hydrocarbon and sulfur-containing chemical compounds by metal oxide decorated graphene surfaces have not been carried out. The primary goal here is to develop a general understanding of the adsorption and effects of sulfur and fuel compounds on conductivity of pristine graphene and metal-oxide particle functionalized graphene chemiresistive sensors.

5.2. Materials and Methods

5.2.1 Graphene growth, Fabrication and Functionalization

Details on the growth of graphene films on the Si-face of a semi-insulating, on-axis 6H-SiC substrate by sublimation of silicon; the etch process used for forming 400×400 μm^2 graphene mesas, and the procedure used for forming Ti/Au (10 nm/100 nm) ohmic contacts, and ZnO nanoparticle functionalization (50 – 80 nm, US Research Nanomaterials Inc.) by means of an N-ethylamino-4-azidotetrafluorobenzoate linker molecule were given elsewhere [182-186]. More detailed information on the graphene growth, device fabrication and functionalization is presented in chapter 3. Hall measurements on special

test structures of the pristine graphene indicated p-type conductivity with a carrier mobility and a sheet carrier concentration of 1047 $cm^2/(V \cdot s)$, and 1.42 x 10^{12} cm^{-2}, respectively. More detailed results on material and contact resistance and noise are reported elsewhere [255]. The device structure used in this work is given in Figure 5.1. The analyte materials used here, decane, propyl benzene, thiophene, and octanethiol, were obtained at reagent grade purity (≥ 98%) from Sigma-Aldrich and used as received.

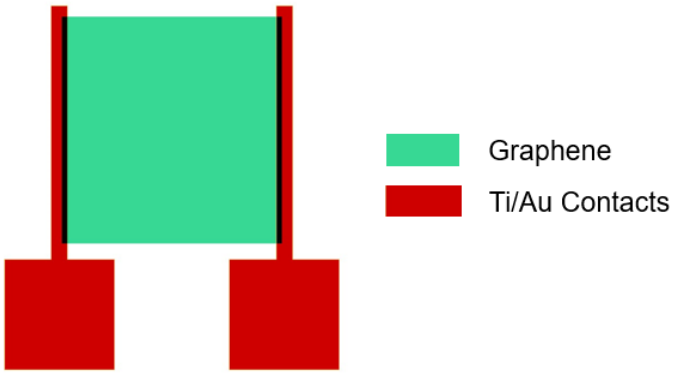

Figure 5.1: Computer-aided design (CAD) schematic of the device geometry selected for chemical vapor testing. The unpatterned graphene device has a channel length of 380 µm and channel width of 410 µm.

5.2.2 Instruments and Experimental Setup

Each device of four tested in parallel was contacted with a pair of Au-coated W probes on a conventional probe station connected to a computer-controlled SR830 DSP lock-in amplifier (LIA). One of each pair of probes is connected to a low impedance ac voltage source $V_s = 0\ V_{dc} + 0.1\ V_{ac,\ rms}$ with a frequency *f* on the order of 10 kHz, a slightly different frequency for each device. The other probe is connected to a grounded bias

resistor R_b of 10 kΩ to roughly divide the voltage V_s and give a maximum voltage drop across R_b to be measured by the LIA (10 MΩ || 25 pF input impedance) at *f*. In this way, the small changes ΔV measured across each R_b can be converted to small changes in the differential conductivity $(G-G_0)/G_0$ of multiple devices on the same substrate with high signal-to-noise ratios and excellent cross-talk rejection. We monitored the sample temperature with a 3 mil thermocouple contacting the surface of the substrate.

During this experiment, devices under test (DUT), all on a single chip, were continuously exposed to a stream of dry air (dew point: − 40°C) at 4.8 lpm directed from close range into open air. One or more vapors were generated by bubbling streams of dry 99.9999% N_2 at 0-100 standard cubic centimeter per minute (sccm) through glass frits immersed in approximately 15-25 ml of reagent-grade analyte as independently controlled by mass flow controllers (MFC). To reduce the possibility of liquid condensation in the solenoid valve directing the vapor to the DUT, the streams, generally assumed to be saturated, were mixed with a constant 200 sccm flow of N_2. When directed to the DUT and mixed with the dry air stream, this technique generates a range of analyte and interferent dilutions between 0.002 and 2% from equilibrium vapor pressure at slightly over 5 lpm. Vapor concentration was checked with a Hiden model HPR-20 QIC residual gas analyzer configured with differential pumping in order to sample volumes at atmospheric pressure.

The procedure for testing the device is as follows. Prior to each measurement, the chip was heated on a hot plate in air at 125 °C for 5 min to induce thermal desorption from and regeneration of the surface. Then, the chip is cooled in air for at least 5-7 minutes and allowed to equilibrate back to room temperature (22-25 °C). The data collection process

had the following steps: a) 200 s to establish baseline, b) a pulse sequence, typically five pulses 60s on, 60s off, wherein the solid valve directs air either into the mixer ("on") or to the system exhaust ("off") c) LIAs, substrate temperature, and bubbler temperature sampled synchronously at ~ 4Hz and d) vapor composition monitored asynchronously in parallel.

5.3. Computational Methods and Model Systems

5.3.1 Computational Methods

All the first-principles calculations have been performed using BURAI 1.3, a GUI of Quantum Espresso, within density functional theory (DFT) in the Kohn-Sham approach [256]. This graphical user interface (GUI) system was developed as a JavaFX application and requires a Java Runtime Environment (JRE). The exchange-correlation energy functional calculations were achieved by utilizing the Generalized Gradient Approximation (GGA) in the Perdew, Burke, and Ernzerhof (PBE) technique [257], which adopts double numerical basis sets polarization functions. In GGA, it is well known that the equilibrium distance between the adsorbate and graphene sheet will be underestimated, resulting in an underestimation of binding energy, but valuable results can still be obtained within this framework [258]. An ultra-soft pseudopotential with nonlinear core corrections was used, and a cutoff for wavefunctions and charge density was set as 25 Ry and 225 Ry, respectively, which is demonstrated to be the most important parameter for computing effort and accuracy. The convergence criterion for electronic optimization of the self-consistent field (SCF) was set to 1.0×10^{-4} Ry using unpolarized spins. A 6×6×1 symmetric

Fermi vacuum k-point grid was used to calculate the total energy and electronic density of states (DOS). Solid state physics and condensed matter physics define density of states (DOS) as the proportion of states to be occupied by a system at any given energy [259]. The density of states is defined as $D(E) = N(E) / V$, where $N(E)\delta E$ is the number of states in the system of volume V whose energies lie in the range from E to $E + \delta E$ [259]. The distribution can be expressed mathematically as a probability density function, which is an average over the various system states' space and time domains. In addition, projected density of states gives the projection of particular orbital of particular atom on the density of states. In other words, the sum over all the projections, which will have the total density of state (TDOS), or simple the DOS [259]. Furthermore, Gaussian smearing was defined as Fermi vacuum occupancy, and the smearing width was 1.0×10^{-2} Ry. The optimized configurations for the surface/adsorbate pairs were obtained by placing relaxed molecules ~3 Å above the surface and optimizing the systems using the Broyden-Fletcher-Goldfarb-Shanno (BFGS) algorithm [260]. All atomic positions were completely relaxed until the forces in each atom were less than 5.0×10^{-3} Ry/Bohr and the energy of the atomic system obtained in the SCF calculation was less than 3.0×10^{-4} Ry. All calculations were performed at 293 K. The adsorption energy of chemical species adsorbed on the graphene or metal-oxide nanosheet is then evaluated by the following formula:

$$E_{(adsorption)} = E_{(surface + molecule)} - E_{(surface)} - E_{(molecule)} \quad (5.1)$$

where $E_{(surface + molecule)}$ is the total energy of the adsorption system, $E_{(surface)}$ is the energy of the isolated graphene or metal-oxide nanosheet, and $E_{(molecule)}$ is the energy of isolated chemical molecules. A shift in adsorption energy in the negative direction will result in

more favorable adsorption, indicative of stronger interaction between the adsorbate (molecule) and adsorbent (nanosheet).

5.3.2 Model Systems

The unit cells used in the configuration of the planar films of graphene (hexagonal) and ZnO (wurtzite) were taken from the website "American Mineralogists Database" [261]. The considered graphene was simulated by a one-layer of 24 (24 C atoms) form by placing 2×1 unit C cells along the x, and y axes. A similar supercell was used for simulation for the ZnO nanosheet by a one-layer slab of 35 atoms (18 Zn, 17 O) formed by placing

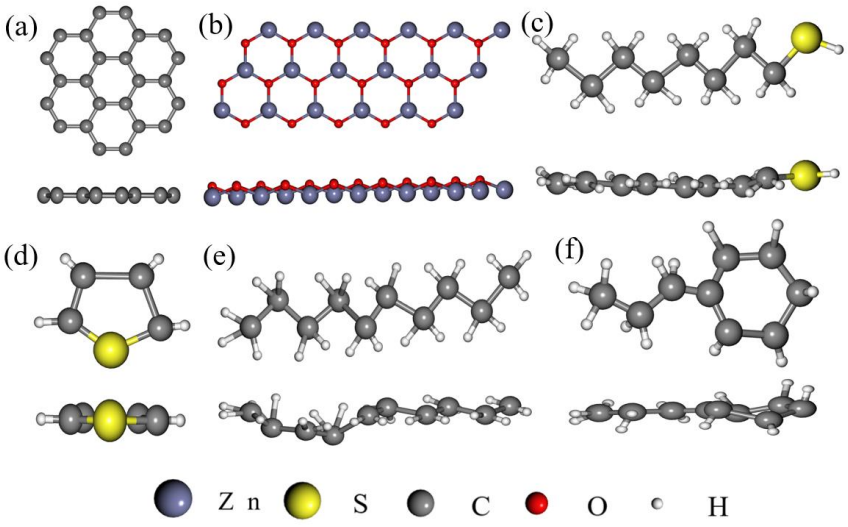

Figure 5.2: Optimized geometry top and side view of (a) graphene, (b) ZnO nanosheet, (c) octanethiol, (d) thiophene (e) decane, and f) propyl benzene. The light blue spheres are Zn atoms. The yellow and grey spheres denote S and C atoms, respectively. Red and white spheres represent O and H atoms, respectively.

2×1 unit ZnO cells along the x, and y axes. The octanethiol, thiophene, decane, and propyl benzene nanostructures containing and 27 (8 C, 18 H and 1 S atoms), 9 (4 C, 4 H and 1 S atoms), 32 (10 C and 22 H atoms) and 21 (9 C and 12 H atoms) atoms, respectively, were draw manually for simulation. All atoms of the considered model structure had been relaxed. The optimized structures of graphene, ZnO, octanethiol, thiophene, decane, and propyl benzene are shown in Figure 5.2. Monolayer wurtzite ZnO is composed of threefold coordinated Zn and O atoms on the surface and, thus, exhibits unsaturated bonds which provide strong interaction with gas molecules [262]. It is mainly the neighboring atoms which determine the characteristics of interactions with adsorbing molecules.

5.4. Results and Discussion

5.4.1 Chemical Vapor Sensing

Conductivity data was collected during exposure of pristine graphene and ZnO functionalized graphene sensors to at least two concentrations each of decane, propyl benzene, thiophene, and octanethiol. The measured baseline (initial) resistance values on the devices before exposure at each concentration are Table 5.1. Sensor response was calculated from

$$\text{Response} = \frac{G - G_0}{G_0} \tag{5.2}$$

where G_0 is the conductance of the device prior to exposure to the target vapor and G is the

Table 5.1: The baseline resistance ($1/G_0$) of the device immediately prior to each experiment.

Thiophene					
Concentration (ppm)	88	97	270	340	460
Pristine (kΩ)	5.89 ± 0.62	5.46	5.35 ± 0.29	5.44 ± 0.18	6.38 ± 0.64
ZnO (kΩ)	6.15 ± 0.93	6.47 ± 0.63	6.78 ± 1.60	6.79 ± 1.18	10.01 ± 0.54

Octane Thiol					
Concentration (ppm)	0.2	0.4	0.6	1.1	2.7
Pristine (kΩ)	6.38	6.93 ± 0.45	6.95 ± 0.92	6.24	5.79
ZnO (kΩ)	9.15 ± 3.12	14.27 ± 3.64	8.08 ± 3.79	7.68 ± 3.07	8.91 ± 2.98

	Decane		Propyl Benzene	
Concentration (ppm)	3.2	32.3	3.4	8.4
Pristine (kΩ)	5.34 ± 0.54	5.48 ± 0.51	6.08 ± 0.51	6.85 ± 0.72
ZnO (kΩ)	5.86 ± 0.76	7.74 ± 2.42	6.24 ± 2.92	6.04 ± 2.54

conductance after 60 seconds exposure. Precise values used for subsequent calculation of average and standard deviation of response were reached by fitting a linear model to the measured voltage over the last 40 seconds of each exposure, and interpolating to establish a value at 60 seconds. In each experiment the measurement duration was 800 seconds (100 seconds setup time, five cycles of 60 seconds on and 60 seconds off, and 100 seconds recovery time). The responses of the pristine and ZnO functionalized graphene sensors as a function of the thiophene and octanethiol vapor concentrations are shown in Figure 5.3 and Figure 5.4, respectively. As shown in Figure 5.3(a) and Figure 5.4(a), the pristine graphene sensors show a negative response and ZnO functionalized graphene sensors show a positive response to thiophene and octanethiol vapors. The response of both samples shows a nearly linear dependence on the thiophene vapor concentration at the lower concentration region (88 ppm to 340 ppm with the thiophene vapor and 0.2 ppm to 0.6 ppm

with the octanethiol vapor), as shown in Figures 5.3(b) and 5.4(b), and Table 5.2. It is found that the ZnO functionalized graphene devices exhibited a higher response magnitude than the pristine graphene devices to the same vapor concentrations.

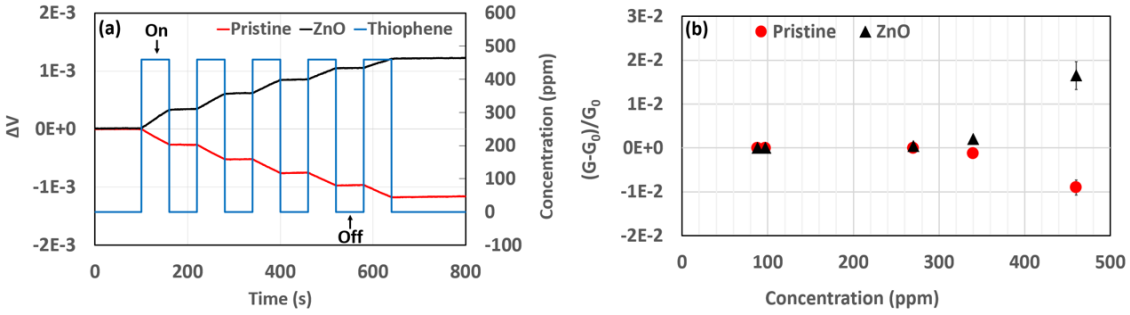

Figure 5.3: (a) Sensor response of the pristine graphene and ZnO functionalized graphene devices to thiophene at 460 ppm for five exposure on-off cycles (b) Mean and standard deviation of sensor response of the devices for varying concentrations of thiophene vapor at room temperature.

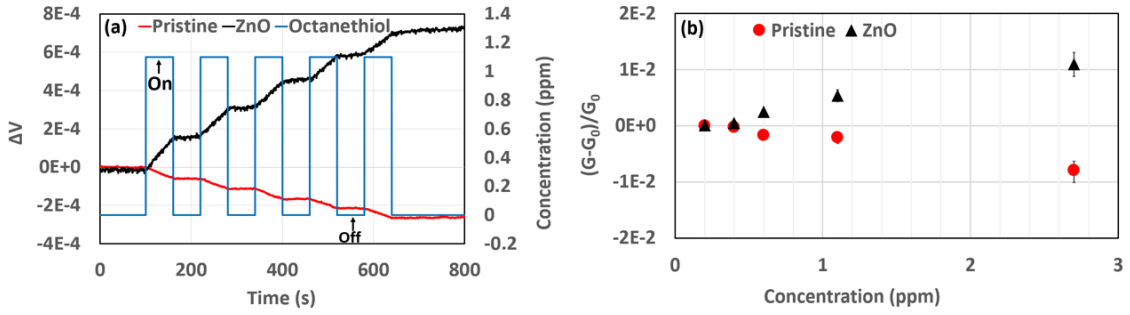

Figure 5.4: (a) Sensor response of the pristine graphene and ZnO functionalized graphene device for one concentration of octanethiol at 1.1 ppm for five exposure on-off cycles. (b) Mean and standard deviation of sensor response of the devices for varying concentrations of octanethiol vapor at room temperature.

Table 5.2: Sensor response, $(G-G_0)/G_0$, with standard deviation of the pristine graphene and ZnO functionalized graphene vapor sensors for thiophene and octanethiol vapor.

	Thiophene (ppm)				
Concentration	88	97	270	340	460
Pristine	$-3.09\times10^{-5} \pm 4.97\times10^{-5}$	$-7.44\times10^{-5} \pm 5.25\times10^{-5}$	$-9.76\times10^{-5} \pm 1.50\times10^{-4}$	$-1.25\times10^{-3} \pm 2.32\times10^{-4}$	$-9.05\times10^{-3} \pm 1.74\times10^{-3}$
ZnO	$3.21\times10^{-5} \pm 7.62\times10^{-5}$	$8.02\times10^{-5} \pm 8.56\times10^{-5}$	$4.53\times10^{-4} \pm 1.95\times10^{-4}$	$2.03\times10^{-3} \pm 4.11\times10^{-4}$	$1.65\times10^{-2} \pm 3.16\times10^{-3}$
	Octanethiol (ppm)				
Concentration	0.2	0.4	0.6	1.1	2.7
Pristine	$-4.65\times10^{-5} \pm 3.54\times10^{-5}$	$-2.40\times10^{-4} \pm 8.95\times10^{-5}$	$-1.71\times10^{-3} \pm 3.78\times10^{-4}$	$-2.06\times10^{-3} \pm 3.94\times10^{-4}$	$-7.96\times10^{-3} \pm 1.61\times10^{-3}$
ZnO	$8.47\times10^{-5} \pm 1.02\times10^{-4}$	$4.32\times10^{-4} \pm 9.13\times10^{-5}$	$2.44\times10^{-3} \pm 4.89\times10^{-4}$	$5.35\times10^{-3} \pm 1.07\times10^{-3}$	$1.09\times10^{-2} \pm 2.14\times10^{-3}$

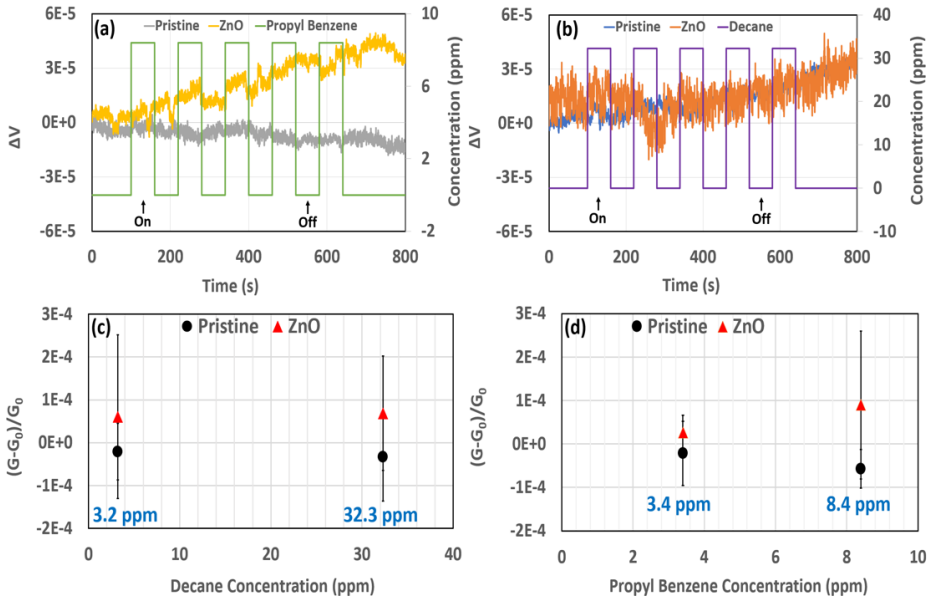

Figure 5.5: Sensor response of the pristine graphene and ZnO functionalized graphene device for one concentration of (a) decane at 32.3 ppm and (b) propyl benzene at 8.4 ppm. Mean and standard deviation of sensor response of the devices as calculated from measurements of response to five exposures for (c) decane and (d) propyl benzene.

Neither sensor indicated any significant conductance response toward decane, or propyl benzene vapors as shown in Figure 5.5. Figures 5.5(c) and 5.5(d) show the sensor responses to decane and propyl benzene vapor concentrations, respectively, with response mean and standard deviation values generated from measurements of five exposures.

5.4.2 Adsorption of molecules on graphene and ZnO nanosheet

Various adsorption configurations were considered for each adsorbate/nanosheet pair. The most stable (i.e., highest adsorption) configurations are shown in Figure 5.6 and Figure 5.7. When thiophene and octanethiol molecules are adsorbed on graphene, there is very little interaction between the adsorbate and the nanosheet. In comparison, the

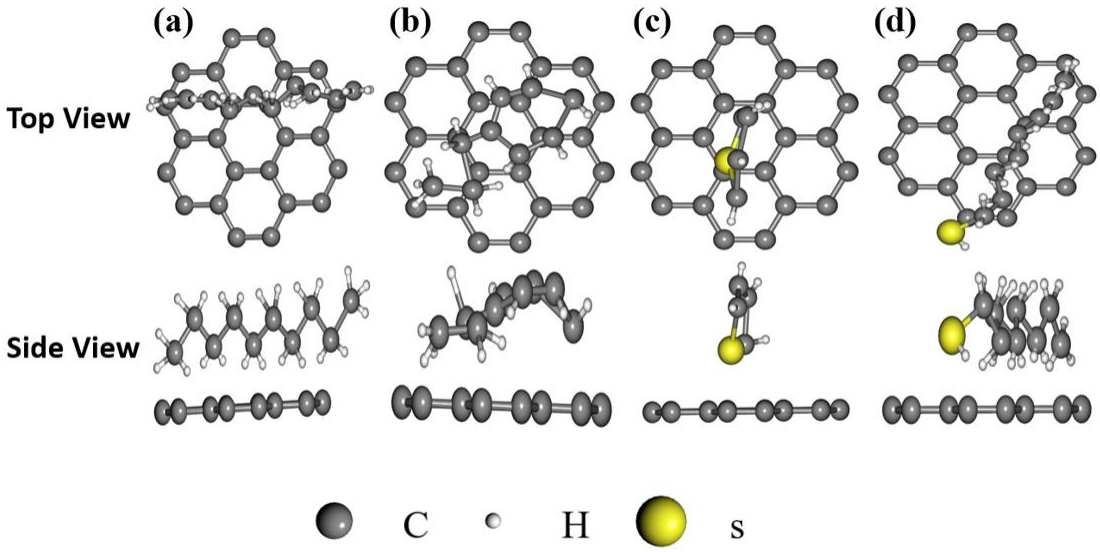

Figure 5.6: Side and top views of the most stable adsorption configurations of (a) decane, (b) propyl benzene, (c) thiophene, and (d) octanethiol on graphene. Grey, white, and yellow spheres denote C, H, and S atoms, respectively.

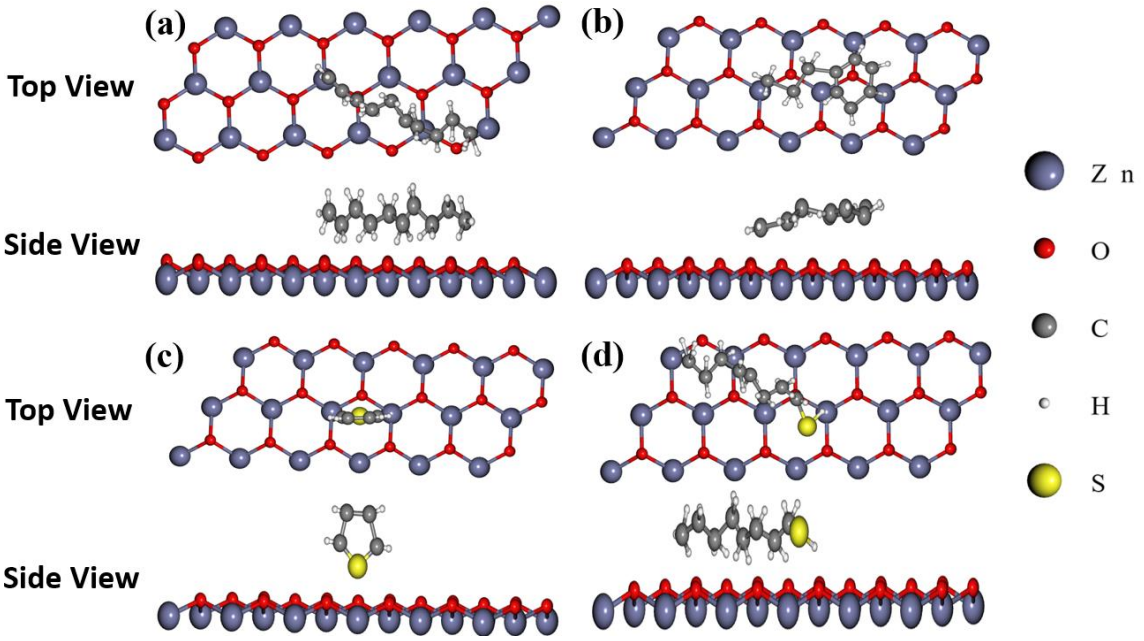

Figure 5.7: Side and top views of the most stable adsorption configurations of (a) decane, (b) propyl benzene, (c) thiophene, and (d) octanethiol on ZnO nanosheet. Light blue, red, grey, white and yellow spheres denote Zn, O, C, H, and S atoms respectively.

geometry optimization process indicates that the C-H, C-S and S-H bonds of the adsorbed thiophene and octanethiol molecule are stretched after adsorption on the ZnO surface of the nanosheet. This happens due to electron density transfer between the Zn-O (ZnO) and C-H, C-S and S-H (C_4H_4S, $C_8H_{18}S$) bonds at the point of interaction between Zn and S. The calculated molecular bond length and bond angle distortion in the ZnO nanosheet are significantly higher than the graphene, generating broken bonds and pores in the ZnO nanosheet. The ZnO nanosheet appears to envelop the thiophene and octanethiol molecules as shown in Figure 5.8. On the other hand, neither decane nor propyl benzene molecules are significantly distorted, nor do they induce distortion, on either graphene or ZnO nanosheets.

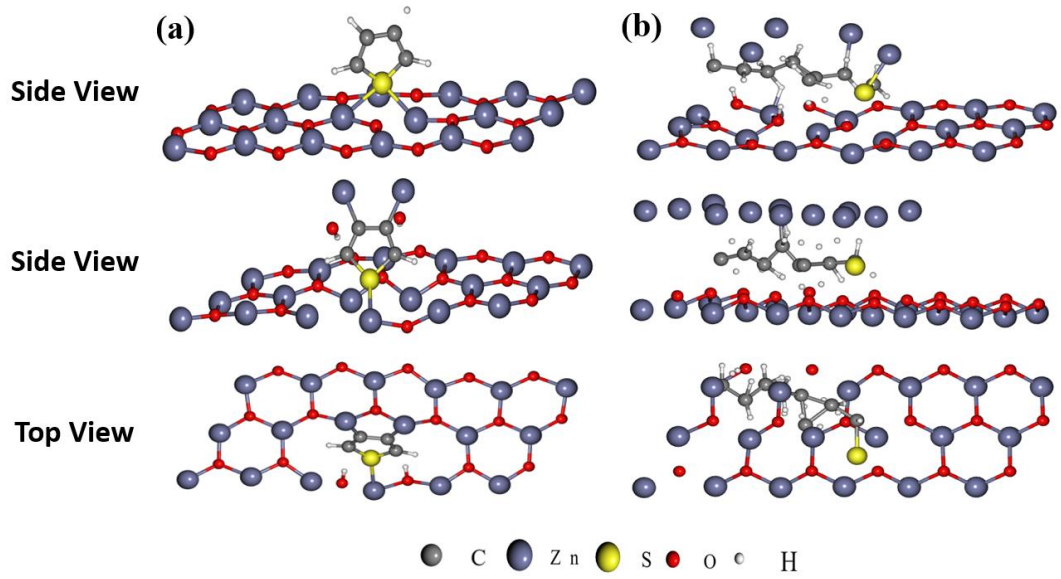

Figure 5.8: The adsorption configuration of (a) thiophene and (b) octane thiol on ZnO nanosheet. Figure shows (Side and top view) the molecular bond length and bond angle distortion and leave pores on the ZnO nanosheet surface. Light blue, red, grey, white and yellow spheres denote Zn, O, C, H, and S atoms respectively.

Self-consistent field (SCF) calculations were performed and allowed to converge for graphene and ZnO nanosheets considered with and without decane, propyl benzene, thiophene and octanethiol. For the graphene adsorption complexes, the decane, propyl benzene, thiophene, and octanethiol adsorption energies were calculated as 0.39 eV, 1.02 eV, -1.08 eV, and -3.62 eV, respectively. For the case of adsorption onto ZnO, decane, propyl benzene, thiophene, and octanethiol adsorption energies were calculated as 0.81 eV, 1.71 eV, -3.20 eV, and -5.76 eV, respectively. The adsorption energies for the four species onto the two surfaces are given in Table 5.3. The results show that the ZnO surface provides

a more energetically favorable adsorption site for thiophene and octanethiol than graphene. More importantly, a positive adsorption energy indicates that work is required to move molecules closer to the nanosheet surface, while a negative adsorption energy indicates charge transfer and possible molecular reconfiguration or surface reconstruction; the more negative means the more interaction, and the slower recovery after exposure. Hence, for a chemiresistive sensor to respond to vapor exposure the adsorption energy must be negative but not so negative as to irrecoverably saturate. This is consistent with our observation that, relative to pristine graphene, ZnO functionalized devices are faster in their response to thiophene and octanethiol and slower in recovery.

Table 5.3: Adsorption energy values for decane, propyl benzene, thiophene and octanethiol molecule adsorbed of graphene and ZnO nanosheet.

Adsorption energy (eV)	**Hydrocarbon Compounds**		**Sulfur-Containing Compounds**	
	Decane	Propyl benzene	Thiophene	Octanethiol
Graphene	0.39	1.02	-1.08	-3.62
ZnO Nanosheet	0.81	1.71	-3.20	-5.76

5.4.3 Electronic Structure

The density of states (DOS) is defined as the number of allowed electron/hole states per unit volume at a given energy, and the phenomenon of charge carrier transport in conductive solids largely depends on this parameter. To further investigate the adsorption of decane, propyl benzene, thiophene and octanethiol on the graphene and ZnO surfaces, the total and projected density of states were calculated for the observed adsorption

configurations. Figure 5.9 represents the total density of states (TDOS) for a graphene nanosheet before and after the adsorption of decane, propyl benzene, thiophene, and octanethiol molecules. A common zero point has been used for better comparison of the Fermi level energies of the adsorption complexes. Adsorption of sulfur compounds

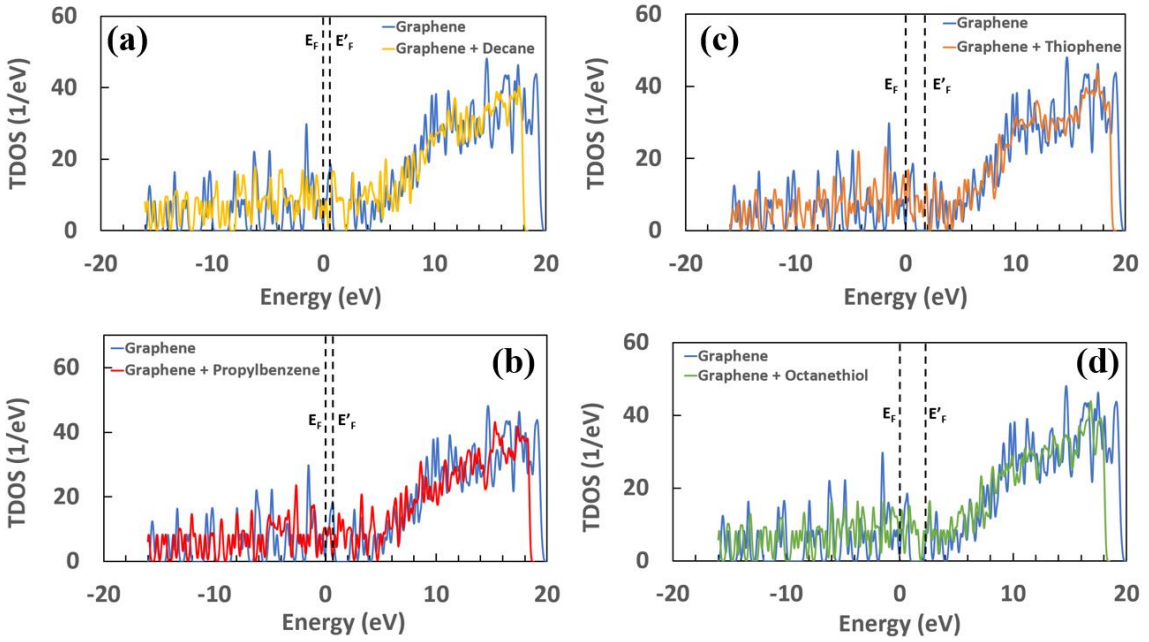

Figure 5.9: The total density of states for graphene before and after the (a) decane, (b) propyl benzene, (c) thiophene, and (d) octanethiol adsorption process. The Fermi energies of the graphene nanosheet before and after adsorption are denoted by E_F and E'_F, respectively.

displaces the Fermi level to a higher energy relative to the displacement induced by the pure hydrocarbons, indicative of a relatively higher transfer of charge into the film.

Specifically, the Fermi energy (E_F) of graphene is increased 2.12 eV after adsorption of octanethiol. Adsorption of decane, propyl benzene and thiophene was shown to induce E_F shifts of 0.63 eV, 0.81 eV, and 1.94 eV, respectively. The TDOS of the adsorbate/graphene structures showed small but finite differences in comparison with the isolated graphene structure, the most significant being the lowering of the vacuum level of the adsorbed system relative to the isolated graphene structures. Figure 5.10 shows the TDOS for ZnO nanosheet before and after the adsorption of decane, propyl benzene, thiophene and

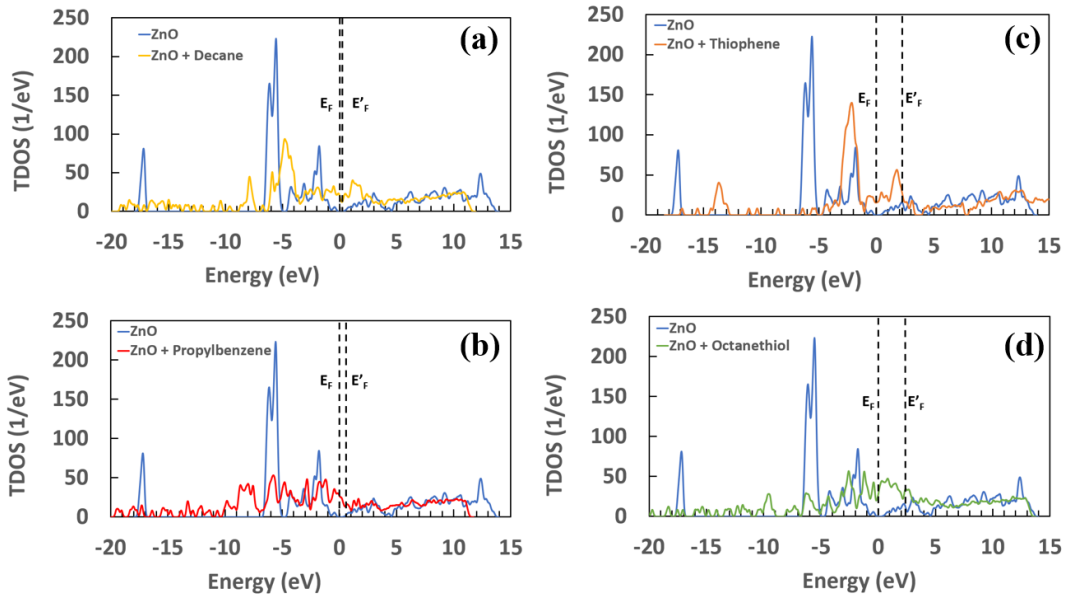

Figure 5.10: The total density of states for ZnO nanosheet before and after the (a) decane, (b) propyl benzene, (c) thiophene, and (d) octanethiol adsorption process. The Fermi energies of the ZnO nanosheet before and after decane, propyl benzene, thiophene and octanethiol adsorption are denoted by E_F and E'_F, respectively.

octanethiol molecules. We observed a shift of E_F to higher energy upon adsorption of all species studied. Relative to the case of adsorption onto graphene, the adsorption onto ZnO of hydrocarbons induced a smaller shift while the sulfur compounds induced a larger shift. Specifically, decane, propyl benzene, thiophene, and octanethiol induced E_F shifts of 0.24, 0.49, 2.22, and 2.39 eV, respectively. In contrast to the graphene structure TDOS, the TDOS of the ZnO nanosheet-thiophene and ZnO nanosheet-octanethiol complexes exhibit significant differences compared to the isolated nanosheet. These differences include both the change in peak energies and the appearance of several small peaks between -7 to -17 eV in the DOS of the considered adsorbed system. Due to these changes in energy of the states, the nanosheet electronic transport characteristics could be affected, and this fact can be used to produce vapor sensors in the adsorption process. Furthermore, adsorption moves E_F and also creates more states at the new E_F. These changes in state occupancy suggest the manner of change in the electronic transport properties of the films. Therefore, graphene and ZnO nanostructures are exposed to thiophene and octanethiol molecules, a larger change in conductivity is expected than the decane and propyl benzene.

The projected density of states (PDOS) representing the atomic contributions to the TDOS of the sulfur atom and a single C or Zn atom for the adsorption complexes of thiophene and octanethiol molecule with graphene and ZnO nanosheets was extracted from the Quantum Expresso calculation and is presented in Figure 4511. For comparison, the Fermi level energies of the adsorption complexes have been shifted to zero. The S of thiophene and octanethiol molecules shows significant overlap with Zn within the valence band. The overlap between the PDOS of these two atoms describes how the sulfur atom of

thiophene and octanethiol molecules forms a chemical bond with the ZnO nanosheet. Many small peaks were found with energy levels around the Fermi energy as well as the energy

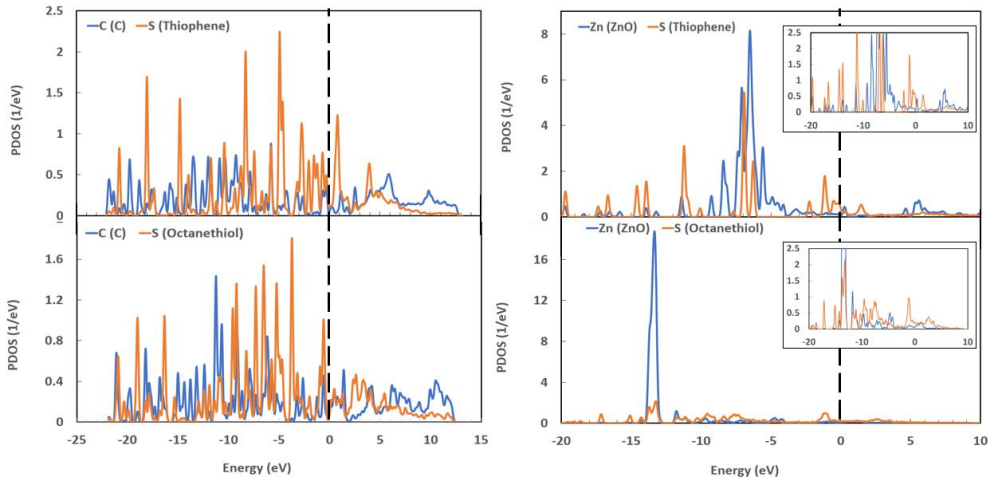

Figure 5.11: The projected density of states (PDOS) for the adsorption complexes of thiophene (upper) and octane thiol (lower) with a graphene (left) and ZnO (right) nanosheet. The Fermi energies of the adsorption complexes have been shifted to zero denoted by black dotted line. Inert (right) shows lower PDOS for comparison.

range of -5 to -15 eV, all attributable to this interaction. The overall PDOS results indicate chemisorption between the thiophene and octanethiol molecules and the ZnO nanosheet. As a result, substantial modification of electronic transport behavior can be expected within ZnO functionalized graphene structures at thiophene and octane thiol vapor exposure. Therefore, the obtained DFT calculation results support our experimental results.

5.5. Chemical Vapor Sensing Mechanism

We use a simple model to explain the different responses of pristine graphene and ZnO functionalized graphene based on effective doping. Our pristine graphene was found to be p-type with a carrier mobility μ of 1047 $cm^2/(V \cdot s)$, and a sheet carrier density N_s of 1.42 x 10^{12} cm^{-2} after device processing. After ZnO nanoparticle functionalization, the graphene/linker/ZnO system was observed to be n-type with carrier mobility μ of 1030 $cm^2/(V \cdot s)$, and sheet carrier density N_s of 6.33 x 10^{11} cm^{-2}. This indicates that the Fermi energies with respect to the band structure of pristine graphene and ZnO functionalized graphene are different (Figure 5.12(a)). The density of states in graphene is proportional to state energy $E \propto N_s$. Since the carriers are fermions, there are only two electrons per state, so the number of states is equal to ½ the number of electrons. A schematic illustration of the relationship between the resistance R and sheet carrier density N_s of graphene is shown in Figure 5.12(b) [263]. For the n-type ZnO functionalized graphene samples, the initial resistance point is on the left-hand side of the resistance peak, as shown in Figure 5.12(b) by the black circle. Adsorption of thiophene and octanethiol molecules involves electron transfer into the ZnO functionalized graphene system, leading to resistance shift away from the charge neutral point ($N_s = 0$) and consistent with movement of the Fermi level higher into the conduction band, as shown in Figure 5.10, and an increase in conductivity, as shown in Figure 5.3. On the other hand, in the case of the pristine graphene, the devices are p-type with the initial resistance point in the right side of the resistance peak (Figure

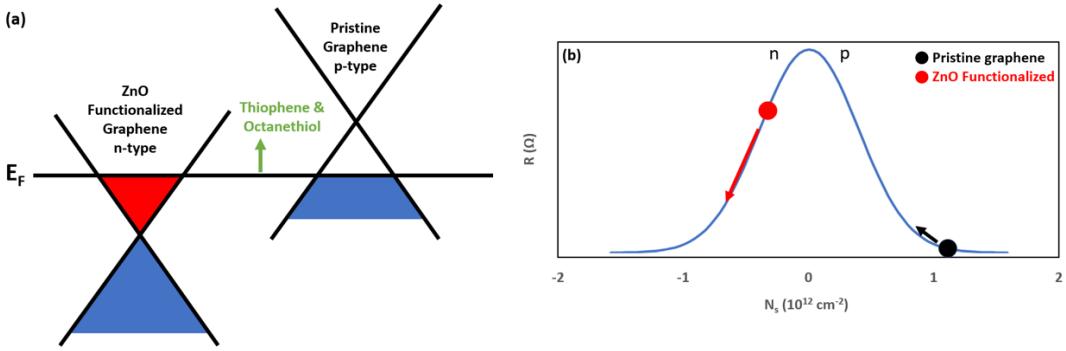

Figure 5.12: An illustration of (a) the Fermi level shift and (b) resistance due to thiophene and octanethiol doping for p-type pristine graphene and n-type ZnO functionalized graphene.

5.12(b)). Adsorption of thiophene and octanethiol molecules also induces electron transfer into the film, but here leading to a shift of the sheet carrier concentration closer to the charge neutral point (N_s = 0), the Fermi level towards the interband region (Figure 5.9), and to decreased conductivity (Figure 5.3). The change of resistance due to surface doping is smaller compared to the ZnO functionalized graphene samples.

5.6. Conclusion

The goal of our work was to understand which graphene sample (with and without ZnO functionalization) is best suited for chemiresistive sulfur sensing applications. In this paper, graphene formed by sublimation at high temperature on the Si-face of semi-insulating, on-axis 6H-SiC substrate was used as the sensor material. ZnO functionalized graphene was found to be a highly efficient sensor material for thiophene and octanethiol sensing. Moreover, density functional theory calculations were used to explain and verify

experimental results. Density functional theory calculations were performed to study the interaction of decane, propyl benzene, thiophene and octanethiol molecules with graphene (with and without metal oxide functionalization) to fully understand the detection properties of these nanosheets in adsorption processes. The results of the adsorption energy and TDOS (Fermi level shift) values show that ZnO offers a significantly more energetically favorable surface to adsorption of thiophene and octanethiol relative to hydrocarbons. Current and future researchers should benefit from the results of this simulation work in predicting metal-oxide catalyst particles that may be suitable for manufacturing highly selective chemical vapor sensors using graphene.

CHAPTER 6 : EFFECTS OF DEVICE GEOMETRY ON THE PROPERTIES OF GRAPHENE BASED CHEMICAL VAPOR SENSING DEVICES

6.1 Introduction

Gas/vapor sensors have a significant role to play in many different application fields, including environmental monitoring, industrial manufacture, medical diagnosis, military, and aerospace use [264-266]. Meanwhile, the materials used to construct gas/vapor sensors have a great impact on their combined properties, such as sensitivity, selectivity, and stability. Even though solid state gas/vapor sensors [267-271] have many advantages, such as small size, low power consumption, high sensitivity, and low cost, to makes them a desirable option for sensing very low concentrations of gases involving parts-per-million (ppm) levels, but they have significant short term instability issues as well as limited measurement accuracy [272]. Utilizing novel nanostructures as sensing elements, nanotechnology provides a variety of opportunities for developing the next generation of gas detectors with enhanced sensor performance, including high sensitivity at extremely low concentrations, high selectivity, fast response and recovery times, and room-temperature operation [273-276]. Among them, a trend towards graphene-based gas/vapor sensors has recently gained intense attention due to its atom-thick two-dimensional (2-D) structure and excellent properties of graphene sheets [277-281].

Graphene, a two-dimensional form of sp^2 carbon has been considered as a promising material for gas/vapor sensing applications due to its large surface area per unit volume, high electrical conductivity, extraordinary carrier mobilities, exceptional mechanical strength, low contact resistance, and extremely low 1/f noise characteristics

[25, 49, 282-283]. Graphene structure whose electronic properties are strongly dependent on surface adsorbates, which can change local charge carrier concentrations resulting in either p-type or n-type doping. One remarkable property of graphene sheets (one monolayer thick) is that every atom is a surface atom that participates in carrier transport. Therefore, even a single vapor adsorption event leads to a change in conductivity that can be easily measured [192-193]. This property explains the detection of single molecules in the gas phase [49]. Several graphene allotropes have been successfully used as gas/vapor sensors, including exfoliated graphene flakes, chemical vapor deposition (CVD) graphene, epitaxial graphene, and chemically reduced graphene (rGO). They demonstrate high sensitivity to NO_2, O_2, NH_3, H_2, CO_2, SO_2 and H_2S, even at part-per-billion and higher concentrations [50, 237-249, 284]. In spite of the high sensitivity, the usage of graphene for practical sensor applications remains a challenge. According to previous studies [194-195, 280, 285-287], chemical modifications of graphene through surface functionalization are not only capable of changing the electronic properties of the material, but can also affect the binding energy of molecules on the surface. Thus, functionalizing the graphene with appropriate metal oxide nanoparticles (NPs) that allow the precise binding of the target gas/vapor (e.g., sulfide containing analytes) to the graphene surface will be beneficial.

In this paper, we presents two types of chemical vapor sensors made of pristine graphene and ZnO metal oxide nanoparticle functionalized graphene grown via sublimation at high temperatures. It is well known that zinc oxide NPs are among the most studied nanomaterials for chemical sensing because they are thermally and chemically stable, less toxic, highly conductive, low cost, and come in a variety of shapes and sizes

[71-72]. Zinc oxide is an n-type semiconductor with a wide band gap energy of 3.37 eV. Previous studies have demonstrated that ZnO NPs on their own, as well as when they are combined with graphene, have a high sensitivity to gases/vapor such as methane, nitrogen dioxide, hydrogen, ammonia, ethanol, and acetone [70, 211-212]. Maximizing sensor sensitivity is of paramount importance, and in this work, we explore the relationship among device geometries for pristine and ZnO functionalized graphene. For comparison purposes, all devices studied had the same graphene mesa area, but with diverse defects patterns such as etched holes inside the graphene. These hole patterns included arrays of coarse and fine long slots etched perpendicular and parallel to the applied field, and two-dimensional (2D) arrays of squares, circles, and few and many pointed stars. An analysis of the hydrocarbon chemical compounds (decane $C_{10}H_{22}$, and propyl benzene C_9H_{12}) and sulfur containing chemical compounds (thiophene C_4H_4S, and octanethiol $C_8H_{18}S$) detection characteristics of the device has been performed at room temperature, and ZnO functionalized graphene was found to be the most sensitive sensor for the detection of sulfur compared to pristine graphene. Additionally, pristine and ZnO functionalized graphene sensors did not show any significant response toward decane and propyl benzene vapor.

6.2 Materials and Methods

6.2.1 Instruments and Experimental Setup

The devices were contacted by using a pair of Au-coated W probes from a conventional probe station connected to a computer-controlled SR830 DSP lock-in amplifier (LIA). The probes are connected to a low impedance voltage source $V_s = 0\ V_{dc} + 0.1\ V_{ac,\,rms}$ with a frequency on the order of 2 kHz, a different frequency for each device,

with a suitable bias resistor R_b (0.1-10 kΩ) with the device impedance in parallel with the 10 MΩ input impedance of the lock-in amplifier, so the lock-in amplifier measures the voltage drop across the resistor at the reference frequency. Therefore, we measure small changes in ΔV in R_b that correspond to small changes in the differential conductance $(G-G_0)/G_0$ of multiple devices on the same substrate with high signal-to-noise ratios. We placed the substrates on a sample chuck and monitored the temperature with a thermocouple contacting the substrate. The mass flow controller (MFC) controlled each component's flow rate independently, determining the composition of the mixed vapor. We generated the vapor by bubbling a small stream of dry N_2 0-100 standard cubic centimeter per minute (sccm) through a glass frit immersed in 15-25 ml of analyte. As a precaution to reduce the possibility of liquid condensation in the solenoid valve that directs liquid vapor to the device under test (DUT), a constant 200 sccm flow of N_2 has been mixed with the outlet of the following device, which is considered to be saturated with liquid vapor. When directed to the DUT, it is mixed with another constant flow of 4.8 lpm to achieve a range of dilution between 0.02 and 2%.

Understanding that the composition of the vapor head space is not solely determined by the nominal composition of the liquid is crucial. As a first order, the composition of the vapor pressure *P* can be given by $\sum_i x_i P_{0,i}$, where $P_{0,i}$ is the temperature-dependent equilibrium vapor pressure of each component and x_i is the mole fraction of each component *i* in the mixture ($\sum_i x_i = 1$). Variations from Raoult's law [289] can occur either in the direction of a simplification, or in the opposite direction, depending on the nature and strength of the interactions between the molecules, and these deviations are especially

significant for dilute species. In addition, the volatile components of a liquid evaporate from it, which changes the composition of the liquid, and that change is reflected in the vapor's composition. Thus, the sensor data acquisition system will be equipped with a residual gas analyzer (RGA) with differential pumping in order to collect vapor at atmospheric pressure and monitor analyte and substrate temperatures simultaneously. The relationship between RGA counts and the partial pressure of the vapor can be determined by measuring the RGA response at the characteristic mass observed at the known dilution of pure compound vapor at a known temperature. Based on this information, determine the partial pressures of specific compounds in the dilute vapor head space over a mixture.

For sensing experiments, pristine graphene and ZnO nanoparticle functionalized graphene devices were exposed to the following hydrocarbons: decane and propyl benzene as well as sulfur compound mixtures: thiophene and octanethiol at room temperature. Exhaust flow was monitored by residual gas analyzer (RGA) to check the level of hydrocarbon compounds and sulfur containing chemical compounds. The device response is defined as

$$\text{Response} = \frac{|G - G_0|}{G_0} \tag{6.1}$$

where G_0 is the conductance prior of the device to exposure to the target vapor and G is the conductance after exposure to the target vapor molecules. The vapor experiments were conducted for 800 s (100 s setup time, five dosing cycles of 60 s on and off, and 100 s settle time). When vapor flow was turned off, the sensors had been allowed to recover in air at room temperature for 60 s. After each measurement, the chip was heated on a hot plate in

an air at 125 °C for five mins to allow the sensor to recover. Then, equilibrate the chip back to room temperature (25-30 °C) by exposing it to air for at least five to seven mins. The following steps were followed for data collection: a) establishing a baseline of 200 seconds, b) a pulse sequence, typically five pulses 60 seconds on, 60 seconds off, c) LIAs, substrate temperature, and bubbler temperature samples are taken simultaneously at ~4 Hz and d) monitoring vapor composition in parallel with the pulse sequence.

6.3 Results and Discussion

6.3.1 Vapor Sensing Properties

Hall mobility measurements, of the films indicated pristine graphene carriers to be p-type with an average carrier mobility μ of 1047 $cm^2/(V \cdot s)$, and sheet density N_s of 1.42 x 10^{12} cm^{-2}, and ZnO functionalized graphene to be n-type with an average carrier mobility μ of 1030 $cm^2/(V \cdot s)$, and sheet density N_s of 6.33 x 10^{11} cm^{-2}. All other electrical evaluations such as total resistance, contact resistance, sheet resistance, contact resistivity, transfer length method, and $1/f$ low frequency noise measurements were completed elsewhere [255]. The pristine graphene and ZnO nanoparticle functionalized graphene devices were exposed to decane (3.2 ppm and 32.3 ppm), propyl benzene (3.4 ppm and 8.4 ppm), thiophene (88 ppm to 460 ppm) and octanethiol (0.2 ppm to 2.7 ppm) at room temperature.

The responses of the pristine and ZnO functionalized graphene sensors as a function of the thiophene vapor concentrations in the range of 88 ppm to 460 ppm and octane thiol vapor concentrations in the range of 0.2 ppm to 2.7 ppm in N2 carrier gas at room temperature are represented in Figure 6.1 – Figure 6.4, respectively. The responses shown

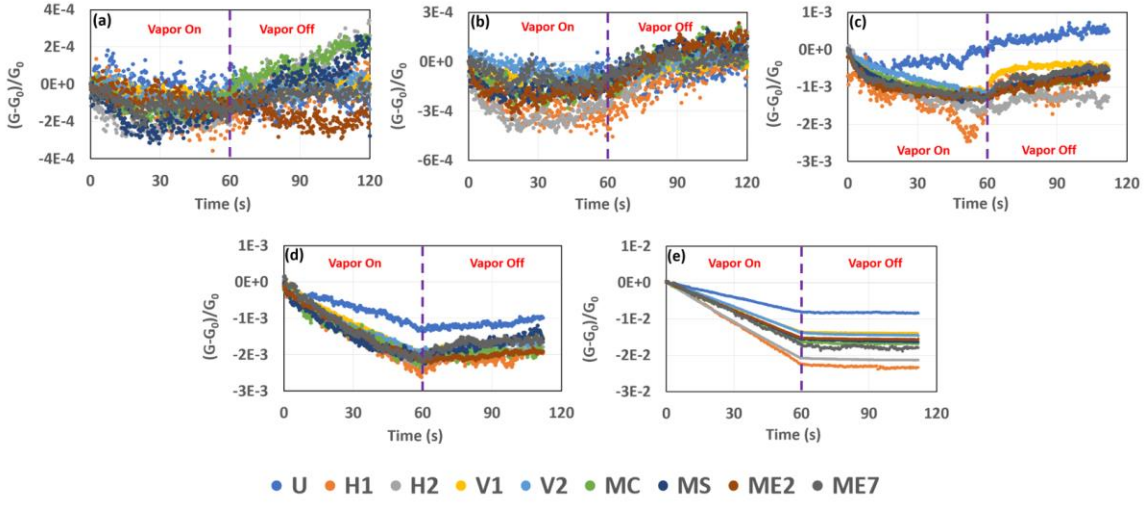

Figure 6.1: Conductance responses of pristine graphene for each device varying concentration of thiophene vapor (a) 88 ppm, (b) 97 ppm, (c) 270 ppm, (d) 340 ppm, and (e) 460 ppm at room temperature.

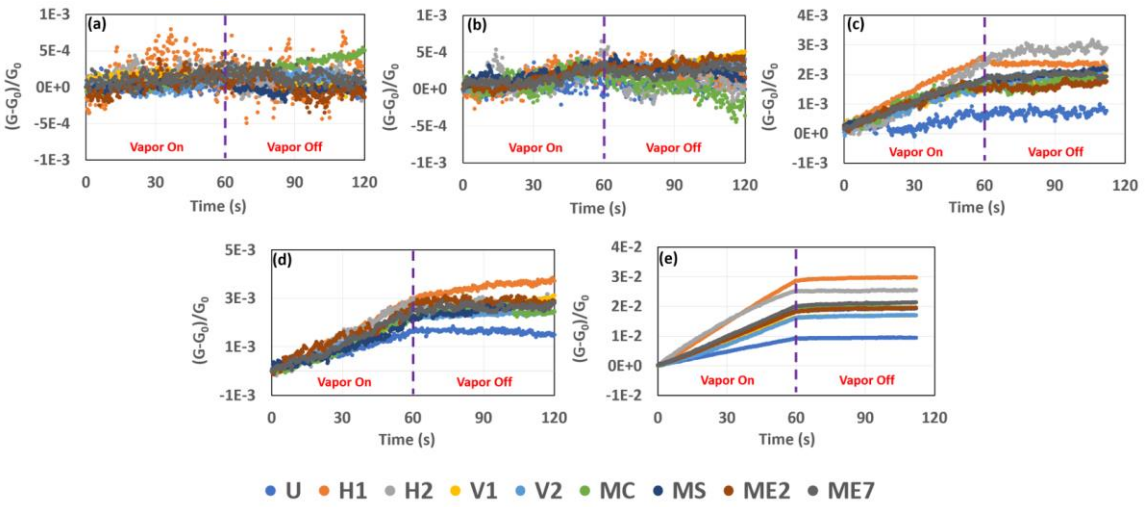

Figure 6.2: Conductance responses of ZnO functionalized graphene for each device varying concentration of thiophene vapor (a) 88 ppm, (b) 97 ppm, (c) 270 ppm, (d) 340 ppm, and (e) 460 ppm at room temperature.

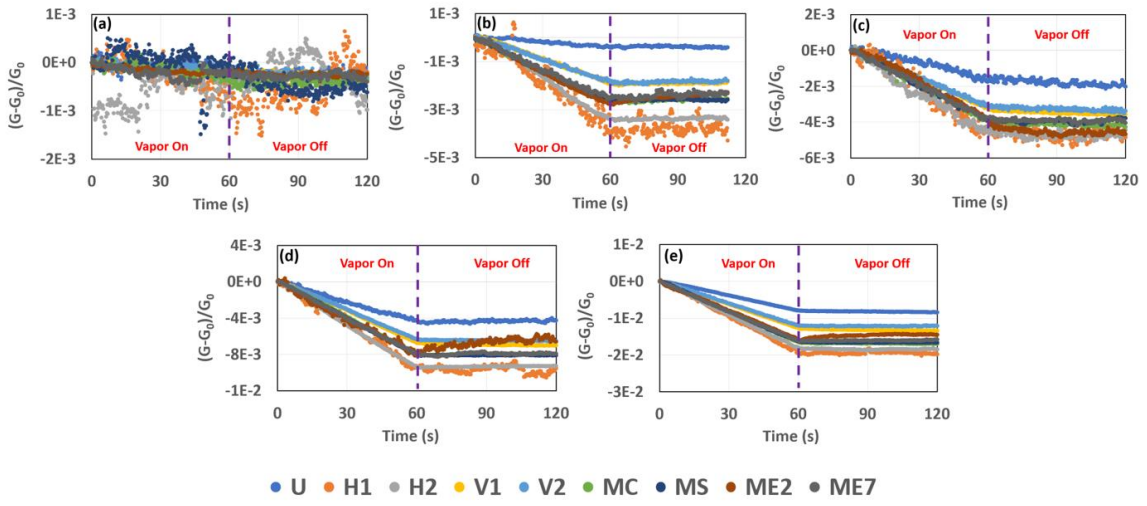

Figure 6.3: Conductance responses of pristine graphene for each device varying concentration of octane thiol vapor (a) 0.2 ppm, (b) 0.4 ppm, (c) 0.6 ppm, (d) 1.1 ppm, and (e) 2.7 ppm at room temperature.

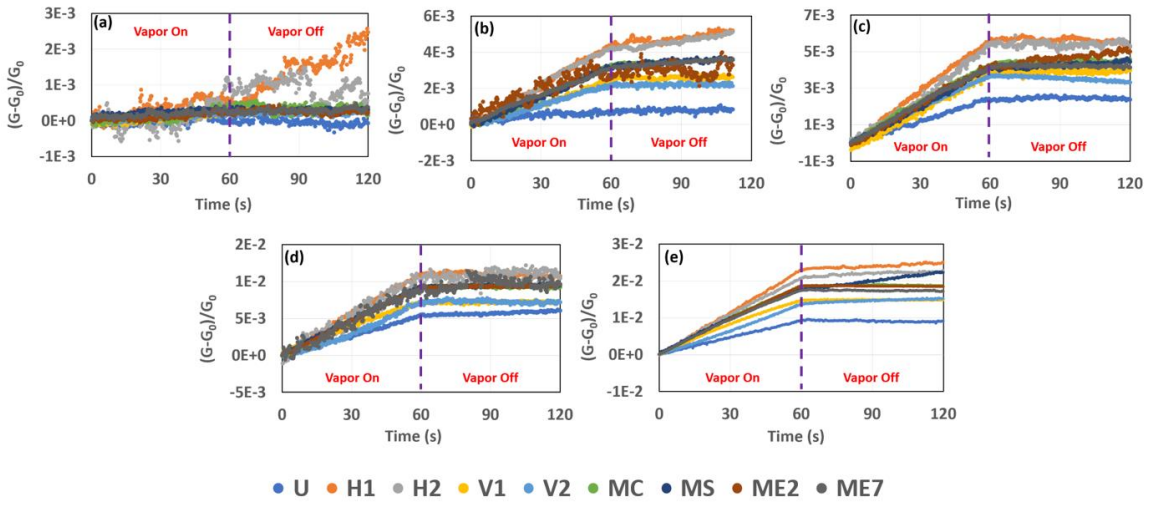

Figure 6.4: Conductance responses of ZnO functionalized graphene for each device varying concentration of octane thiol vapor (a) 0.2 ppm, (b) 0.4 ppm, (c) 0.6 ppm, (d) 1.1 ppm, and (e) 2.7 ppm at room temperature.

are average of the five 120 s response and recovery cycles for each device. As shown in Figure 6.1-6.4, a decrease in the pristine device conductance was observed when exposed thiophene and octane thiol vapor, while the ZnO functionalized device conductance increased upon exposure. This is likely attributable to the different majority carrier type in the graphene film, p-type for pristine graphene and n-type for ZnO functionalized graphene, and the nature of the labile charge in the adsorbates. Vapor sensing occurs when adsorption of species induces a change in film carrier population and consequently a change in conductance [290]. Adsorption of thiophene and octane thiol vapor onto graphene or zinc oxide evidently induces electron transfer from the adsorbate into the adsorbent. In the case of p-type pristine graphene, this reduces the carrier concentration in the graphene channel, shifting the Fermi level closer to the charge neutral point (Ns = 0), resulting in a decrease in the graphene conductivity. In contrast, the Fermi energy of n-type ZnO functionalized graphene is situated above the Dirac point. Exposure to thiophene and octane thiol vapors results in an increase in film conductivity. This can be explained as resulting from electron transfer into the ZnO particles followed by transfer from the particles along the linker molecule and into the film. These additional electrons move the Fermi energy further away from the Dirac point and thereby increase the device conductance.

As shown in Figure 6.1 to Figure 6.4, all the graphene sensor devices show an obvious response to thiophene and octane thiol vapor. The sensitivity of the pristine and ZnO functionalized graphene shows nearly linear dependence on the thiophene vapor concentration at the lower concentration region 88 ppm to 340 ppm and with the

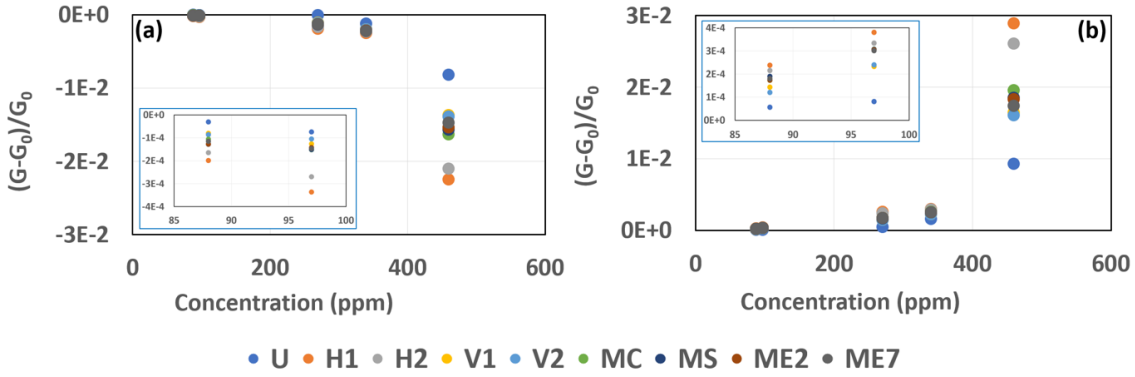

Figure 6.5: Sensor responses of the (a) pristine graphene and (b) ZnO functionalized graphene device for varying concentrations of thiophene vapor at room temperature.

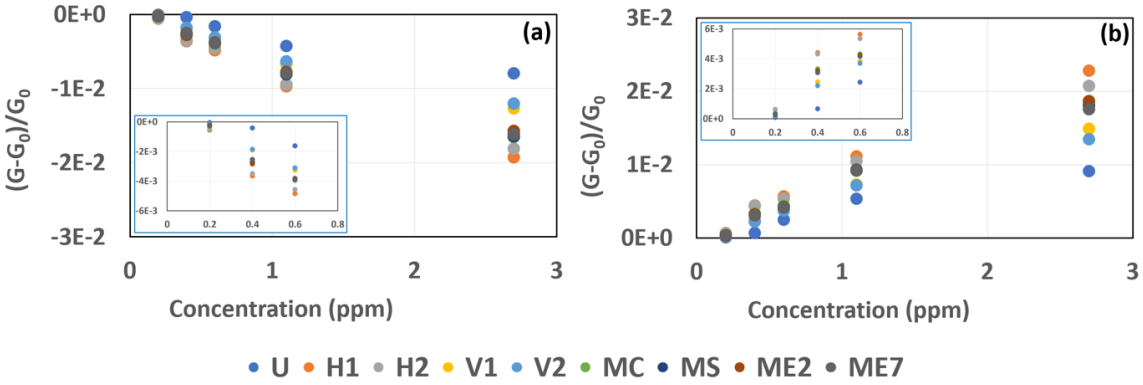

Figure 6.6: Sensor responses of the (a) pristine graphene and (b) ZnO functionalized graphene device for varying concentrations of octane thiol vapor at room temperature.

Table 6.1: Sensitivity of the pristine graphene and ZnO functionalized graphene vapor sensors for thiophene vapor and their detection limits.

Groups	Device Designation	Device Response, $(G-G_0)/G_0$									
		Pristine Graphene					ZnO Functionalized Graphene				
		88 ppm	97 ppm	270 ppm	340 ppm	460 ppm	88 ppm	97 ppm	270 ppm	340 ppm	460 ppm
A	U	-3.09E-05	-7.44E-05	-9.76E-05	-1.25E-03	-8.24E-03	5.65E-05	8.02E-05	4.53E-04	1.61E-03	9.27E-03
B	H_1	-1.99E-04	-3.36E-04	-1.91E-03	-2.51E-03	-2.25E-02	2.37E-04	3.80E-04	2.59E-03	2.95E-03	2.89E-02
	H_2	-1.66E-04	-2.70E-04	-1.68E-03	-2.34E-03	-2.10E-02	2.15E-04	3.33E-04	2.40E-03	2.86E-03	2.60E-02
	V_1	-8.09E-05	-1.27E-04	-1.13E-03	-2.01E-03	-1.37E-02	1.44E-04	2.32E-04	1.47E-03	2.24E-03	1.64E-02
	V_2	-8.70E-05	-1.05E-04	-1.20E-03	-1.98E-03	-1.39E-02	1.20E-04	2.39E-04	1.48E-03	2.23E-03	1.61E-02
C	MC	-1.06E-04	-1.52E-04	-1.29E-03	-2.20E-03	-1.63E-02	1.73E-04	3.08E-04	1.71E-03	2.54E-03	1.95E-02
	MS	-1.28E-04	-1.51E-04	-1.35E-03	-2.18E-03	-1.57E-02	1.89E-04	3.06E-04	1.65E-03	2.47E-03	1.85E-02
	ME_2	-1.28E-04	-1.43E-04	-1.31E-03	-2.22E-03	-1.54E-02	1.73E-04	3.05E-04	1.69E-03	2.48E-03	1.83E-02
	ME_7	-1.15E-04	-1.47E-04	-1.32E-03	-2.23E-03	-1.48E-02	1.80E-04	3.01E-04	1.70E-03	2.49E-03	1.74E-02

Table 6.2: Sensitivity of the pristine graphene and ZnO functionalized graphene vapor sensors for octane thiol vapor and their detection limits.

Groups	Device Designation	Device Response, $(G-G_0)/G_0$									
		Pristine Graphene					ZnO Functionalized Graphene				
		0.2 ppm	0.4 ppm	0.6 ppm	1.1 ppm	2.7 ppm	0.2 ppm	0.4 ppm	0.6 ppm	1.1 ppm	2.7 ppm
A	U	-6.35E-05	-4.11E-04	-1.62E-03	-4.32E-03	-7.96E-03	7.81E-05	6.63E-04	2.44E-03	5.35E-03	9.08E-03
B	H_1	-5.71E-04	-3.66E-03	-4.85E-03	-9.73E-03	-1.93E-02	6.22E-04	4.42E-03	5.63E-03	1.11E-02	2.28E-02
	H_2	-5.48E-04	-3.51E-03	-4.57E-03	-9.46E-03	-1.81E-02	6.09E-04	4.32E-03	5.35E-03	1.05E-02	2.07E-02
	V_1	-1.68E-04	-1.90E-03	-3.26E-03	-6.74E-03	-1.27E-02	2.17E-04	2.45E-03	3.82E-03	7.27E-03	1.48E-02
	V_2	-1.53E-04	-1.86E-03	-3.11E-03	-6.37E-03	-1.20E-02	1.93E-04	2.21E-03	3.70E-03	7.14E-03	1.35E-02
C	MC	-3.26E-04	-2.68E-03	-3.95E-03	-8.04E-03	-1.66E-02	3.65E-04	3.32E-03	4.32E-03	9.24E-03	1.86E-02
	MS	-2.47E-04	-2.73E-03	-3.81E-03	-8.10E-03	-1.64E-02	2.96E-04	3.19E-03	4.16E-03	9.29E-03	1.80E-02
	ME_2	-2.34E-04	-2.83E-03	-3.84E-03	-7.81E-03	-1.57E-02	2.55E-04	3.18E-03	4.24E-03	9.18E-03	1.86E-02
	ME_7	-2.50E-04	-2.55E-03	-3.88E-03	-7.99E-03	-1.62E-02	2.70E-04	3.08E-03	4.17E-03	9.13E-03	1.75E-02

octanethiol vapor concentration at the lower concentration region 0.2 ppm to 0.6 ppm, as shown in Figure 6.5, Figure 6.6, Table 6.1 and Table 6.2. These responses were averages of the five response and recovery cycles, then fit a line to the averaged response, and the interpolated value at 60s. We observed that the thiophene response profile could be modeled as a power law when concentration increases and the octane thiol profile, which

appears to be saturated, when concentration increases. It is found that the ZnO functionalized graphene devices exhibits the highest response among the pristine graphene devices for both thiophene and octane thiol vapor. This gain can be attributed to the more porous structure created by the NPs, which prevents the graphene sheets from re-stacking, and therefore increases the active surface area for vapor detection [232]. Another impressive feature is the significant improvement in device speed over pristine graphene. In general, group B (H_1, H_2) had the highest conductance value range, and group A (U) the lowest for pristine and ZnO functionalized graphene. The conductance values for the H_1 and H_2 device are a -1 to 1 order of magnitude greater than the other devices. Interestingly, based on Tables 6.1 and 6.2, a pattern was observed within the conductance value. The conductance values for Group B (H_1 and H_2) are the highest, followed by 2D (MC, MS, ME_2 and ME_7), which has the second biggest range of conductance values. The conductance values for group B (V_1 and V_2) are the third highest (similar values), while group A (U) exhibited the lowest conductance values. Based on these results, engineered defects onto graphene showed a marked improvement in sensitivity to thiophene and octane thiol vapors compares to unpatterned graphene. The sensitivity of graphene towards thiophene and octane thiol is related to a fast physisorption process occurring at room temperature [291-293]. The carbon sp^2-bonds in graphene's basal plane provide low-energy adsorption sites for thiophene and octane thiol through weak dispersive forces. In addition, structural defects, vacancies, and dangling bonds may allow higher binding energies, as they allow many hundred meV binding energies per molecule [232, 294]. These last

interactions may explain the slow kinetics of graphene's response to thiophene, and octane thiol observed mainly during the recovery phase in our experiment.

To further investigate the selectivity features, pristine and ZnO functionalized graphene devices were also exposed to decane (3.2 ppm and 32.3 ppm) and propyl benzene (3.4 ppm and 8.4 ppm). As can be seen in Figure 6.7, all the devices exhibited no response to decane and propyl benzene, while it produced a significant strong response to thiophene and octane thiol vapor. Based on these results, we are sensing sulfur molecules (S) rather than hydrocarbon molecules (C and H). These results are consistent with our density

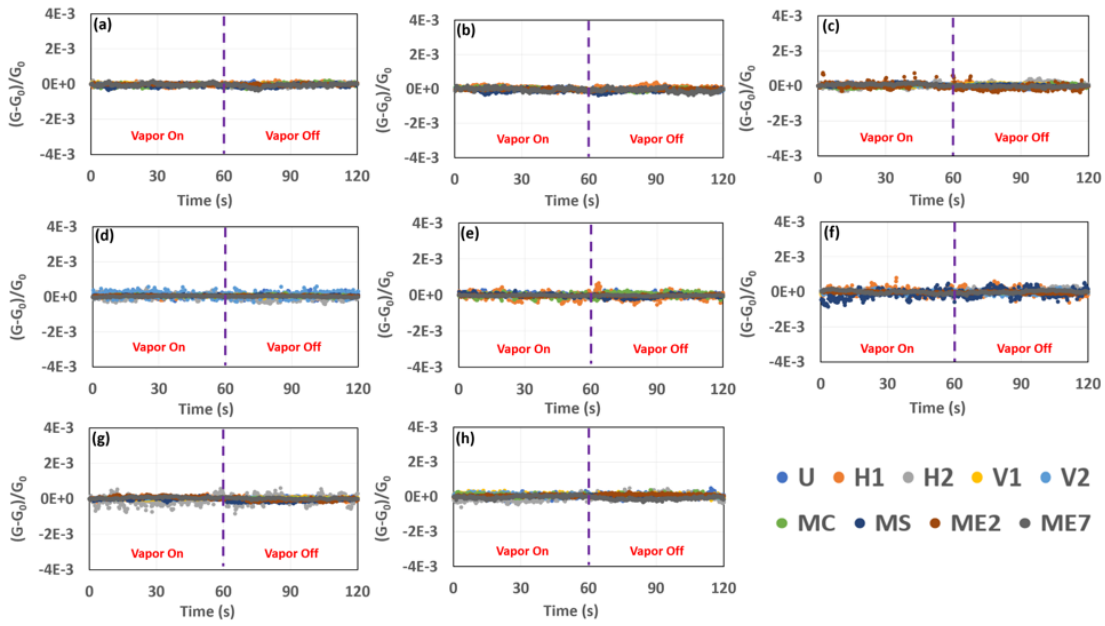

Figure 6.7: Sensor response of the pristine graphene devices was expose to decane at (a) 3.2 ppm, (b) 32.3 ppm and propyl benzene at (e) 3.4 ppm, (f) 8.4 ppm. Sensor response of the ZnO functionalized graphene devices was expose to decane at (c) 3.2 ppm, (d) 32.3 ppm and propyl benzene at (g) 3.4 ppm, (h) 8.4 ppm. These responses were average the five response and recovery cycles.

functional theory (DFT) simulation study in chapter 5. For the pristine graphene adsorption complexes, the decane, propyl benzene, thiophene, and octanethiol adsorption energies were calculated as 0.39 eV, 1.02 eV, -1.08 eV, and -3.62 eV, respectively. Additionally, the ZnO adsorption complexes, the decane, propyl benzene, thiophene, and octanethiol adsorption energies were calculated as 0.81 eV, 1.71 eV, -3.20 eV, and -5.76 eV, respectively. The results show that the ZnO nanocomposite surface provides the most energetically advantageous and stable adsorption of thiophene and octanethiol compared to pristine graphene, making it the most likely binding site for chemical molecules. This explains why ZnO functionalized graphene devices are faster in their response to thiophene and octanethiol and slower in their recovery processes.

The investigation of which device features influence conductance the most led us to study the relationship between conductance and device geometry, functionalization, effective graphene area, metal contact area, and mesa etched graphene perimeter. The area and perimeters (internal and external) of graphene mesas measured after etching and metal contact areas were calculated for the geometries shown in Figure 3.1 and described in Table 3.1. Based on our previous research [255], we discovered that functionalization generally lowers noise with the exception of the H_1, H_2, and U devices. Furthermore, these three products also have the lowest noise levels, implying that the factors contributing to noise, as well as the passivating effect of functionalization, are distinct for certain devices (H_1, H_2, and U), but not for others, specifically V_1, V_2, MC, MS, ME_2, and ME_7. According to our analysis of the device geometries, a single trap/excitation, generation/recombination, adsorption/desorption, etc., event can simultaneously induce significant changes in

mobility and carrier concentration in the H_1, H_2, and U devices, but not in the V_1, V_2, MC, MS, ME_2, and ME_7 devices, where much of the graphene is spatially remote from the primary transport paths. As a consequence, events outside of the direct paths between electrodes have a minimal impact on mobility through the defined regions, while the generated charges can easily diffuse into the areas of current flow where drift mobility (and, thus, scattering events) are important. The ME_2 is somewhat exceptional. Nevertheless, the sparser hole array compared to the MS and MC devices and reduced internal perimeter compared to the lower field, high carrier concentration area of the ME_7 device could explain the results observed. These results suggest that mobility and carrier concentration are rather complex relationships.

In an effort to look for correlations between measurable parameters of graphene area, contact area, active device perimeter, and conductance and, we present plots of these in Figure 6.8 (thiophene at 340 ppm) and Figure 6.9 (octane thiol at 1.1 ppm) for the two sets of devices, pristine and ZnO functionalized graphene. The graphene area and perimeter

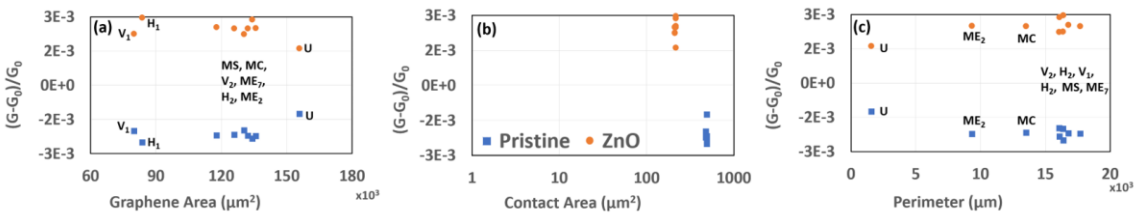

Figure 6.8: Conductance plotted against (a) graphene area, (b) contact area, and (c) total perimeter for both pristine and ZnO functionalized graphene devices expose to thiophene at 340 ppm.

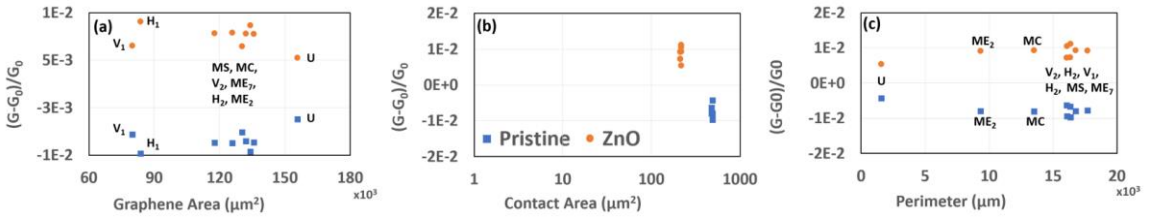

Figure 6.9: Conductance plotted against (a) graphene area, (b) contact area, and (c) total perimeter for both pristine and ZnO functionalized graphene devices expose to octane thiol at 1.1 ppm.

for each device was calculated from the mask data. The contact area was calculated from the width of metal contacts and the transfer length elsewhere [63]. There is no strong evidence for correlation with the device active (graphene) area or the contact area of the conductance. On the other hand, we do see strong correlation and inverse correlation between the perimeter and conductance. Based on this, it appears that different mechanisms exist in the device geometries in the various regions of the film that can be exploited to increase sensor performance, which can be used to improve sensor design. Ultimately, the question of which is the optimal sensor design is still unsettled. In this work, a characteristic and reproducible response behavior defined as change in conductance were achieved. In addition, the sensor should be designed in a manner that favors detection of perturbations induced by adsorption of target species over others. There should be a minimum tolerance for background or benign chemicals, which can also cause noise. Finally, nanoparticles other than 50–80 nm dia. ZnO may have different impacts on noise and sensor response. These factors will be explored in future work.

6.4. Conclusions

Researchers and developers have continued to encounter various challenges in developing chemical vapor sensor devices in terms of sensitivity, selectivity, reaction time, robustness, and other features. Graphene is one of the promising materials that has been used to address these problems in sensor applications. The goal of our work was to understand which graphene samples (with and without functionalization) is best suited for chemiresistive sulfur sensing applications. The goal of our work was to investigate the effects on vapor sensing on devices with engineering defects in graphene channels with and without functionalization. In this paper, by sublimation at high temperature in a chemical vapor deposition reactor, epitaxial graphene was formed on the Si-face of semi-insulating, on-axis 6H-SiC substrates. As a chemical linker, N-ethylamino-4-azidotetrafluorobenzoate (TFPA-NH2) was used to functionalized Zinc oxide NPs. For comparison purposes, all of the devices studied had the same graphene mesa area. As a result of analyzing the vapor sensing data for all sensors, ZnO functionalized graphene was found to be a highly efficient sensor for thiophene and octanethiol sensing. As a result of analyzing the vapor sensing data for all sensors, ZnO functionalized graphene was found to be a highly efficient sensor for thiophene and octanethiol sensing. As a results of analyzing the vapor sensing data for all devices, the conductance values for Group B (H_1 and H_2) are the highest, followed by 2D (MC, MS, ME_2 and ME_7), which has the second biggest range of conductance values. The conductance values for group B (V_1 and V_2) are the third highest (similar values), while group A (U) exhibited the lowest conductance values. The selectivity characteristics were also examined by exposing pristine and ZnO-

functionalized graphene devices to decane and propyl benzene. All the devices showed no response to decane and propyl benzene. The results indicate that we are sensing sulfur molecules (S) instead of hydrocarbon molecules (C and H). Furthermore, there is no strong evidence for correlation with the device active (graphene) area or the contact area of the conductance. On the other hand, we do see strong correlation and inverse correlation between the perimeter and conductance. According to experimental results, current and future researchers will benefit from this work, which will illuminate the analysis and selection appropriate device structure in pristine and ZnO functionalized graphene vapor sensors.

CHAPTER 7 : A CIRCUIT FOR GAS SENSING - DESIGN, TESTING, AND EVALUATION

7.1 Introduction

Detection of harmful gases and chemicals is very important in many fields such as environmental protection, industrial production and safety, agriculture, and medical diagnosis [242, 270, 295-297]. Gas and chemical sensors are used in critical applications to protect individuals from combustible, explosive, and toxic gases. Various materials [267, 269-270, 298-299], including inorganic semiconductors, metal oxides, solid electrolytes, and conducting polymers, have been used in fabricated sensing devices characterized by small size, low power consumption, high sensitivity, and long term reliability. Among these, nanomaterials such as carbon nanotubes (CNTs), metal-oxide nanoparticles, and graphene are be studied for use in chemical sensing for their excellent responsive characteristics, maturing preparation technology, and low cost of mass production for microelectronics applications since the traditional silicon-based technologies are reaching their limits [300].

In principle, a sensor is a device whose purpose is to detect some characteristic of its surroundings by a change in electrical or optical signal. Examples of commercial gas/chemical sensors include chemiresistors, silicon-based field effect transistors (FET), electrochemical, capacitance sensors (CS), and optical fiber sensors (OFS) [301]. Among them, chemiresistor and electrochemical sensors are the most commonly used in gas/vapor sensor detection applications due to their simple structure, easy implementation, and room-temperature operation [302-303]. Chemiresistor sensors consist of materials whose

resistance is modified as the result of charge transfer when a gas or chemical is adsorbed on the surface [302]. For electrochemical sensors, the target gas is either oxidized or reduced at the surface of the working electrode in the sensor. This reaction alters the potential of the working electrode relative to the reference electrode [303]. The schematic diagram of different types of gas sensor as shown in Figure 7.1.

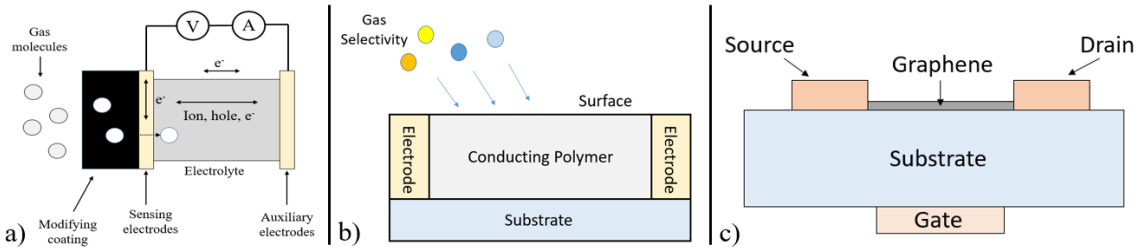

Figure 7.1: The schematic diagram of different types of gas sensors: a) electrochemical, b) chemiresistor, and c) graphene field effect transistor (FET) sensors.

The graphene Field Effect Transistor (GFET) sensor is composed of a graphene channel between two electrodes; the usual gate contact, isolated from the channel by a thin high quality oxide and which would modulate the electronic conductivity of the channel, is absent in the case of epitaxial graphene. Rather, the channel is exposed to the environment to enable functionalization and binding of receptor molecules to the channel surface. Materials that adsorb onto the channel affect conductivity through charge transfer, dipole scattering, and, in the case of electrochemical cell topologies with an aqueous saline ambient and a remote counter electrode, liquid displacement leading to a change in

equivalent gate capacitance. The ambient vapor effect on electrical signals in these sensors can be very low and possibly smaller than the noise level [304]. In some situations, the output of a sensor can be orders of magnitude smaller than the electrical noise level. Hence, precise measurements should be performed using appropriate high sensitivity instrumentation with high resolution. One solution is the use of lock-in amplifiers (LIA) [305-307] to identify data signals at a specific reference frequency using the phase detection method (PD). Since lock-in amplifier are phase sensitive, they measure both the amplitude of the signal and the phase difference between the reference and the input signal. In this work, a simple and portable analog LIA circuit, designed for gas sensing in any noisy environment, is presented. Building on the previous work, a wearable or portable lock-in multi-sensor platform suitable for any environment is designed.

7.2 General Architecture and Design: Components Identification

The commercial lock-in systems proposed in the literature [308-310], which are expensive, heavy, and power-hungry, are typically appropriate for multi-frequency operation and not considered suitable used in the portable sensing system that utilizes e.g., single supply battery cells. Therefore, results of this work can be used to design low-voltage and low-power embedded systems. Many inexpensive, compact, and lightweight solutions for sensor applications in noisy industrial environments have been reported [308-310]. Most of these analog sensor applications are designed for low frequency (i.e., 50 Hz - 1 MHz) phase-sensitive detection of conventional periodic signals (i.e., sinusoidal waveforms) with very long response times (i.e., 300s - 2000s) [311-313]. In order to

improve signal-to-noise (SNR) ratio in a chemielectric transduction device, in this work we need accurate amplification of a small signal in a somewhat noisy environment, with a wide frequency range of noise sources. Therefore, in this work we designed a portable analog lock-in amplifier circuit for gas sensing, subject to the design and performance specifications described here and derived from measurements and experience with functionalized graphene chemiresistors built in our laboratory. Specifically, we are designing a circuit to simultaneously excite and monitor conductance changes ΔG in a chemiresistive transducer of baseline conductance G_0 in response to vapor concentration changes ΔP. G_0 ranges between 5×10^{-4} and 1×10^{-3} Siemens, and $\Delta G/G_0$ ranges from 1×10^{-4} to 0.1. The 70 mV_{rms} excitation is between 1 and 3 kHz. Response times of interest will be as fast as 1 second, and as slow as 100 seconds. Other parameters of interest include response linearity (that is, output signal $\Delta V \propto \Delta P$) over three orders of magnitude, the noise floor of the system over the frequency range of interest, power consumption, and thermal drift of the electronics over the time scales of interest. Changes in conductivity can be measured effectively by forming a voltage divider, applying a known voltage to the series combination of the sensor and a bias resistor, and measuring the voltage drop across the bias resistor with a high impedance voltmeter. The conductance of the sensor is then easily calculated from the known applied voltage, the measured voltage, and the known bias resistor. Lock-in amplifiers function well as high input impedance, narrow-band ac voltmeters with very high noise rejection.

7.2.1 Low Noise Resistors

Electrical noise is an unwanted and unavoidable resistor phenomenon. The input resistor, used to reduce electrical loading on the device under test, is critical in any amplifier circuit. Resistor noise is often specified as microvolts noise per volt of applied voltage, for a 1 MHz bandwidth [314]. There are different types of noise components such as thermal or Johnson noise, shot noise and 1/*f* noise (flicker noise) [200].

In all materials, the electrons constantly move. As temperature increases, the movements increase. The vibrations of the electrons cause an electric signal (AC) across the terminals of the component. Because the vibrations are completely random, the electrical signal is noise. This is called thermal noise or Johnson noise. Thermal noise is the predominant source of noise for resistors and constant over a wide frequency range [200]. It is dependent on three variables: resistance, temperature, and measurement bandwidth. The relation between these three parameters is described by the formula:

$$E_{TH} = \sqrt{4 \cdot R \cdot k \cdot T \cdot \Delta B} \tag{7.1}$$

where E_{TH} is the RMS noise signal in volts, R is the resistance in ohms, k is Boltzmann's constant, T is the temperature in Kelvin and ΔB is the bandwidth in Hz. The equation shows that the noise level can be decreased by reducing the resistance, the temperature, or the bandwidth.

Shot noise is associated with a DC flow produced by carriers crossing a potential barrier and is attributed to the passage of discrete charge carriers. Carriers can cross the barrier provided they have sufficient kinetic energy to do so (some carriers cross, and some do not). The large numbers of carriers that do cross, each carrying a charge of magnitude

q, generates an average current I_{DC} [200]. On top of this is superimposed a minute fluctuation due to the randomness in the flow of individual charge carriers over the barrier. The root-mean-square value of the shot noise current I_n is given by the Schottky formula.

$$I_n = \sqrt{2 \cdot I_{DC} \cdot q \cdot \Delta B} \tag{7.2}$$

Where q is the charge of an electron, I_{DC} is the DC current, and ΔB is the bandwidth in hertz. Thermal and shot noises are also known as white noise because their spectral density does not depend on the frequency. The thermal noise increases with a larger resistance value, while the shot noise decreases.

A significant type of low frequency noise is flicker noise, also known as $1/f$ noise, that with thermal noise constitutes the two types of dominant noise in semiconductor devices [200]. Flicker noise is particularly important in analyzing the noise behavior of a device, as it typically dominates at low frequencies (less than 100 Hz). The corner frequency, f_0, where the $1/f$ noise level is equal to that of thermal or shot noise, ranges from a few Hz to tens of kHz.

Any noise at the input will be amplified by the full gain of the amplifier. Therefore, selecting a low noise resistor at the first stage is of great importance. Figure 7.2 shows the noise characteristics or index of several types of common resistors. The noise index (NI) in a resistor is commonly expressed in units of μV/V or in decibels, where u is root mean square noise voltage over a decade bandwidth, and U is the DC voltage drop across the resistor, by

$$NI_{dB} = 20 \log\left[\left(\frac{u}{U}\right) \cdot 10^6\right]. \tag{7.3}$$

Both *u* and *U* are measured in volts. The lower the noise index, the lower the level of noise in the resistor. As shown in the figure the carbon film, thick film and carbon composition resistors are not the proper choice for low noise applications. On the other hand, thin film, metal foil, and wire wound resistors have better noise characteristics and are thus often used for low noise applications [314]. However, wire wound resistors are not readily available in large resistance values and are usually inductive, which can cause instability problems in some cases.

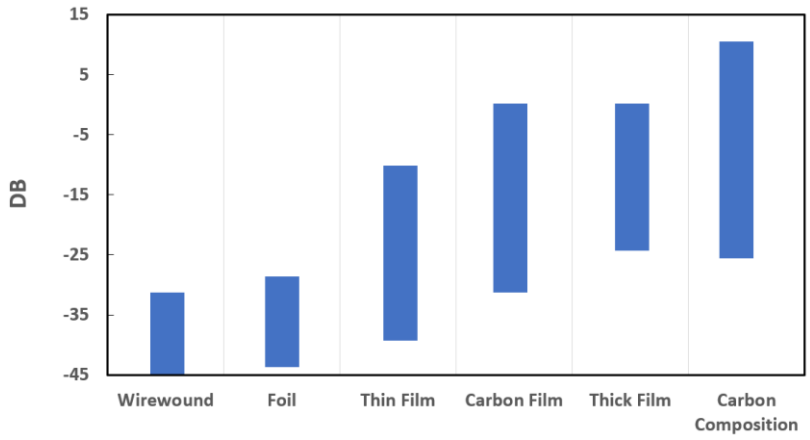

Figure 7.2: The Noise index (dB) of different types of commercial resistors [314].

7.2.2 Low Noise Capacitors

Film, rather than ceramic, capacitors are preferred for very low noise applications due to their lack of piezoelectric effects [315]. In addition, film capacitors such as polyester, polycarbonate and polypropylene have excellent temperature stability although

over a somewhat limited temperature range. Polyphenylene sulfide (PPS) capacitors operate over a broad temperature range, are stable, and can be acquired with large capacitance values above 1μF [315]. Any of these capacitors mentioned above will be suitable for our circuits.

7.2.3 Function Generator

A signal or function generator (oscillator) is a device that can produce voltage waveforms at a variety of frequencies, amplitudes, and sometimes shapes. A microelectronic implementation of a function generator can be constructed as an integrated circuit using several active elements [316-318], such as operational amplifiers and transistors. Most function generators can be used to generate sine, square, sawtooth, and triangular AC signals. These waveforms can be either repetitive or single shot (which requires an internal or external trigger shot). Function generators or oscillators are used in areas like communications, measurements, audio, and radio frequencies (RF), suitable for applications that need low distortion or stable frequency signals [319]. They are also used in the development, test, and repair of electronic equipment. Various type of operational amplifier ICs with different specifications are available commercially to meet performance requirements. One amplifier IC is inexpensive but drifts significantly with temperature. Another is low power, but also relatively noisy. Another operates as a high-speed amplifier, with high output current, and also high power. All operational amplifier selections are a compromise among performance, power, and price, and improving one specification means compromising on another.

7.2.4 Input Pre-Amplifier

The purpose of the input pre-amplifier is to accurately increase the size of a small input signal with a minimum of corruption from noise or input loading. Depending on the application and the characteristics of the input signal, different types of input amplifier ICs are used for lock-in amplifier applications. Operational amplifiers are widely used in lock-in amplifier circuits being employed as active elements in mixers, filters and also signal conditioning stages such as preamplifiers [320-322]. Beside low voltage and power efficient (class AB) operation, pre-amplifiers need to have a low noise, high input impedance and low input offset voltage. For example, one often uses instrumentation

Table 7.1: Different types of the IC input amplifiers with specifications [323-329].

Input Amplifier Performance										
Process	**Part Number**	**Architecture**	**Supply Voltage (Min/Max)**	**Gain (V/V)**	**Input Impedance (Ω)**	**Input Capacitance (F)**	**Noise (nV/√Hz) @ 1 kHz**	**-3dB Bandwidth (G = 1)**	**Input offset (Max Voltage)**	**Cost ($)**
Bipolar	AD620	Instrumentation	2.3/18	1 - 10000	10 G	2p	9	1 MHz	50 µV	5 - 48
Bipolar	TLE2141	Instrumentation	2/22	1	65 M	2.5p	10.5	5.9 MHz	200 µV	0.75 - 5
JFET	AD8220	Instrumentation	4.5/35	1 - 1000	10^4 G	6p	14	1.5 MHz	250 µV	3 - 10
N/A	AD8553	Instrumentation	1.8/5.5	0.1 - 10000	50 G	1p	30	1 K	120 µV	2 - 4
Bipolar	AD8675	Op Amp	5/18	126 dB	N/A	9.6p	2.8	N/A	75 µV	2 - 4
N/A	AD8429	Instrumentation	4/18	1 - 1000	1.5 G	3p	1	15 MHz	50 µV	5 - 13
Bipolar	OPA27	Op Amp	4/22	124 dB	2 G	2.5p	3.2	8 MHz	25 µV	1 - 4

amplifiers with high common mode rejection to make differential measurements that are not affected by noise on the ground lines [323]. Other studies also often used an IC TLE2141 low noise high speed precision operational amplifier [324], another study used a general purpose IC AD8220 instrumentation amplifier [325], and a zero drift IC AD8553 input amplifier [326], for lock-in amplifier circuit design. Table 7.1 shows specifications of some different types of commercially available operational amplifiers.

7.2.5 Phase Detector (PD) or Demodulator

Lock-in amplifiers are so-named because the amplifier is locked to, and the signal is thus measured at, a specific frequency of interest while ignoring input signals at all other frequencies. They are amplifiers because the output signal level is generally higher than the input signal level [330]. Since they are phase sensitive, they measure both the amplitude of the signal and the phase difference between the reference excitation and signal waveforms. Many studies using both analog and digital lock-in amplifiers for sensor applications such as thermoelectric, photoelectric, or electromechanical transducers have been reported [321-322, 331-332]. The use of digital signal processing techniques to perform the phase detector (PD) operations on the digitized signal is appropriate when the processing electronics include a processor with enough computing power to perform the mathematical operations required. However, the use of an analog lock-in amplifier is the best solution for portable sensor applications that include low-cost microcontrollers with limited computing power. These instruments enhance the detection sensitivity and resolution and improve the signal-to-noise ratio allowing measuring of small AC signal

amplitudes modulated at an operating frequency f_o by providing a proportional DC output voltage level.

Lock-in amplifiers use a phase detection technique to amplify the portion of a noisy and complex input signal at a specific reference frequency f_o, filtering out components at frequencies other than f_o. Although phase detection can be performed with analog or digital techniques, for wearable and portable sensors employing low cost microcontrollers with limited computing power, an analog lock-in amplifier is the best option [333-335]. The phase detector is used to improve the signal-to-noise ratio in AC signal measurements. It is a common signal processing element which is often used to demodulate an input signal by the reference signal. If two signals are multiplied, the result will be a signal consisting of the sum and difference of two signals as expressed in the following derivation.

$$\begin{aligned} A &= V_{in} \sin(\omega_1 t) \\ B &= V_{ref} \sin(\omega_2 t + \theta) \end{aligned} \tag{7.4}$$

where A and B are the signal and reference waveforms respectively, V_{in}, V_{ref}, ω_1 and ω_2 are the amplitude and angular frequency of signal and reference respectively, and θ is the phase difference between the two waveforms. The constant scaling factor, in units of 1/V, is not included in this derivation.

$$\begin{aligned} V_O &= A \cdot B \\ V_O &= V_{in} \sin(\omega_1 t) \cdot V_{ref} \sin(\omega_2 t + \theta) \\ V_O &= V_{in} \cdot V_{ref} [\cos(\omega_1 t - \omega_2 t + \theta)) - \cos(\omega_1 t + \omega_2 t + \theta))] \end{aligned} \tag{7.5}$$

where $\omega_1 = 2\pi f_1$, $\omega_2 = 2\pi f_2$

$$V_O = \frac{V_{in}V_{ref}}{2}[\cos(2\pi(f_1 - f_2)t - \theta) - \cos(2\pi(f_1 + f_2)t + \theta)] \tag{7.6}$$

$$\begin{aligned} V_O = \frac{V_{in}V_{ref}}{2}[&\cos(2\pi(f_1 - f_2)t)\cos\theta + \sin(2\pi(f_1 - f_2)t)\sin\theta \\ &- \cos(2\pi(f_1 + f_2)t)\cos\theta + \sin(2\pi(f_1 + f_2)t)\sin\theta] \end{aligned} \tag{7.7}$$

Application of a low pass filter to the output of the demodulator (see below, section 7.2.6) removes the last two terms; minimizing the phase between the reference and the signal eliminates the second and maximizes the first. If the signal and reference frequencies are equal, then $f_1 = f_2$

$$V_O = \frac{V_{in}V_{ref}}{2} \tag{7.8}$$

and this is proportional to the magnitude of the input signal and maximized by controlling the phase relationship between the input signal and reference [336-337].

There are many commercially available phase detector/demodulator IC chips with different specifications which can be selected according to project requirements. For example, one often uses a high precision balanced modulator/demodulator IC AD630 [338] that combines a flexible commutating architecture with accuracy. Other studies also often used an IC AD633-EP low cost analog multiplier [339], other studies have used a phase reversal analog switch MAX4526 [340] or a phase sensitive demodulator MPY634KP [341], for lock-in amplifier circuit design.

7.2.6 Low Pass Filter

Ideally, after low-pass filtering the output from the PD circuit is a voltage proportional to the phase angle between the input and synchronous reference waveforms multiplied by the input amplitudes. In actuality, the PD output after low pass filtering also includes contributions from (noise) signals with frequencies very close to the lock-in reference frequency, as allowed by the first term in eq. (7.6) [342]. Attenuation of these spurious signals depends upon the low pass filter cutoff frequency and the filter roll-off. A lower cutoff frequency will remove noise sources closer to the reference frequency and a higher cutoff frequency allows these signals to pass [343]. The low pass filter band edge f_{lp} determines the detection bandwidth $\Delta f = (f_0 + f_{lp}) - (f_0 - f_{lp}) = 2f_{lp}$. For example, setting the low pass filter cutoff to 3 Hz, appropriate for data sampling at 1 Hz, allows a 6 Hz bandwidth at the reference frequency.

A greater challenge is low frequency signals that effectively modulate the amplitude of the input signal. This possibly results in a low frequency AC output from the PD [344] that is ambiguous with, for example, changes in the quantity of that being measured by the sensor. Consider the effect of a low frequency signal, *e.g.*, a change in the sensor conductivity induced by a change in concentration of an analyte the sensor is designed to measure. While this change may in reality be an abrupt step function, we will here consider the Fourier decomposition of the signal into a set of sine waves modulating the conductivity of the sensor and thus the measured voltage signal across the bias resistor. Let one arbitrary component be described by

$$C = V_s \sin \omega_3 t \tag{7.9}$$

with ω_3 and V_s the frequency and amplitude of that component, respectively. Here we neglect phase differences. Then the measured voltage $V_{0,s}$ can be represented as the product of the reference signal and the analyte signal,

$$A \cdot C = V_{in} V_s \sin \omega_1 t \sin \omega_3 t \tag{7.10}$$

$$V_{0,s} = \frac{V_{in} V_s}{2} [\cos((\omega_1 - \omega_3)t) - \cos((\omega_1 + \omega_3)t)] \tag{7.11}$$

This signal is fed into the demodulator and compared to the reference also at ω_1. The output is a complex time- and phase- varying signal comprising frequencies $\omega_3 = 2\pi f_{lp}$ and lower that are then passed through the low pass filter. This defines the response time of the sensor measurement electronics.

A low pass filter can be implemented with passive elements, such as an RC-network, or R and C elements can be used together with one or more operational amplifiers to make an active filter. Multiple filter stages improve the sharpness (roll-off) of the low-pass frequency cut-off. Several filter designs exist, including Butterworth, Bessel, Chebyshev, and elliptic, with implementations in topologies such as the Sallen-Key. Factors relevant to filter design in this application include power consumption, size, roll-off, phase accuracy, and flexibility. Since low frequency noise is passed through the amplifier without attenuation, low frequency noise and component drift characteristics will be important design considerations.

7.3 Objective and Methods

The objective of this work is to design a wearable or portable analog lock-in amplifier circuit platform to improve SNR in a chemielectric transduction device for gas sensing. Typical sensor implementations reported in literature using lock-in amplifiers also used external function generators or oscillators, one or more amplifiers for gain control, one or two phase detectors or demodulators for phase detection, and a 2^{nd} - 4^{th} order low pass filter [308-310, 321-322, 335-341]. The lock in amplifier circuit proposed here includes an internal function generator, a high pass filter to remove DC offsets, a low noise pre-amplifier, a phase detector or demodulator (in phase, 0^{o}), and a 7^{th} order low pass filter for better noise reduction. Implementation details of each component or sub-circuit of the proposed lock-in amplifier circuit platform described in the section 7.4 in greater detail.

The software package known as PC Version of Simulation Program with Integrated Circuit Emphasis (PSPICE) [345] is a very powerful circuit simulation software tool that assists engineers in rapidly analyzing and designing multi-element circuits with analog and digital components. PSPICE can perform DC and AC analysis, transient analysis, Fourier analysis, noise analysis, parametric analysis, distortion analysis and Monte Carlo analysis, and can quantify circuit temperature sensitivity. Models of integrated circuits, with varying levels of accuracy and complexity, are freely available from manufacturers.

We have used the circuit simulation to design a wearable or portable lock-in amplifier-based sensor platform at the discrete component level. The design incorporates a $\pm$ 15V dual supply voltage and low noise commercial components (i.e., resistors,

capacitors, and integrated circuits). For comparison, the simulation is performed using either an ideal sine wave or the output of the function generator that we designed.

7.4 Proposed Circuit Design

A block diagram of our lock-in amplifier design is shown in Figure 7.3 and is intended to achieve phase-sensitive synchronous demodulation. As shown, it consists of six main blocks: function generator, sensor, high pass filter, low noise amplifier, phase detector (PD) or demodulator and low pass filter. The sensor is excited by a sinusoidal signal with a known frequency from the function generator and the output voltage of the sensor is injected into the lock-in system. The high pass filter has a very long time constant to remove any DC offset of the sensor signal with minimal impact on the sensor time response as fed into the low noise amplifier. The low noise amplifier provides high gain to the signal prior to it being sent to the PD. The PD or demodulator multiplies the amplified sensor signal with a sine wave reference signal. By properly synchronizing the input signal of the phase detector and the reference signals to have the same frequency and phase value, the data signal is full-wave rectified at the output. Then by using a low pass filter, high frequency (down to the cutoff frequency of the low pass filter, and excluding the effective bandwidth defined by the frequency difference equal to the low pass filter cutoff) noise is cancelled, and the absolute data signal mean value can be extracted. Hence, the combination of a demodulator and a low pass filter allows signals to be measured even when accompanied by significant noise.

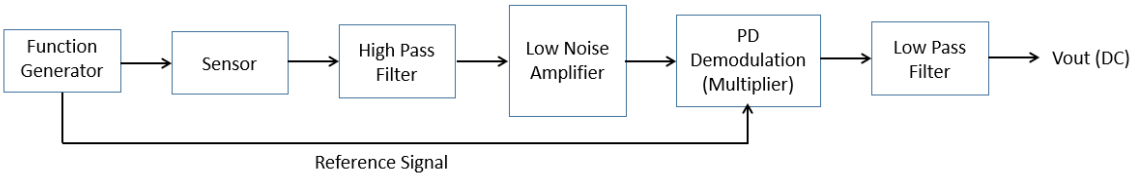

Figure 7.3: Block diagram of the proposed lock-in amplifier.

All four stages of the function generator circuit and all three active stages in the 7th order low pass filter circuit in the lock-in amplifier circuit design in this work used the OPA27 (Texas Instruments) integrated circuit (IC) operational amplifier. It was selected because it has ultra-low noise (4.5 nV/√Hz max at 1 kHz), high precision, low voltage offset drift (0.4 µV/º C) and low input offset error (100 µV max) characteristics [329]. A more recent device, the OPA4227, provides an updated model (the OPA227) and is available in a quad package. This would reduce circuit size and might be expected to increase circuit stability, as all the amplifiers would share a common substrate. This will be the subject of future investigations. We have used the OPA27 in this design simulation because PSPICE library models for the OPA227 and OPA4227 were not available.

An Analog Devices standard IC AD620 amplifier is used in the low noise input amplifier because it is a high precision instrumentation amplifier requiring only one external resistor to set gain from 1 to 10,000 (i.e., R_{gain} values to ground of open, 5.6 kΩ, 1 kΩ, and 50 Ω set gain values of 1x, 10x, 50x, and 10,000x, respectively). Furthermore, the AD620 has a low input offset voltage maximum of 50 µV and offset drift of 0.4 µV/º C [323]. Additionally, the AD620 works well as a preamplifier due to its low input voltage

noise maximum of 9 nV/√Hz at 1kHz and 0.1 pA/√Hz input current noise [323]. As shown in Table 7.1 in section 7.2.4., several more recent ICs such as the AD8428 or AD8429 can be used as suitable low noise input amplifiers but are not supported by available PSPICE models for the simulation.

This lock-in amplifier design uses the highly integrated and balanced AD630 modem chip, which not only simplifies the design relative to the options discussed above in section 7.2.5, but also effectively suppresses noise interference making it suitable for our LIA circuit design [346]. A more recent device, the ADA2200 synchronous demodulator is available but PSPICE does not support this device for simulation.

7.4.1 Function Generator

The function generator produces a variety of different waveforms (square, triangle, or sine) and allows for frequency adjustment using a potentiometer. The schematic for the function generator (that just uses operational amplifiers, resistors, and capacitors) is shown in Figure 7.4. Important performance requirements of this circuit include frequency stability vs. temperature and over time, minimal phase jitter, and sufficient current drive capabilities to maintain this performance while providing the sensor excitation voltage. The function generator shown in Figure 7.4 consists of two integrators and an inverting amplifier.

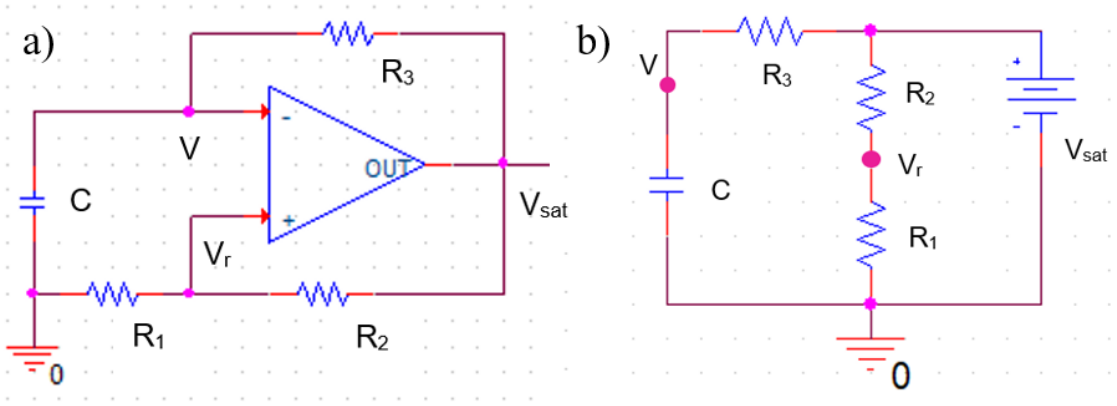

Figure 7.4: The astable multivibrator circuit (left) and a simplified version with the assumed ideal op-amp removed (right). The op-amp inputs, which have effectively infinite impedance, are at the nodes V and V_r. The op-amp output, which has effectively zero output impedance, is replaced by a voltage source V_{sat}. Finally, the op-amp gain is effectively infinite, so that V_{sat} switches between the negative and positive saturation values as determined by V_r - V.

The first stage is a simple operational amplifier square wave generator wired as a comparator and implemented as an astable multivibrator [347] as shown in Figure 7.4(a). To understand how it works, consider the circuit with the op-amp having immediately previously switched from driving the output to $-V_{sat}$ to driving the output to $+V_{sat}$. This leaves the voltage V at the inverting (-) input and the ungrounded terminal of the capacitor at the divided voltage V_r. This is shown in the simplified circuit of Figure 7.4(b), where the op-amp inputs of infinite input impedance have been removed from the circuit nodes at V (inverting input) and V_r (non-inverting input), and the op-amp output, which has a near-zero output impedance, has been replaced by a dc voltage source. The voltage V_r is a fraction β of the output voltage, $\pm V_{sat}$, $\beta = R_1/(R_1 + R_2)$.

The capacitor C charges through the resistor R_3, which limits the charging current I according to

$$I = \frac{V_{sat} - V}{R_3} = C\frac{dV}{dt} \tag{7.12}$$

Rearranging terms and integrating,

$$\int_{V_i}^{V_f} \frac{1}{V_{sat} - V} dV = \frac{1}{R_3 C} \int_{t_i}^{t_f} d\tau \tag{7.13}$$

$$-[\ln(V_{sat} - V)]\,|_{-V_r}^{V_r} = \frac{\triangle t}{R_3 C} \tag{7.14}$$

where the subscripts *i* and *f* indicate the initial and final capacitor voltages and charging points in time. Looking again at the original circuit, we see that the capacitor C starts charging when the output of the op-amp goes high, and once the voltage across the capacitor reaches the reference voltage V_r, the op-amp output saturates at the negative limit. Thus, $V_i = -V_r$ and $V_f = +V_r$. Completing the integration, substituting

$$V_r = \frac{R_1}{R_1 + R_2} V_{sat} = \beta V_{sat} \tag{7.15}$$

and dividing through by V_{sat},

$$-\ln\frac{V_{sat} - V_r}{V_{sat} + V_r} = \ln\frac{1+\beta}{1-\beta} \tag{7.16}$$

$$\triangle t = R_3 C \ln\frac{1+\beta}{1-\beta} \tag{7.17}$$

The capacitor now charges with reversed polarity and the output switches again to saturate at the positive limit once the capacitor reaches the reference voltage. This cycle continues, and the output is a square wave. If the positive and negative values of the amplifier saturation voltage have the same magnitude, then the positive and negative charging cycle times are the same and the expression for the period of oscillation follows. With the values used in the circuit here (in Figure 7.5), we find:

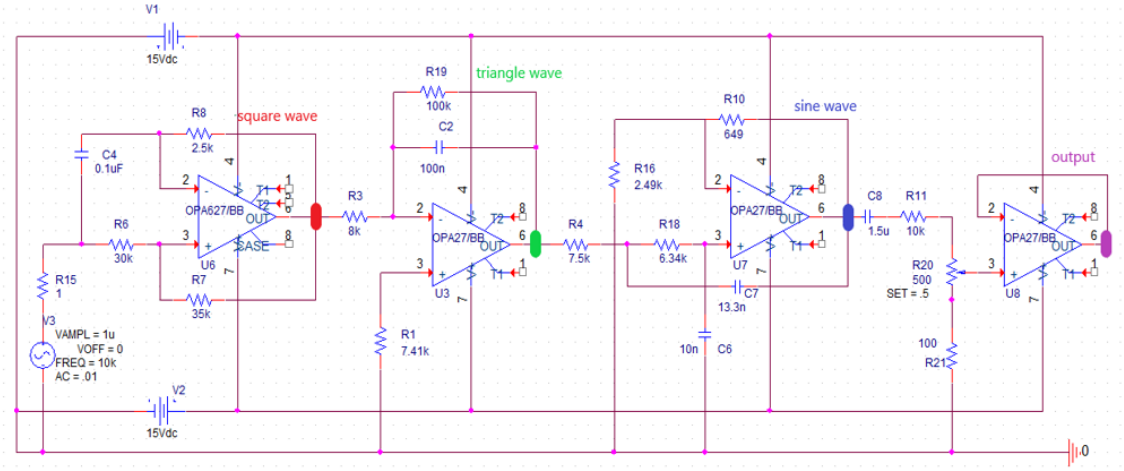

Figure 7.5: Schematic of the function generator sub-circuit. Stage 1 is an astable multivibrator, which generates a rail-to-rail square wave at 2 kHz (see text). Stage 2 is a low frequency integrator, converting the input square wave into a triangle wave. The triangle wave output from stage 2 goes to the PD to serve as a reference, and stage 3 filters the harmonic components of the triangle wave, leaving a sine wave at the fundamental frequency. Stage 4 removes any DC offset from the sine wave, sets the amplitude, buffers the output driving the sensor.

$$\beta = \frac{R_6}{R_7 + R_6} = \frac{30k\Omega}{30k\Omega + 35k\Omega} = 0.462 \tag{7.18}$$

$$T = 2R_8C_4 \ln\left(\frac{1+\beta}{1-\beta}\right) = 2(2500)(0.1 \text{ x } 10^{-6}) \ln(2.717) = 0.0005s \quad (7.19)$$

$$f = \frac{1}{T} = 2000Hz \; or \; 2kHz \quad (7.20)$$

where R is the resistance in Ω, C is the capacitance in F, β is the feedback fraction, T is the period in seconds, and *f* is the oscillation frequency in Hz.

As stated above, the frequency of oscillation for this circuit not only depends upon the RC time constant but also upon the feedback fraction. However, if $R_6 = 1.164R_7$, we see that *f* is equal to just 1 / 2RC. Therefore, the frequency of the output is given by $f = 1 / (2R_8C_4)$, 2 kHz for the chosen values of R_8 (2.5 kΩ) and C_4 (0.1 μF). The output $V_1(t)$ can be given by

$$V_1(t) = A \cdot \text{sgn}(2\pi ft) \quad (7.21)$$

although this is only accurate to within the bandwidth of the op-amp. The amplitude A is equal to the output rails of the selected op-amp. The optimal op-amp for stage 1 at U_6 will have characteristics of high slew rate and symmetric rail-to-rail operation, in addition to properties approaching the ideal op-amp: infinite input impedance (near-zero bias current), and zero output impedance (high drive current capability).

The output frequency, f_0, of 2 kHz is somewhat arbitrary since it depends on the impedance and capacitance of the sensor device we are measuring. It was chosen because we want to operate at as high a frequency as possible (to get away from 1/*f* noise) but are limited by the phase shift induced by the device characteristics (since the impedance is frequency dependent, $Z = 1/2\pi fC$, where C is the capacitance). We need to compromise on

the amplitude as well. If the amplitude is too low, the signal maybe lost in the noise. If the amplitude is too high, because the sensor devices are very small, they may experience non-linear effects from breakdown. Accordingly, 70 mV_{rms} seems like a good number to start with. The output of the function generator feeds into the sensor device and series bias resistor for amplification by the low noise amplifier and provides the reference signal for the phase detector or demodulator.

The second stage consists of an operational amplifier integrator. In normal operation of the op-amp, the inverting input will be maintained by circuit and the op-amp output at the same value as the non-inverting input, i.e., 0V. Otherwise, the high open-loop gain, and bandwidth of the amplifier rails the output. Assuming normal operation, the output of U_3, V_{out}, will draw a current through the capacitor that balances the current from the output of the previous stage, here V_{in}, through R_{in} (R_3):

$$\frac{V_{in}}{R_{in}} = -C\frac{dV_{out}}{dt} \tag{7.22}$$

Or, after rearranging terms and integrating, and letting Δt represent the time interval of interest (one half cycle)

$$V_{out}(t) = -\frac{V_{in}}{R_{in}C}\triangle t + \text{constant} \tag{7.23}$$

For our case, V_{in} is about ± 13V, and for f = 2kHz, Δt = 250 μs. Arbitrarily selecting a value of 0.1 μm for C_4, we should see a value of V_{out} = 4V by setting R_{in} = 8kΩ. The feedback resistor R_{19} provides a closed loop means of correcting for input bias voltage and current errors. A large value of 100 kΩ provides a low frequency closed loop gain of -12.5, and a

3 dB point at 100 Hz, but a very small parallel current path, assuring that the stable time response to a 2 kHz driving square wave is dominated by the capacitor. The integration constant will be handled at a later stage. The non-inverting input of U_3 is tied to ground using resistor R_1 (7.41 kΩ) in order to balance input bias currents. The output of the triangle wave generator will be used at the demodulator to minimize the phase between the excitation signal driving the sensor, and the demodulator input after multiple filter stages. The requirements on this amplifier are less severe than for stage 1, so we can select for good noise and power performance.

The third stage is a 2^{nd} order, single stage Butterworth low-pass filter design using a Sallen-Key topology, removing the harmonics in the triangle wave to leave a closer approximation to a sine wave. This circuit was designed using an online tool provided by Texas Instruments, Inc [348]. Design specifications used here included a passband frequency (2dB gain) of 2 kHz and a 40 dB attenuation at 20 kHz. This results in a sine wave amplitude comparable to the triangle wave, accounting for attenuation from the filtering of higher frequency components. Again, the requirements on this amplifier are less severe than for stage 1, so we can select for good noise and power performance. Anything less than a perfect sinusoid puts power into higher order frequencies, can generate signals ambiguous with noise at harmonic frequencies of the fundamental f_0, and cause inaccurate measurements of the sensor current at the drive frequency.

The final stage includes a passive high pass filter formed by the capacitor C_8 (1.5 μF) and resistor R_{11} (10 kΩ), potentiometer R_{20}, and resistor R_{21} in series in order to generate a 0.1V p-p signal from the previous sine wave while removing any DC

components. The passive filter has a 3 dB roll-off frequency of 1.6 Hz and largely eliminates DC offset errors. A simple follower to buffer the voltage-divided signal from changes in the sensor (load) impedance follows this passive stage. Outputs from the function generator feed into the sensor device and serve as the reference signal for the phase detector or demodulator.

7.4.2 Sensor, High Pass Filter (HPF), and Pre-Amplifier

The graphene sensor devices relevant to the circuit under discussion here have a real impedance between 5 - 50 kΩ, and a small and variable capacitance we are neglecting. This will be modeled in the simplest case as a 50 kΩ resistor, as shown in Figure 7.6. We will model real sensor responses as 10% changes in resistance with 0.5s rise and fall times and a 3s pulse width. We will later address sensor noise by modulating the sensor resistance

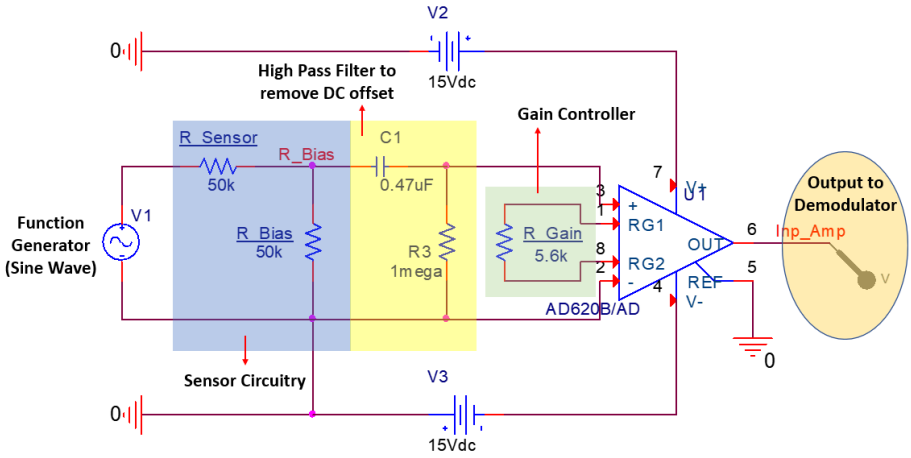

Figure 7.6: Schematic of the sensor circuitry, high pass filter, and low noise amplifier.

in a complex but more realistic fashion. The sensor is excited by a sinusoidal voltage signal from the function generator. The current through the sensor returns to ground through series resistor R_{bias}, generating a voltage. Matching the resistance of R_{bias} to the sensor is a good compromise between sensitivity and dynamic range. The capacitor C_1 (0.47 µF) and resistor R_3 (1 MΩ) form a passive high pass filter (yellow box; 3db roll-off at 0.34 Hz) to remove the DC offset of the signal fed into the low noise amplifier U_1. We will later examine the utility and cost of an active filter. The pre-amplifier U_1, here implemented with an instrumentation amplifier, amplifies the high pass filtered sensor output signal with the gain controlled by the resistor R_{gain}. The output of the pre-amplifier will feed into the phase detector (PD) / demodulator circuit.

7.4.3 Phase Detector (PD) or Demodulator

A PD is used in AC measurements to enhance the information content of a signal-plus-noise voltage by using a fixed frequency reference to demodulate a signal at that fixed frequency. This can be done by multiplying the input voltage by the reference signal resulting in an output signal consisting of the sum and difference of the input voltage and the reference. However, the internal behavior of the AD630, an integrated circuit implementation of a phase detection circuit, is not obvious on this point. For this reason, another interpretation of the AD630 modulator is developed. The diagram of the AD630 presented in the manufacturer's documentation in Figure 7.7(a) can be converted into the more useful version of Figure 7.7(b) [346]. In this figure, the individual A and B channel preamps, the switch, and the integrator output amplifier are combined in a single

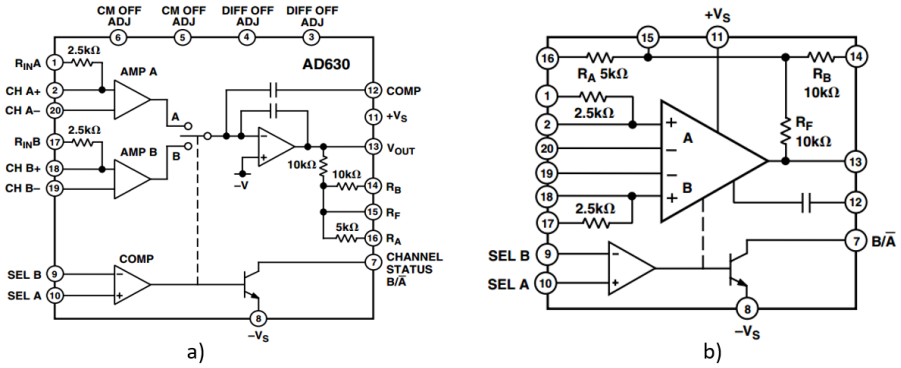

Figure 7.7: a) Main and b) simplified diagrams of AD630 from the manufacturer's datasheet [346].

operational amplifier. This amplifier has two differential input channels, only one of which is active at one time as selected by the comparator inputs, bottom left. It is not direct *multiplication* of reference and input signals connected to pin 1 and pin 17, but rather switching *between* input signals, or more precisely between amplified signals, that gives rise to the demodulation: the input signal, comprised of multiple frequencies, is only sampled at the reference frequency. Components of the input signal at the reference frequency appear at the output as DC values while components at other frequencies are time variant at the output. By using the triangle wave output from the function generator at input SEL A and comparing that to an adjustable value at SEL B, we can control the timing of the switch and so maximize the signal by controlling the phase.

The basic function of the AD630 may be easier to recognize as two separate gain amplifiers, which can be inserted into a signal path under the control of a sensitive voltage comparator. When the circuit is switched between amplifiers with inverting and

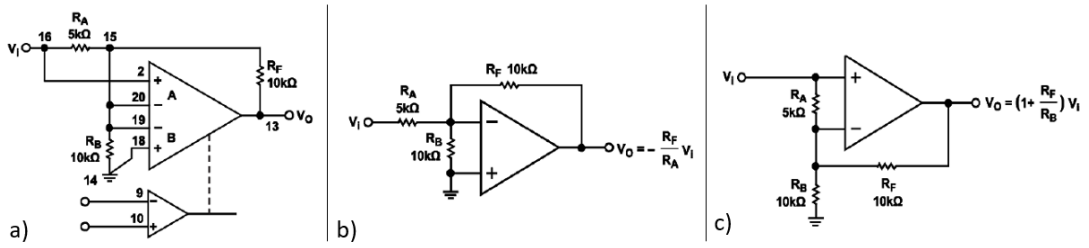

Figure 7.8: The schematics of a) AD630 symmetric gain (2), b) inverting gain configuration, and c) noninverting gain configuration [346].

noninverting gain, it provides the basic demodulation function [346]. Figure 7.8(a) shows an externally wired configuration (pin 16 to pin 2; pin 15 to pins 20 and 19; pin 18 to pin 14 and GND; input signal to pin 16; reference signal to pin 9; pin 10 to some constant value against which the reference signal can induce switching; pin 13, demodulator output) to illustrate the basic functionality of the AD630. The comparator selects either of the two input stages to complete an operational amplifier feedback connection around the AD630. When channel B is selected, the R_A and R_F resistors are connected for inverting feedback as shown in the inverting gain diagram in Figure 7.8(b). When the sign of the comparator input is reversed, channel B is deselected, and channel A is selected. Channel A is the noninverting gain configuration shown in Figure 7.8(c) [346].

In the configuration shown in Figure 7.9, pin 9 (inverting) of the voltage comparator is at ground and pin 10 (non-inverting) is connected to the reference signal. When the reference signal goes into its negative half cycle, Channel B is selected. This configuration provides inverting amplification with a gain of -2 whereas when the reference signal goes

into its positive half cycle, Channel A is selected, providing non-inverting amplification with a gain of +2.

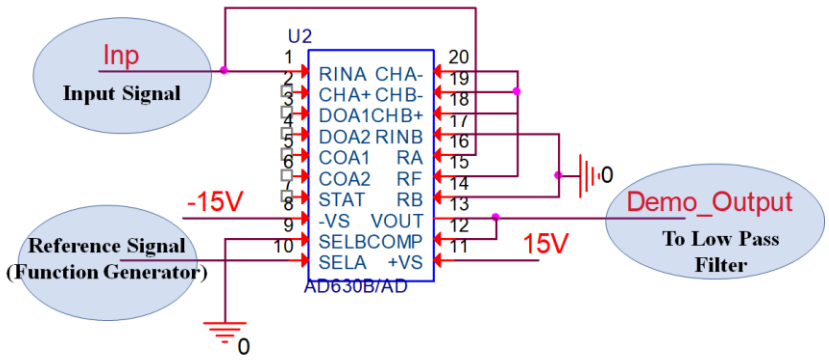

Figure 7.9: The schematic of the PD or Demodulator.

7.4.4 Low Pass Filter (LPF)

The last part of the circuit consists of the low pass filter, the output of which is a low frequency signal proportional to the amplitude of the voltage drop across R_{bias} at the reference frequency. Although it is not a DC signal (otherwise there would be no sensor response) it is a very low frequency. As mentioned in section 7.2.6, the purpose of the low pass filter is to remove the AC components from the desired quasi-static output. The quasi-static output V_{out} is described in the following expression:

$$V_{out} = A \cdot V_{Bias} \cdot \left| \frac{2\theta}{\pi} \right|$$
$$V_{Bias} = \frac{R_{Bias}}{R_{Bias} + R_{Sensor}} V_{in} \tag{7.24}$$

where $V_{in} = V_0 \sin(\omega t + \theta)$ is the excitation signal input to the sensor device, V_{Bias} is the signal input to the low noise amplifier, A is the circuit gain, R_{Sensor} is the sensor resistance, R_{Bias} is the bias resistor used to generate the voltage V_{Bias}, ω is the angular frequency and θ is the phase angle between the reference and input signals.

The proposed filter design is a unity gain 7th order low pass filter composed of a cascaded single passive 1st order stage and three identical active 2nd order stages implementing a Sallen-Key topology, shown in Figure 7.10. The Sallen-Key topology

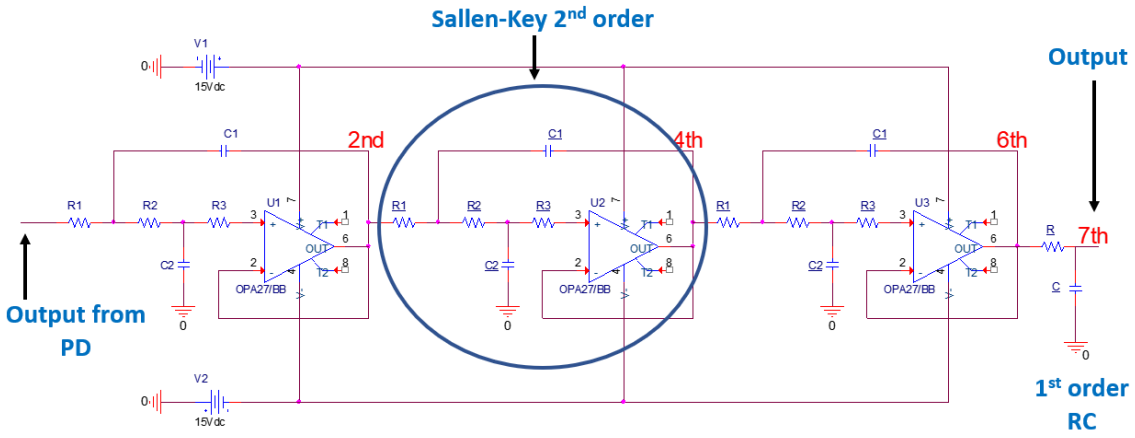

Figure 7.10: The schematic of the 7th order low pass filter and DC output.

[349] is an active filter design built around a single non-inverting operational amplifier, two resistors, and two capacitors, creating a voltage- controlled voltage-source (VCVS) design with filter characteristics of high input impedance, low output impedance, and excellent stability. The passive components, resistors R_2 and R_3 and capacitors C_1 and C_2 in Figure 7.10, form the 2nd order (blue circle) frequency selective circuit. At low frequencies, where C_1 and C_2 appear as open circuits and the amplifier input draws no current, the signal is simply unity-gain buffered to the output. At high frequencies, where C_1 and C_2 appear as short circuits, the signal is shunted to ground at the amplifier's input, the amplifier amplifies this input (~ 0V) to its output, and the signal does not appear at V_0. However, near the cut off frequency, where the impedances of C_1 and C_2 are on the same order as R_2 and R_3, positive feedback through C_1 provides a quality factor *Q* shaping of the filter frequency response [350]. In order to set filter components, the design procedure typically fixes the ratio between the resistors and between the capacitors. One possibility is to set the ratio between C_1 and C_2 as n^2 and the ratio between R_2 and R_3 as m^2. Therefore,

$$\begin{aligned} R_2 &= mR, \qquad R_3 = \frac{R}{m} \\ C_1 &= nC, \qquad C_2 = \frac{C}{m} \end{aligned} \tag{7.25}$$

As a result, the cut-off frequency, f_0 and quality factor, *Q*, expressions are reduced to

$$\begin{aligned} w_0 &= 2\pi f_0 = \frac{1}{RC} \\ Q &= \frac{mn}{m^2+1} \end{aligned} \tag{7.26}$$

Starting with an arbitrary choice for capacitor C and *n*, the appropriate value for resistor R and *m* can be calculated in favor of the desired f_0 and *Q*. Considerations of amplifier output

impedances of the active stage and any input stage, the non-zero values of stray and amplifier input capacitances, and available component sizes, also suggest optimal values for component resistance and capacitance.

As shown in Figure 7.10, the 2nd order filter can be cascaded with other RC (resistor and capacitor) stages to create a 3rd order filter. To create higher-order filters we can continue cascading. An individual stage of the Sallen-key filter can be cascaded to generate much higher order filters. It should be noted that the higher the filter order, the closer the filter becomes to the ideal "brick wall" response [350]. A Texas Instruments OPA27 IC operational amplifier, which provides low noise and a fast response, is used in the active low pass filter presented here.

7.5 Simulation Results and Discussion

7.5.1 Function Generator

Our function generator provides a 2 kHz 100 mV_{p-p} sinusoidal wave as shown in Figure 7.11(b). An OPA627 was found to provide better results in the multivibrator (1st stage) part of the circuit, presumably due to the significantly reduced input bias currents. In Figure 7.12 we compare the effect of the two different op-amps on the output amplitude. Specifications of the two op-amps, and the effect of each on the output, are shown in Table 7.2.

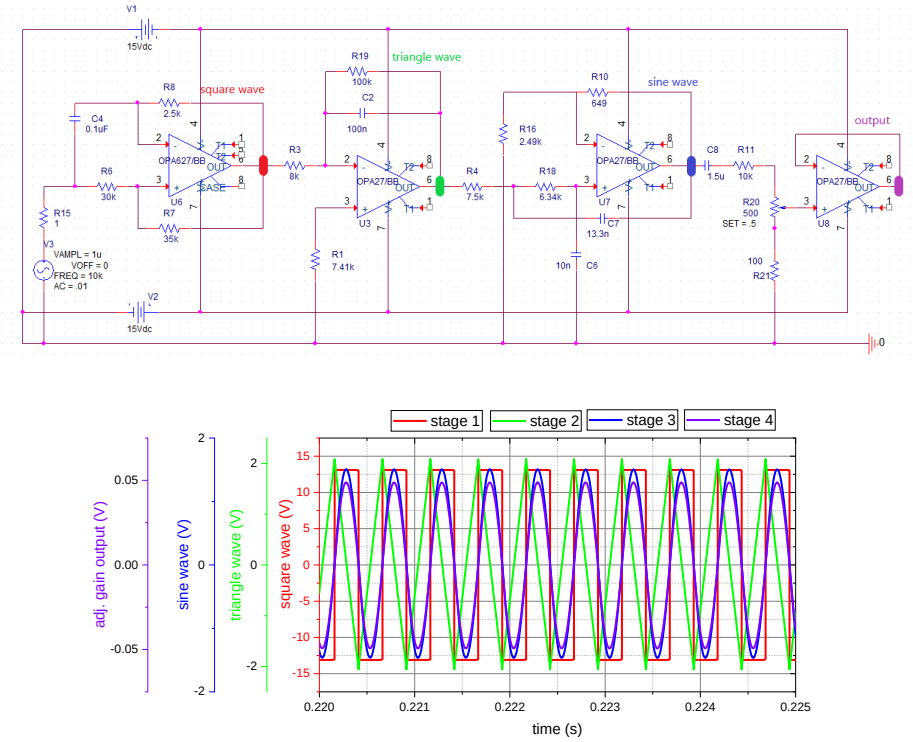

Figure 7.11: a) Schematic of the function generator circuit; b) function generator output provides 2 kHz sinusoidal signal with 100 $mV_{p\text{-}p}$.

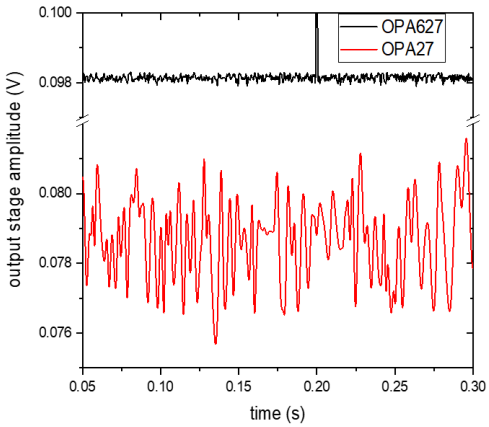

Figure 7.12: Comparison of function generator output amplitudes, fourth stage, for two different first stage op-amps, the low-noise OPA27 and the low noise, FET input OPA627. All other circuit elements are the same.

Table 7.2: comparison of two op-amps, selected parameters, and their effect on the output (stage 4) sine wave when used in stage 1 of the circuit in Figure 7.11, as extracted from the data in Figure 7.12.

	Input bias Current (pA)	Output Impedance (W)	Slew rate (V/μs)	Quiescent current, typ. (mA)	Inp. noise, 1 kHz, nV/√Hz	Mean out. from FG, V	Std. dev. from FG, mV
OPA27	±10000	70	2.8	2.8	3.2	0.079	1.145
OPA627	±1	55	55	7	5.2	0.098	0.172

7.5.2 Sensor, High Pass Filter (HPF), and Low Noise Amplifier

The 2 kHz, 100 mV_{p-p}, sinusoidal signal from the function generator (V_{IN}) excites the 50 kΩ sensor, R_{sensor}, and the matched 50 kΩ series resistor, R_{bias}, as shown in Figure 7.6. This representation of the sensor is generally adequate for simulations. However, as the circuit becomes more complex and the information needed grows, a more accurate representation of the sensor is needed. PSPICE includes a model of a voltage controlled admittance, which can be used to simulate a voltage controlled resistor. In use, the resistance between one terminal and ground multiplied by the voltage between a floating pair of terminals determines the resistance between a second floating terminal pair. PSPICE also includes a random number generator, which can be used to simulate a white noise source. We have used these two components to implement a model of a sensor of base resistance 50 kΩ, with the resistance modulated by a pulsed voltage and a parallel noisy voltage source as shown in Figure 7.13. The changing resistance of the sensor R_{sensor} as

controlled by these two sources causes the envelope of the 2 kHz signal V_{IN} measured across R_{bias} to change.

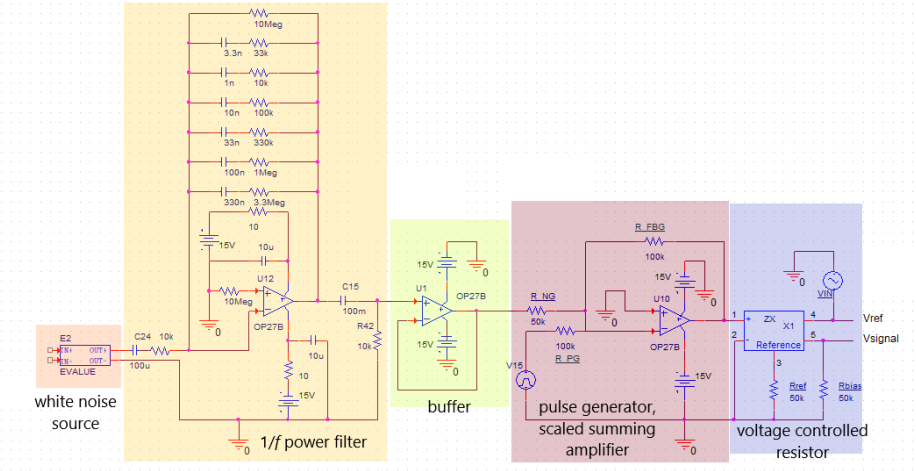

Figure 7.13: This circuit schematic shows the combination of a white noise source, an active filter with voltage gain roll-off of $f^{-1/2}$ over the range of 50 mHz to 50 kHz, a passive high-pass filter to roll off the signal below 1 mHz, a buffering amplifier for the filter output, an amplifier to scale and combine the buffered $1/f$ noise source and the pulsed voltage source, and a voltage controlled resistance. A simple 2 kHz sinusoidal source V_{IN} and the series bias resistor R_{bias} are also shown. The output $V_{signal} = V_{ref}*R_{sensor}/(R_{sensor} + R_{bias})$, is connected to the next stage high pass filter. Other than R_{bias} and the circuit represented by V_{IN}, none of this circuit would be actually built: it is intended only to simulate a responsive and typically noisy sensor with resistance determined by the modulation of R_{ref}.

The pulsed voltage source has been programmed to source a voltage pulsed between two values V_0 and V_1, with a controlled rise time t_R, fall time t_F, and pulse width PW. The random number generator functions as a sequential value voltage source. The component returns a pseudo-random number evenly distributed ("white noise") between 0 and 1 at each time increment of the simulation. This value can be offset and scaled as

needed. By filtering the source as shown in Figure 7.13, we can approximate a 1/*f* power spectrum over the range of the filter [351]. In this case, the filter was designed to create a pink noise spectrum, that is,

$$V = A / f^{1/2} \tag{7.27}$$

over the range 50 mHz to 50 kHz. The effect of this filter on the original white noise spectrum is shown in Figure 7.14. After buffering, this signal can be scaled and summed with the pulsed voltage source to simulate a noisy sensor. Of course, it is not intended to build this circuit; rather, it is a means of simulating a chemiresistor with 1/*f* noise.

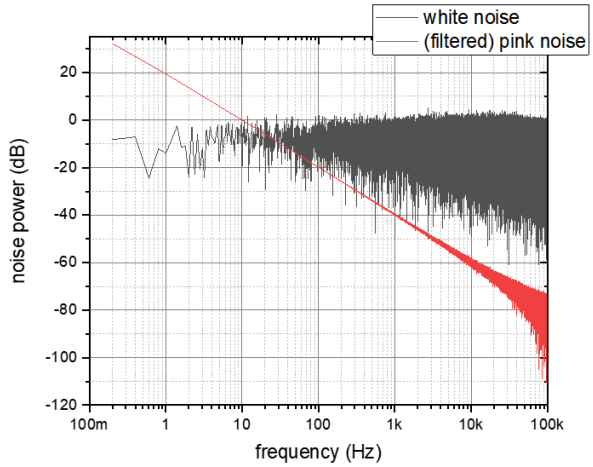

Figure 7.14: Frequency spectrum of pseudo-white noise source (-), and noise after filtering by the circuit shown in Figure 14(-). The white noise intensity spectrum is flat, the pink noise (flicker, or 1/*f*, noise) spectrum is very nearly linear over six decades of frequency. The data shown was collected over a 5s simulation.

The voltages at various point of this circuit, as well as their spectral decomposition, from a 100s simulation with time steps limited to 10 μs are shown in Figure 7.15. At the

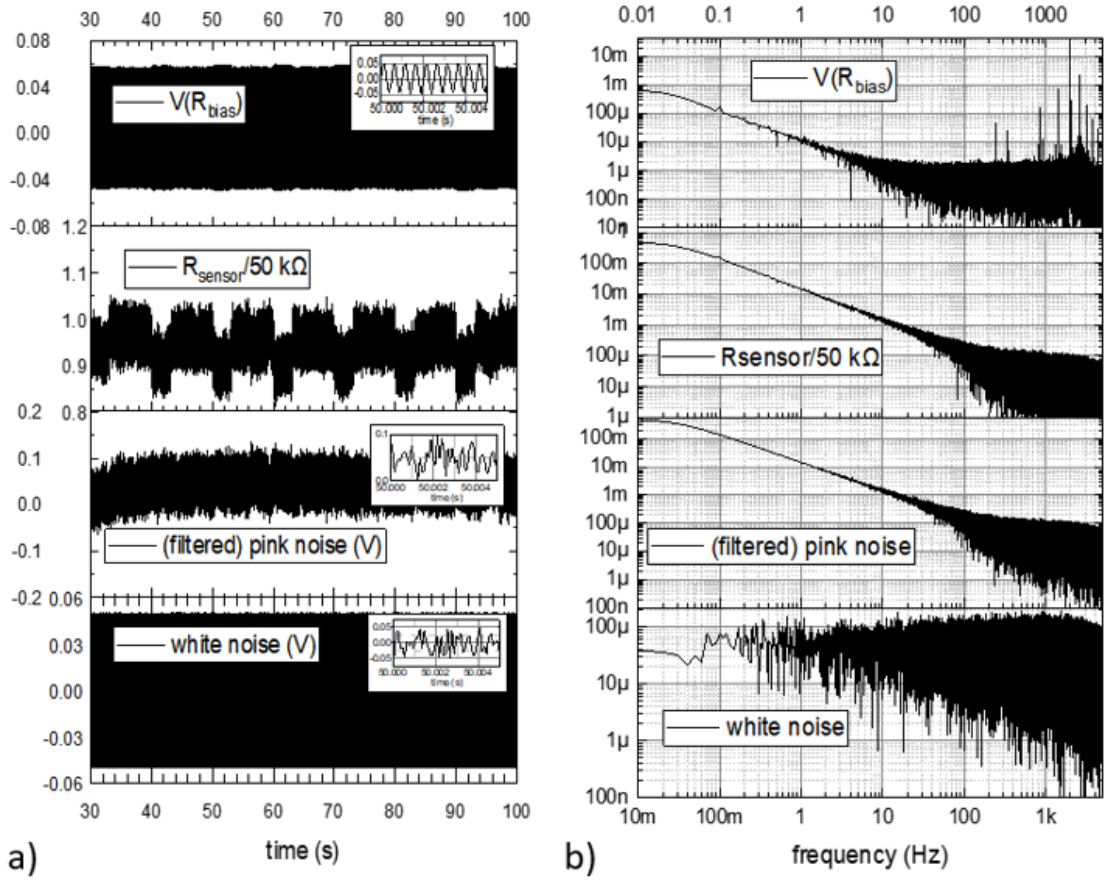

Figure 7.15: Shown here are signals associated with the sensor, a) in real time, and b) in a spectral decomposition derived from a fast Fourier Transform. Although the simulation began at 0s, it took almost 40s for the circuit capacitances to charge. At bottom is the output of the white noise generator, centered at 0.0V and scaled to ±0.05V. New values were generated every 10 μs. A time expansion of that signal is shown as an inset in a). Above that is the output of the pink noise filter, noticeably coarser. A time expansion of that signal over the same interval as the lower inset is also shown as an inset. Above that is the sensor resistance, scaled to the 50 kΩ reference value. Above that is the signal measured at the node between the simulated sensor and the series resistor R_{bias}, where the variable and noisy sensor resistance and R_{bias} create a voltage divider acting on the 2 kHz sinusoidal signal from the function generator. A time expansion of that signal is shown in the upper inset.

noise filter. Above that is the resistance of the simulated sensor, incorporating both the bottom is the output of the white noise source. Above is the signal after applying the pin pink noise and the pulsed voltage, here with 0.1s rise and fall times applied to 3s pulses between 100% and 95% on a 10s period. It has been normalized by the value of the 50 kΩ reference resistor. Finally, we show the voltage observed at the node between the sensor and the series resistor Rbias. These two resistors form a voltage divider applied to the 2 kHz, 100 mV sinusoid. Here, rather than use the signal from the function generator, we have used a simple sine wave generator in order to simplify the simulation.

In Figure 7.16, we see the voltage between the sensor and the bias resistor as fed into the capacitor C1 (0.47 μF) and resistor R3 (1 MΩ), which together form a passive high pass filter with a very long time constant (~ 0.5 seconds) that removes any DC offset. The

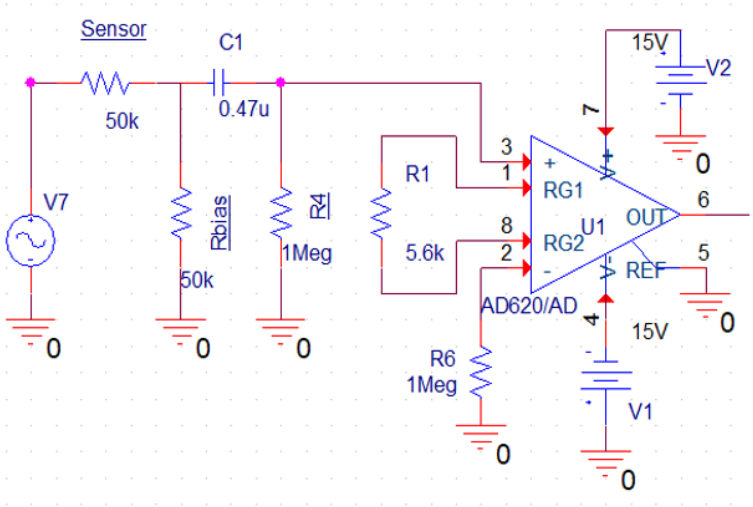

Figure 7.16: The schematic of the passive high-pass filter and low noise amplifier circuit, along with a fixed value sensor resistance.

low noise pre-amplifier U_1 receives the AC signals from the high pass filter and amplifies them. The gain of this amplifier depends on the value of the gain resistor R_1. For illustration, in this section we have set our low noise amplifier gain to be 10x. This setting is a compromise. If the gain is too high, the output signal is prone to drift due to noise, so that the output signal will soon reach saturation, but if the gain is too low, it will not be able to extract the desired signal.

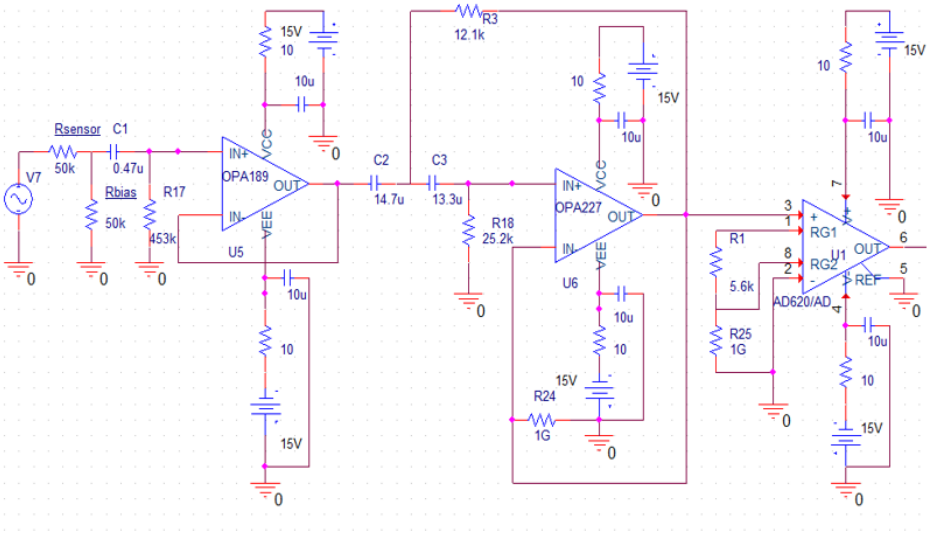

Figure 7.17: Implementation of an active 3rd order Bessel high-pass filter between R_{bias} and the preamplifier (U1), shown here with a single resistor representation of the sensor, R_{sensor}. Certain components have been added to this circuit, specifically 10 Ω resistors and 10 µF capacitors on all the power supply lines and 1 GΩ resistors between some nodes and ground, in order to increase circuit stability as implemented and during simulation.

As an alternative, we have explored the use of an active high pass filter with a steeper roll-off to address the problem of low frequency noise from the sensor. We have chosen to implement this as a two stage, 3rd order Bessel filter in order to maintain the proper shape of non-sinusoidal resistance changes. The active high pass filter circuit is shown in Figure 7.17. The power dissipation of these two additional op-amps is 150 mW, which is significantly higher than that of the preamplifier, 29 mW, and of the passive filter,

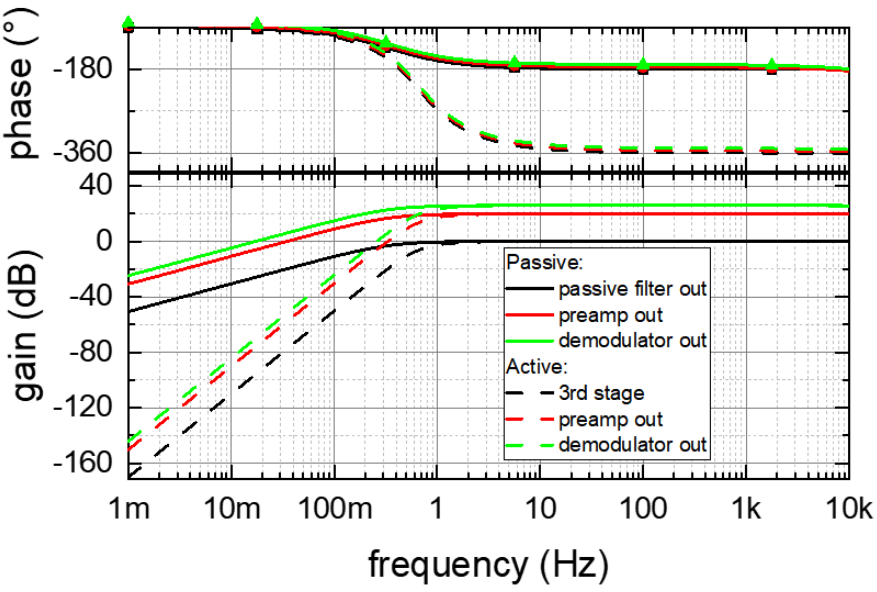

Figure 7.18: Transfer function of the high-pass filter and low noise amplifier, referred to a signal applied across R_{bias}.

about 2 nW. The output of this circuit is presented in Figure 7.18 as a Bode plot of gain and phase *vs* frequency using an ideal sine wave source for V_{ref} and sweeping the frequency. For both circuits, the gain at the demodulator output relative to the signal applied to the sensor is about 26 dB for all frequencies above 1 Hz, up to the roll-off of the AD620 at about 0.5 MHz (not shown).

7.5.3 Phase Detector (PD) or Demodulator

The PD is used to improve the signal-to-noise ratio in alternating current signal measurements. The PD multiplies the input signal by a synchronous reference signal. This configuration, with a voltage-controlled resistor circuit and passive high pass filter, is shown in Figure 7.19. The 2 kHz, 100 mV_{p-p} excitation signal as measured at R_{14} (R_{bias}),

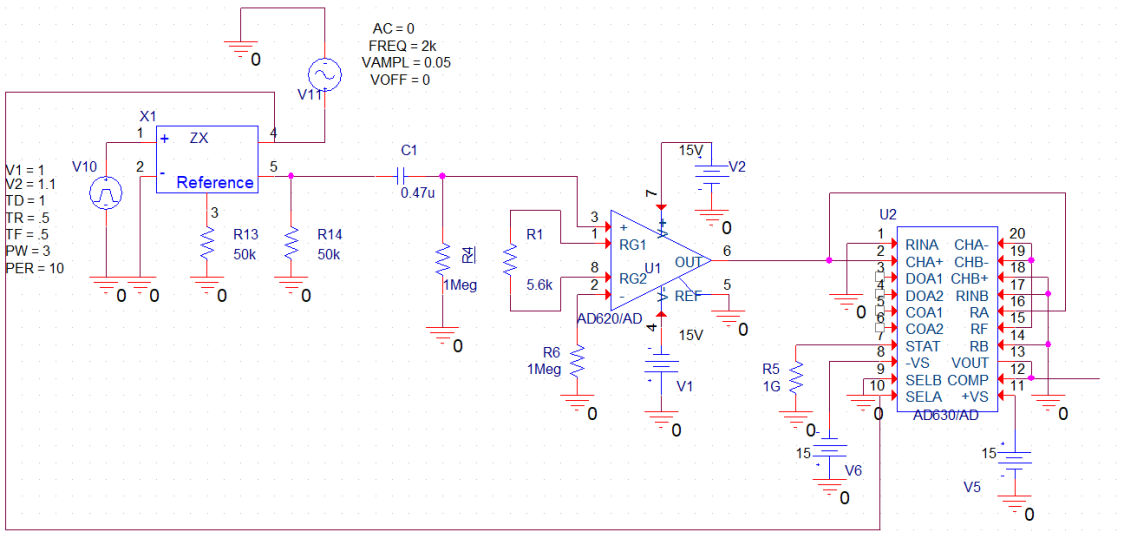

Figure 7.19: The schematic of the pulsed-resistance sensor, passive high pass filter, low noise amplifier, and demodulator.

the output of the pre-amplifier, and the fully rectified output of the demodulator are shown in Figure 7.20(a). For comparison, we show the maximum envelope for the two circuit configurations of passive and active high pass filters at the node between the sensor and R_{bias}, as output from the pre-amplifier, and as output from the demodulator, in Figure 7.20(b). The sensor resistance is modulated so as to represent a 5% increase in resistance in a 3s pulse with a 0.5s rise and fall time. Switching between inverting and noninverting inputs of the AD630 is under the direct control of the reference signal. During the positive half cycle of the reference signal, AD630 acts as a noninverting amplifier with a gain of 2, and during the negative half cycle, it acts as an inverting amplifier with a gain of -2. There is a certain amount of noise evident in the output from the demodulator, attributable in this case to input offset current errors propagating to the output of the low-noise amplifier. These are partially ameliorated by resistor R_6 (Figure 7.16), matching the impedance to ground at the non-inverting input. Figure 7.20(c) shows the demodulated signal after passing through AD630, appearing as a positive rectified signal. Figure 7.20(d) shows a spectral decomposition of the demodulator output signal from the active filter circuit configuration.

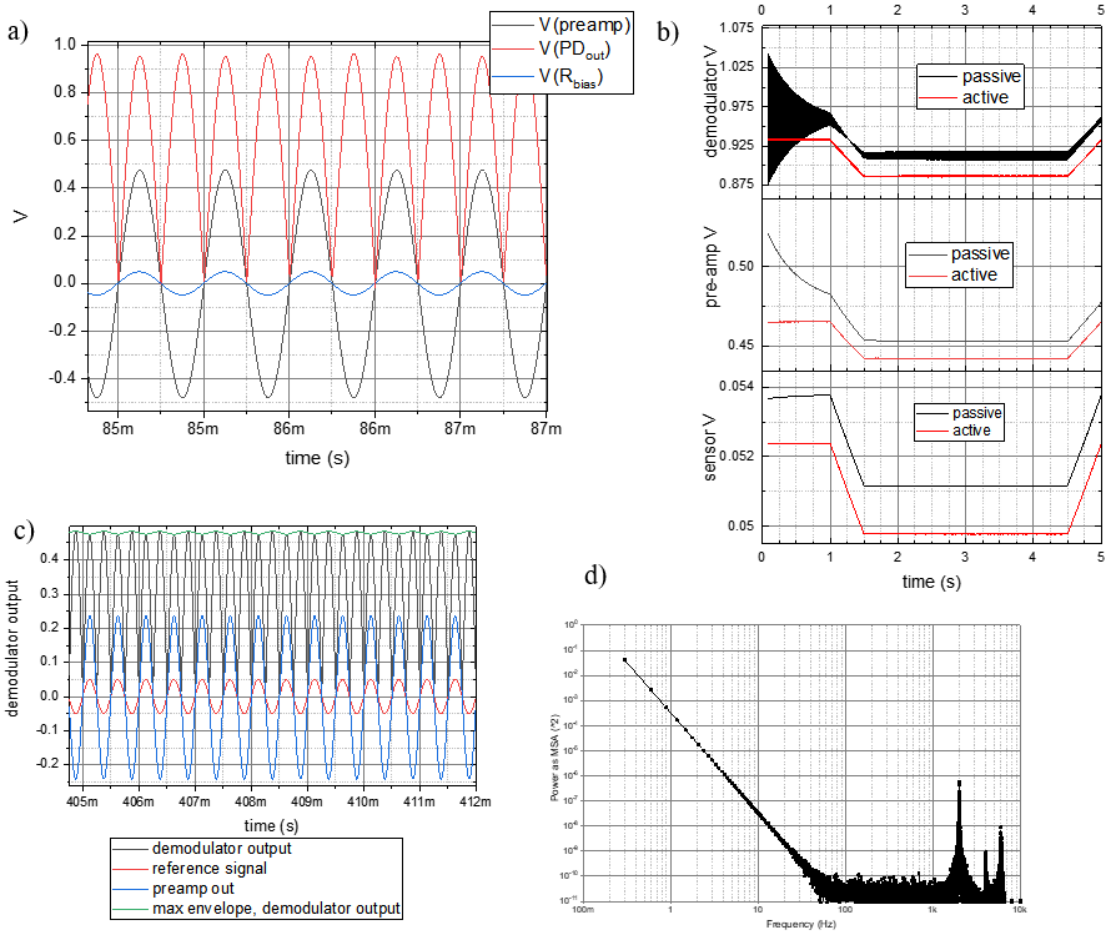

Figure 7.20: a) shows the 2 kHz signal at the node between the sensor and R_{bias} (-), the output from the low noise preamplifier (-), and the full wave rectified output from the demodulator PD (-) as simulated in the circuit shown in Figure 20. b) shows the peak envelope maximum at the output of the sensor (bottom), preamplifier (middle), and demodulator while the sensor resistance changes from 50 kΩ to 55 kΩ for 3 s, for the passive (-) and active (-) high pass filter circuits of Figure 7.19 and Figure 7.17, respectively. c) shows the demodulator output at higher time resolution, along with the other signals. The "maximum envelope" plotted in figure b) is also shown. d) shows the results of a fast Fourier transform plotted as power versus frequency in the demodulator output data shown in c). The next stage low pass filter easily blocks the components at 2, 4, and 6 kHz.

7.5.4 Low Pass Filter (LPF) and Output

The purpose of the low pass filter (shown in Figure 7.21(a)) is to remove noise in general, and in particular any frequency components related to the 2 kHz reference frequency from the desired quasi-static output (see section 7.4.4 or eq. 7.24). For this reason, its cutoff frequency should be as low as possible [349]. The cutoff frequency f_c of

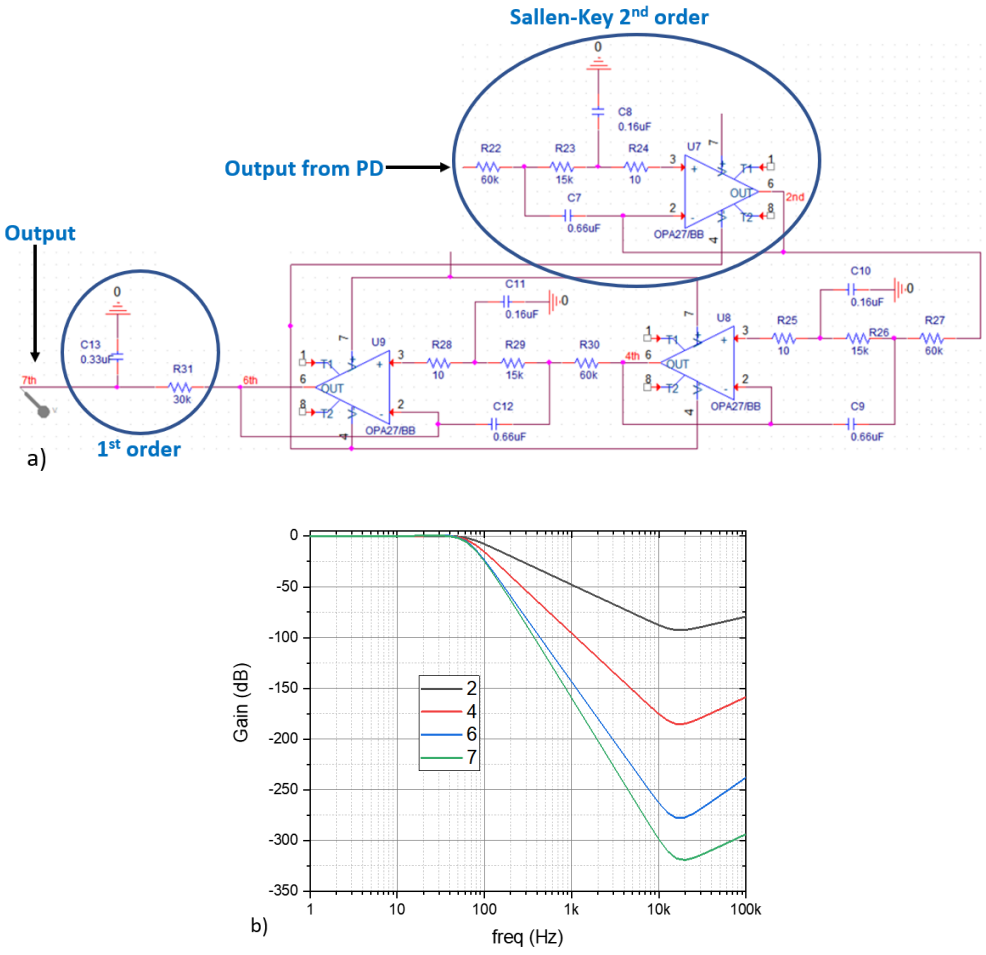

Figure 7.21: a) Schematic of 7th order LPF. b) Transfer function after the various stages of the filter shown above.

this circuit is about 16 Hz, well below the LIA input signal frequency f_i = 2 kHz. To achieve this, using the equations 7.25 and 7.26 to select values for this Sallen-Key filter, the reference resistor R and the capacitor C have been set to 30 kΩ and 0.33 μF, respectively. Thus, the resistors R_1 and R_2, and the capacitors C_1 and C_2, have been calculated and set to 60 kΩ, 15 kΩ, 0.66 μF and 0.16 μF, respectively. The simulated voltage output after various stages of the 7th order LPF is shown in Figure 7.21(b).

In Figure 7.22, we show the utility of the entire circuit, incorporating the pulsed, noisy resistor in the simulation. In order to show something like a representative pulse in response to a set of sensing events, we have generated 4 successive pulses of 5% change in conductivity, 3s long, on a 10s period. A flicker noise source has been added to induce changes in the resistance with a 1/*f* power spectrum. Although the 5% change in device conductivity is arguably visible, it would be difficult to determine a quantitative response given the noise without significant computational analysis. The signal measured at the node between the simulated sensor and the 50 kΩ bias resistor, as excited by the 2 kHz sinusoid from the function generator is also shown. Finally, we show the output from the circuit superimposed on the desired information, sensor conductivity. We show conductivity here in order to maintain the direct relationship between the input and output signals. The rejection of high frequency noise in the sensor conductivity has been visibly effective (see Figure 7.23), although low frequency noise persists. This is very difficult to remove here without removing information from the signal. For this reason, we ultimately apply signal averaging, exploiting the fact in the practical sensor that we have control over the airflow over the sensor by, for example, operation of a valve cycling between a control source of

clean air and our air under test. By inducing a periodic sensor response, we can average over multiple cycles and thus reinforce signal information at the expense of random noise fluctuations. The effect of this is shown in Figure 7.23(b).

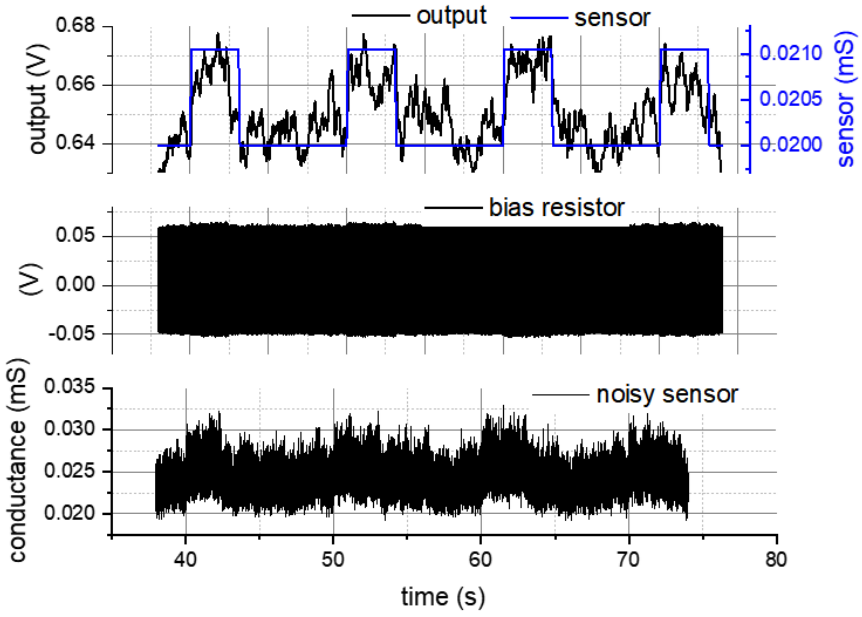

Figure 7.22: Representative signals from the circuit output (upper graph) with the simulated sensor conductivity superimposed; the voltage observed at the node between the sensor and the bias resistor (middle), and the conductance of the sensor, reflecting both the pulsed conductivity and the added 1/f noise. In this simulation there were four pulses 3s long, on a 10s period, modulating the sensor conductivity.

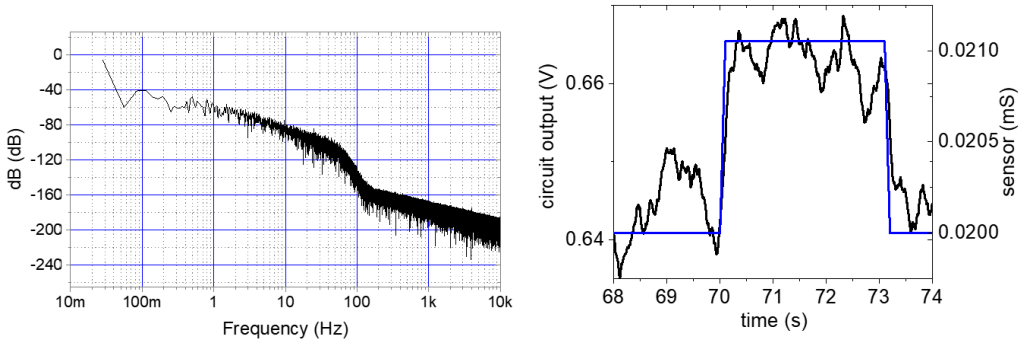

Figure 7.23: a) Fourier transform of circuit output data shown in Figure 7.22, above. Although there is significant attenuation above about 40 Hz, the broad signal at about 100 mHz, generated by the 10 Hz resistance pulses, is not much larger than the neighboring frequencies above and below. These are attributable to noise. To address this, we have averaged the four pulses as shown in b). Although there is still visible low frequency noise, the SNR is obviously improved. Note that the conductivity rise and fall times of 0.1 s have been largely followed by the averaged output. Further signal averaging would only improve the situation.

7.6 Conclusion

In this report, we have proposed a simple and portable analog lock-in amplifier circuit design using commercial components for gas sensing. The results were obtained using PSPICE simulation on commercial IC models. A lock-in amplifier (LIA) uses the phase detection method to read the sensor measurements accurately in noisy environments. We have used these two components to implement a model of a sensor of base resistance 50 kΩ, with the resistance modulated by a pulsed voltage and a parallel noisy voltage source. The changing resistance of the sensor R_{sensor} as controlled by these two sources causes the envelope of the 2 kHz signal V_{IN} measured across R_{bias} to change. Also, the output of the triangle wave generator (2^{nd} stage of function generator) will be used at the

demodulator to minimize the phase between the excitation signal driving the sensor, and the demodulator input after multiple filter stages. The sensor resistance is modulated so as to represent a 5% increase in resistance in a 3s pulse with a 0.5s rise and fall time. Then, a 7^{th} order low pass filter (LPF) was used to cancel noise and extract the absolute mean value of the data signal. We have generated 4 successive pulses of 5% change in conductivity, 3s long, on a 10s period. A flicker noise source has been added to induce changes in the resistance with a 1/f power spectrum. We show the output from the circuit superimposed on the desired information, sensor conductivity. We show conductivity here in order to maintain the direct relationship between the input and output signals. The rejection of high frequency noise in the sensor conductivity has been visibly effective, although low frequency noise persists. This is very difficult to remove here without removing information from the signal.

CHAPTER 8 : CONCLUSIONS AND FUTURE WORK

8.1 Conclusions

Researchers and developers have continued to encounter various challenges in developing chemical vapor sensor devices in terms of sensitivity, selectivity, reaction time, robustness, and other features. Graphene is one of the promising materials that has been used to address these problems in sensor applications. The goal of this dissertation was to understand which graphene samples (with and without ZnO nanoparticles functionalization) is best suited for chemiresistive sulfur sensing applications. Furthermore, devices with different geometries having engineered defects in graphene channels were investigated. For comparison purposes, all of the devices studied had the same graphene mesa area.

We find that, ZnO functionalization generally lowers noise. The resistance measurements showed that devices with long etched stripes orthogonal to the direction of the applied electric field have the highest resistance, and short and wide channel interdigitated devices have the lowest resistance for both pristine and ZnO functionalized graphene. The graphene-metal Ohmic contact resistances (R_C) demonstrate that ZnO functionalized graphene has lower contact resistance, but higher graphene sheet resistance (R_{sh}) compared to the pristine graphene. There is no strong evidence for a correlation between the scalar noise power and actual graphene channel area, contact area, and total perimeter (including the internal etched hole perimeters). However, there is a strong direct correlation between noise frequency dependence and graphene area and contact area.

Furthermore, there is an inverse correlation between noise frequency dependence and perimeter. This work highlights that the electrical and low frequency noise measurements are critical for the selection of appropriate device structure in graphene/ZnO chemical sensors.

In this work, density functional theory calculations were performed to study the interaction of decane, propyl benzene, thiophene and octanethiol molecules with graphene (with and without ZnO functionalization) to fully understand the detection properties of these nanosheets in adsorption processes. Moreover, density functional theory calculations were used to explain and verify experimental results. ZnO functionalized graphene was found to be a highly efficient sensor material for thiophene and octanethiol sensing. The results of the adsorption energy and TDOS (Fermi level shift) values show that ZnO offers a significantly more energetically favorable surface to adsorption of thiophene and octanethiol relative to hydrocarbons. The selectivity characteristics were examined by exposing pristine and ZnO functionalized graphene devices of different geometries to decane and propyl benzene. All the devices showed no response to decane and propyl benzene. These results indicate that we are sensing sulfur molecules (S) instead of hydrocarbon molecules (C and H). The current and future researchers will benefit from the results of this work.

In this dissertation, we have proposed a simple and portable analog lock-in amplifier circuit design using commercial components for gas sensing. The results were obtained using PSPICE simulation on commercial IC models.

8.2 Suggested Future Work

Further investigation of other metal oxides and metal nanoclusters may improve some of the performance indices of the sensor devices presented in this work. Furthermore, the database required for gas sensing using machine learning algorithms needs to be improved. For future research on these sensor devices, other important aspects must be considered: First, to obtain real-time environmental information, citizens and soldiers need low-power, robust, and small form-factor sensors embedded in embedded chips or plug-in modules in smart phones. Second, it would be helpful to conduct an extensive study under various extreme environmental conditions for a long period of time to make the sensor a more reliable sensor. Last, it would be appropriate to test the developed sensors against different kinds of analytes to establish whether they are suited for use as an accurate and stable sensor in the future.

REFERENCES

[1] H. O. Peierson, *Handbook of carbon, graphite, diamond and fullerenes*. New Jersey: Noyes Publications, 1993.

[2] E. H. Falcao and F. Wudl, "Carbon allotropes: beyond graphite and diamond," *J. Chem. Technol. Biotechnol.,* vol. 82, pp. 524-531, 2007.

[3] Katsnelson, Mikhail. (2007). Graphene: Carbon in Two Dimensions. Materials Today. 10. 10.1016/S1369-7021(06)71788-6.

[4] Tiwari, A.; Syvajarvi, M. *Graphene materials: Fundamentals and Emerging Applications*; Wiley: Hoboken, NJ, 2015.

[5] Feiyu, K.; Inagaki, M. *Carbon materials science and engineering: From fundamentals to applications*; Tsinghua University Press: Beijing, 2011.

[6] Inagaki, M.; Kang, F. *Materials science and engineering of carbon: Fundamentals*; Butterworth-Heinemann: Waltham, MD, 2014.

[7] Sharon, M.; Sharon, M. *Graphene: An introduction to the fundamentals and industrial applications*; Scrivener Publishing: Beverly (Mass.), 2015.

[8] Kroto, H.W., Heath, J.R., O'Brien, S.C., Curl, R.F. and Smalley, R.E. (1985) C_{60}: Buckminsterfullerene. Nature , 318, 162-163. https://doi.org/10.1038/318162a0

[9] Lu, W. Carbon nanomaterials for advanced energy systems: Advances in materials synthesis and device applications; Wiley-Blackwell: Chichester, 2014.

[10] Proctor, J.E., Melendrez Armada, D., & Vijayaraghavan, A. (2017). An Introduction to Graphene and Carbon Nanotubes (1st ed.). CRC Press.

[11] Iijima, S. Helical Microtubules of Graphitic Carbon. *Nature* 1991, *354* (6348), 56–58.

[12] Kuchibhatla, S. V. N. T.; Karakoti, A. S.; Bera, D.; Seal, S. One Dimensional Nanostructured Materials. *Progress in Materials Science* 2007, *52* (5), 699–913.

[13] K. S. Novoselov, A. K. Geim, S. Morozov, D. Jiang, Y. Zhang, S. Dubonos, *et al.*, "Electric field effect in atomically thin carbon films," *Science,* vol. 306, pp. 666-669, 2004.

[14] Adetayo, A.; Runsewe, D. Synthesis and Fabrication of Graphene and Graphene Oxide: A Review. *Open Journal of Composite Materials* 2019, *09* (02), 207–229.

[15] Wypych, G. *Graphene: Important results and applications*; ChemTec Publishing: Toronto, 2019.

[16] Simon M. Sze, K.K.N., Physics of Semiconductor Devices. Vol. 3rd. 2006, New York: John Wiley & Sons.

[17] James, F.A.J.L., Michael Faraday: A Very Short Introduction. 1st ed. 2010, Oxford: Oxford University Press. 184.

[18] Lundstrom, M., Moore's Law Forever? Science, 2003. 299 (5604): p. 210-211.

[19] Lifshits, V.G., A.A. Saranin, and A.V. Zotov, Surface phases on silicon: Preparation, structures, and properties. Other Information: PBD: 1995. 1995. Medium: X; Size: 448 p.

[20] Novoselov, K.S., et al., A roadmap for graphene. Nature, 2012. 490 (7419): p. 192-200.

[21] K.S. Novoselov, A.K. Geim, S.V. Morozov, D. Jiang, M.I. Katsnelson, I.V. Grigorieva, S.V. Dubonos, A.A. Firsov, Two-dimensional gas of massless Dirac fermions in graphene. Nature 438 (7065), 197–200 (2005).

[22] Y. Zhang, Y.W. Tan, H.L. Stormer, P. Kim, Experimental observation of the quantum Hall effect and Berry's phase in graphene. Nature 438(7065), 201–204 (2005).

[23] Y.W. Son, M.L. Cohen, S.G. Louie, Energy gaps in graphene nanoribbons. Phys. Rev. Lett. 97(21), 216803 (2006).

[24] S. Stankovich, D.A. Dikin, G.H. Dommett, K.M. Kohlhaas, E.J. Zimney, E.A. Stach, R.D. Piner, S.T. Nguyen, R.S. Ruoff, Graphene-based composite materials. Nature 442(7100), 282–286 (2006).

[25] A.K. Geim, K.S. Novoselov, The rise of graphene. Nat. Mater. 6(3), 183–191 (2007).

[26] A.H. Castro Neto, N.M.R. Peres, K.S. Novoselov, A.K. Geim, The electronic properties of graphene. Rev. Mod. Phys. 81(1), 109–162 (2009).

[27] K.I. Bolotin, K.J. Sikes, Z. Jiang, M. Klima, G. Fudenberg, J. Hone, P. Kim, H.L. Stormer, Ultrahigh electron mobility in suspended graphene. Solid State Commun. 146 (9–10), 351–355 (2008).

[28] J. T. Robinson, F.K. Perkins, E.S. Snow, Z. Wei and P.E. Sheehan, Nano Lett., 2008, 8, 3137 3140.

[29] M. Qazi, T. Vogt, and G. Koley, Appl. Phys. Lett., 2007, 91, 233101-233103.

[30] F. Niu, J.M. Liu, L.M. Tao, W. Wang, and W.G. Song, J. Mater. Chem. A, 2013, 1, 6130-6133.

[31] Wang, Q.H., Hersam, M.C. Nat. Chem. 2009, 1, 206.

[32] Si, Y., Samulski, E.T. Nano Lett. 2008, 8, 1679.

[33] Bostwick, A., Ohta, T., Seyller, T., Horn, K. Rotenberg, E. Nat. Phys. 2007, 3, 36.

[34] Ohta, T., Bostwick, A., Seyller, T., Horn, K., Rotensber, E. Sciecne 2006, 313, 951

[35] Elias, D.C., Nair, R.R, Mohiuddin, T.M.G., Morozov, S.V., Blake, P., Halsall, M.P., Ferrari, A.C., Boukhvalov, D.W., Katsneltson, M.I., Geim, A.K., Novoselov, K.S. Science 2009, 323, 610.

[36] Wang, X.R., Li, X.L., Zhang, L., Yoon, Y., Weber, P.K., Wnag, H.L., Guo, J., Dai, H.J. Science 2009, 324, 768.

[37] Kosynkin, D.V., Higginbotham, A.L., Sinitskii, A., Lomeda, J. R., Dimiev, A., Price, B.K., Tour, J.M. Nature 2009, 458, 872.

[38] Loh, K.P., Bao, Q., Ang, P.K., Yang, J.J. Mater. Chem. 2010, 20, 2277.

[39] Johnson, D.W. and S.E. Lindberg, Atmospheric deposition, and forest nutrient cycling. A synthesis of the Integrated Forest Study. 1992: Springer-Verlag.

[40] Susott, R.A., Characterization of the thermal properties of forest fuels by combustible gas analysis. Forest Science, 1982. 28(2): p. 404-420.

[41] Yamazoe, N. and T. Seiyama, Sensing mechanism of oxide semiconductor gas sensors. IEEE CH2127, 1985. 9: p.376-379.

[42] Jing Kong, Nathan R. Franklin, Chongwu Zhou, Michael G. Chapline, Shu Peng, Kyeongjae Cho, Hongjie Dai, Nanotube Molecular Wires as Chemical Sensors, Science, 28 jan 2000, Vol. 287, Issue 5453, pp. 622-625.

[43] Javaid, Mohd & Haleem, Abid & Rab, Shanay & Singh, Ravi & Suman, Rajiv. (2021). Sensors for daily life: A review. Sensors International. 2. 100121. 10.1016/j.sintl.2021.100121.

[44] National Research Council. 1995. *Expanding the Vision of Sensor Materials*. Washington, DC: The National Academies Press.https://doi.org/10.17226/4782.

[45] X-J. Huang and Y-K. Choi, Sensors and Actuators B, 122, 659 (2007).

[46] Li, S., Ge, Y., Piletsky, S. A., & Lunec, J. (2012). *Molecularly Imprinted Sensors*. Elsevier. https://doi.org/10.1016/C2010-0-69238-8

[47] Janata, J. Chemical Sensors. *Analytical Chemistry* 1992, *64* (12), 196–219.

[48] Orsini, A.; D'Amico, A. Chemical Sensors and Chemical Sensor Systems: Fundamentals Limitations and New Trends. *NATO Security Through Science Series* 69–94.

[49] Schedin, F.; Geim, A. K.; Morozov, S. V.; Hill, E. W.; Blake, P.; Katsnelson, M. I.; Novoselov, K. S. Detection of Individual Gas Molecules Adsorbed on Graphene. *Nature Materials* 2007, *6* (9), 652–655.

[50] Pearce, R.; Iakimov, T.; Andersson, M.; Hultman, L.; Spetz, A. L.; Yakimova, R. Epitaxially Grown Graphene Based Gas Sensors for Ultra Sensitive No2 Detection. *Sensors and Actuators B: Chemical* 2011, *155* (2), 451–455.

[51] Johnson, J.L., et al., *Experimental study of graphitic nanoribbon films for ammonia sensing.* Journal of Applied Physics, 2011. 109(12): p. 124301-7.

[52] Wang, H.-T., et al., *Comparison of gate and drain current detection of hydrogen at room temperature with AlGaN/GaN high electron mobility transistors.* Applied Physics Letters, 2005. 87(17): p. 172105-3.

[53] Wang, H.T., et al., *Hydrogen-selective sensing at room temperature with ZnO nanorods.* Applied Physics Letters, 2005. 86(24): p. 243503-3.

[54] Wang, H.-T., et al., *Stable hydrogen sensors from AlGaN/GaN heterostructure diodes with TiB[sub 2]-based Ohmic contacts.* Applied Physics Letters, 2007. 90(25): p. 252109-3.

[55] Chu, B.H., et al., *Hydrogen detection using platinum coated graphene grown on SiC.* Sensors and Actuators, B: Chemical, 2011. 157(2): p. 500-503.

[56] Ko, G., et al., *Graphene-based nitrogen dioxide gas sensors.* Current Applied Physics, 2010. 10(4): p. 1002-1004.

[57] Nomani, M.W.K., et al., *Highly sensitive and selective detection of NO 2 using epitaxial graphene on 6H-SiC.* Sensors and Actuators, B: Chemical, 2010. 150(1): p. 301-307.

[58] Shi, X.; Gu, W.; Li, B.; Chen, N.; Zhao, K.; Xian, Y. Enzymatic Biosensors Based on the Use of Metal Oxide Nanoparticles. Microchimica Acta 2013, 181 (1-2), 1–22.

[59] Aluri, G. S.; Motayed, A.; Davydov, A. V.; Oleshko, V. P.; Bertness, K. A.; Sanford, N. A.; Rao, M. V. Highly Selective Gan-Nanowire/tio2-Nanocluster Hybrid Sensors for Detection of Benzene and Related Environment Pollutants. *Nanotechnology* 2011, *22* (29), 295503.

[60] Kazemi, S. H.; Khajeh, K. Electrochemical Studies of a Novel Biosensor Based on the CuO Nanoparticles Coated with HORSERADISH Peroxidase to Determine the Concentration of Phenolic Compounds. *Journal of the Iranian Chemical Society* 2011, *8* (S1).

[61] Haider, S.; Kamal, T.; Khan, S. B.; Omer, M.; Haider, A.; Khan, F. U.; Asiri, A. M. Natural Polymers Supported Copper Nanoparticles for Pollutants Degradation. *Applied Surface Science* 2016, *387*, 1154–1161.

[62] Ponce, A. A.; Klabunde, K. J. Chemical and Catalytic Activity of Copper Nanoparticles Prepared via Metal Vapor Synthesis. *Journal of Molecular Catalysis A: Chemical* 2005, *225* (1), 1–6.

[63] Jagadeesh, R. V.; Surkus, A.-E.; Junge, H.; Pohl, M.-M.; Radnik, J.; Rabeah, J.; Huan, H.; Schunemann, V.; Bruckner, A.; Beller, M. Nanoscale Fe2O3-Based Catalysts for Selective Hydrogenation OF Nitroarenes to Anilines. *Science* 2013, *342* (6162), 1073–1076.

[64] Wu, C.; Yin, P.; Zhu, X.; OuYang, C.; Xie, Y. Synthesis of Hematite (α-fe2o3) Nanorods: Diameter-Size and Shape Effects on Their Applications in MAGNETISM, Lithium Ion Battery, and Gas Sensors. *The Journal of Physical Chemistry B* 2006, *110* (36), 17806–17812.

[65] Han, J. S.; Bredow, T.; Davey, D. E.; Yu, A. B.; Mulcahy, D. E. The Effect of AL Addition on the Gas SENSING Properties of fe2o3-Based Sensors. *Sensors and Actuators B: Chemical* 2001, *75* (1-2), 18–23.

[66] Comini, E.; Guidi, V.; Frigeri, C.; Riccò, I.; Sberveglieri, G. Co Sensing Properties of Titanium and Iron Oxide Nanosized Thin Films. *Sensors and Actuators B: Chemical* 2001, *77* (1-2), 16–21.

[67] Lin, C.-W.; Chen, H.-I.; Chen, T.-Y.; Huang, C.-C.; Hsu, C.-S.; Liu, R.-C.; Liu, W.-C. On an Indium–Tin-Oxide Thin Film Based Ammonia Gas Sensor. *Sensors and Actuators B: Chemical* 2011, *160* (1), 1481–1484.

[68] Yoo, K. S.; Park, S. H.; Kang, J. H. Nano-Grained Thin-Film Indium Tin Oxide Gas Sensors for h2 Detection. *Sensors and Actuators B: Chemical* 2005, *108* (1-2), 159–164.

[69] Vaishnav, V. S.; Patel, P. D.; Patel, N. G. Preparation and Characterization of Indium Tin Oxide Thin Films for Their Application as Gas Sensors. *Thin Solid Films* 2005, *487* (1-2), 277–282.

[70] Navale, Y. H.; Navale, S. T.; Ramgir, N. S.; Stadler, F. J.; Gupta, S. K.; Aswal, D. K.; Patil, V. B. Zinc Oxide Hierarchical Nanostructures as Potential no2 Sensors. Sensors and Actuators B: Chemical 2017, 251, 551–563.

[71] Noh, J. H.; Han, H. S.; Lee, S.; Kim, D. H.; Park, J. H.; Park, S.; Kim, J. Y.; Jung, H. S.; Hong, K. S. A Newly Designed Nb-Doped tio2/Al-Doped Zno Transparent Conducting Oxide Multilayer for Electrochemical Photoenergy Conversion Devices. *The Journal of Physical Chemistry C* 2010, *114* (32), 13867–13871.

[72] Park, T.-Y.; Choi, Y.-S.; Kang, J.-W.; Jeong, J.-H.; Park, S.-J.; Jeon, D. M.; Kim, J. W.; Kim, Y. C. Enhanced Optical Power and Low Forward Voltage OF GaN-Based Light-Emitting Diodes with Ga-Doped ZnO Transparent Conducting Layer. *Applied Physics Letters* 2010, *96* (5), 051124.

[73] Rumyantsev, S.; Liu, G.; Shur, M. S.; Potyrailo, R. A.; Balandin, A. A. Selective Gas Sensing with a Single Pristine Graphene Transistor. *Nano Letters* 2012, *12* (5), 2294–2298.

[74] H. P. Boehm, R. Setton, and E. Stumpp, "Nomenclature and terminology of graphite-intercalation compounds," *Pure and Applied Chemistry*, vol. 66, pp. 1893-1901, Sep. 1994.

[75] J. C. Slonczewski and P. R. Weiss, "Band structure of graphite," *Physical Review*, vol. 109, pp. 272-279, 1958.

[76] Andrews, D. L.; Lipson, R. H.; Nann, T. *Comprehensive nanoscience and nanotechnology*; Academic Press: London, 2019.

[77] A. J. Vanbommel, J. E. Crombeen, and A. Vantooren, "Leed and Auger-electron observations of SiC (0001) surface," *Surface Science*, vol. 48, pp. 463-472, 1975.

[78] N. D. Mermin, "Crystalline order in two dimensions," *Physical Review*, vol. 176, p. 250, 1968.

[79] J. Venables, G. Spiller, and M. Hanbucken, "Nucleation and growth of thin films," *Rep. Prog. Phys.*, vol. 47, p. 399, 1984.

[80] J. Evans, P. Thiel, and M. Bartelt, "Morphological evolution during epitaxial thin film growth: Formation of 2D islands and 3D mounds," *Surf. Sci. Rep.*, vol. 61, pp. 1-128, 2006.

[81] N. D. Mermin, "Crystalline order in 2 dimensions," *Physical Review*, vol. 176, pp. 250-254, 1968.

[82] E. Fradkin, "Critical-behavior of disordered degenerate semiconductors II - Spectrum and transport properties in mean-field theory," *Physical Review B,* vol. 33, pp. 3263-3268, Mar. 1986.

[83] K. S. Novoselov, D. Jiang, F. Schedin, T. J. Booth, V. V. Khotkevich, S. V. Morozov, and A. K. Geim, "Two-dimensional atomic crystals," *Proceedings of the National Academy of Sciences of the United States of America,* vol. 102, pp. 10451-10453, Jul. 2005.

[84] Q. H. Wang, K. Kalantar-Zadeh, A. Kis, J. N. Coleman, and M. S. Strano, "Electronics and optoelectronics of two-dimensional transition metal dichalcogenides," *Nature Nanotech.,* vol. 7, pp. 699-712, 2012.

[85] C. Lee, X. Wei, J. W. Kysar, and J. Hone, "Measurement of the elastic properties and intrinsic strength of monolayer graphene," *Science,* vol. 321, pp. 385-388, 2008.

[86] R. Nair, P. Blake, A. Grigorenko, K. Novoselov, T. Booth, T. Stauber, *et al.,* "Fine structure constant defines visual transparency of graphene," *Science,* vol. 320, pp. 1308-1308, 2008.

[87] J. S. Bunch, S. S. Verbridge, J. S. Alden, A. M. van der Zande, J. M. Parpia, H. G. Craighead, *et al.,* "Impermeable atomic membranes from graphene sheets," *Nano Lett.,* vol. 8, pp. 2458-2462, 2008.

[88] A. Peigney, C. Laurent, E. Flahaut, R. Bacsa, and A. Rousset, "Specific surface area of carbon nanotubes and bundles of carbon nanotubes," *Carbon,* vol. 39, pp. 507-514, 2001.

[89] A. A. Balandin, S. Ghosh, W. Bao, I. Calizo, D. Teweldebrhan, F. Miao, *et al.,* "Superior thermal conductivity of single-layer graphene," *Nano Lett.,* vol. 8, pp. 902-907, 2008.

[90] J.-H. Chen, C. Jang, S. Xiao, M. Ishigami, and M. S. Fuhrer, "Intrinsic and extrinsic performance limits of graphene devices on SiO2," *Nature Nanotech.,* vol. 3, pp. 206-209, 2008.

[91] A. Tzalenchuk, S. Lara-Avila, A. Kalaboukhov, S. Paolillo, M. Syväjärvi, R. Yakimova, *et al.,* "Towards a quantum resistance standard based on epitaxial graphene," *Nature Nanotech.,* vol. 5, pp. 186-189, 2010.

[92] S. V. Morozov, K. S. Novoselov, M. I. Katsnelson, F. Schedin, D. C. Elias, J. A. Jaszczak, *et al.,* "Giant Intrinsic Carrier Mobilities in Graphene and Its Bilayer," *Phys. Rev. Lett.,* vol. 100, p. 016602, 01/07/ 2008.

[93] K. I. Bolotin, K. Sikes, Z. Jiang, M. Klima, G. Fudenberg, J. Hone, *et al.*, "Ultrahigh electron mobility in suspended graphene," *Solid State Commun.*, vol. 146, pp. 351-355, 2008.

[94] A. K. Geim and A. H. MacDonald, "Graphene: Exploring carbon flatland," *Physics Today*, vol. 60, pp. 35-41, Aug. 2007.

[95] P. R. Wallace, "The band theory of graphite," *Physical Review*, vol. 71, p. 622, 1947.

[96] Sharma, K. R. *Graphene nanomaterials*; Momentum Press: New York, 2014.

[97] Wolf, E. L. Graphene: A new paradigm in Condensed matter and device physics; Oxford University Press: Oxford, 2014.

[98] Skákalová Viera; Kaiser, A. B. *Graphene: Properties, preparation, characterisation and devices*; Woodhead Publishing: Oxford, 2021.

[99] A. Bostwick, T. Ohta, J. L. McChesney, K. V. Emtsev, T. Seyller, K. Horn, *et al.*, "Symmetry breaking in few layer graphene films," *New J. Phys.*, vol. 9, p. 385, 2007.

[100] Hass, J.; de Heer, W. A.; Conrad, E. H. The Growth and Morphology of Epitaxial Multilayer Graphene. *Journal of Physics: Condensed Matter* 2008, *20* (32), 323202.

[101] Zhang, Y.; Zhang, L.; Zhou, C. Review of Chemical Vapor Deposition of Graphene and Related Applications. *Accounts of Chemical Research* 2013, *46* (10), 2329–2339.

[102] Reina, A.; Jia, X.; Ho, J.; Nezich, D.; Son, H.; Bulovic, V.; Dresselhaus, M. S.; Kong*, J. Layer Area, Few-Layer Graphene Films on Arbitrary Substrates by Chemical Vapor Deposition. *Nano Letters* 2009, *9* (8), 3087–3087.

[103] Ashcroft, N. W.; Mermin, N. D.; Rodriguez, S. *Solid State Physics*. *American Journal of Physics* 1978, *46* (1), 116–117.

[104] Sutter, P. How Silicon Leaves the Scene. *Nature Materials* 2009, *8* (3), 171–172.

[105] Novoselov, K. S.; Castro Neto, A. H. Two-Dimensional Crystals-Based Heterostructures: Materials with Tailored Properties. *Physica Scripta* 2012, *T146*, 014006.

[106] Lu, X.; Yu, M.; Huang, H.; Ruoff, R. S. Tailoring Graphite with the Goal of Achieving Single Sheets. *Nanotechnology* 1999, *10* (3), 269–272.

[107] Zhu, W.; Perebeinos, V.; Freitag, M.; Avouris, P. Carrier Scattering, Mobilities, and Electrostatic Potential in Monolayer, Bilayer, and Trilayer Graphene. *Physical Review B* 2009, *80* (23).

[108] X. Li, W. Cai, J. An, S. Kim, J. Nah, D. Yang, R. Piner, A. Velamakanni, I. Jung, E. Tutuc, S. K. Banerjee, L. Colombo, and R. S. Ruo, “Large-area synthesis of high-quality and uniform graphene films on copper foils.", Science (New York, N.Y.), vol. 324, no. 5932, pp. 1312-4, Jun. 2009.

[109] P. J. Ko, H. Takahashi, S. Koide, H. Sakai, T. V. Thu, H. Okada, and A. Sandhu, “Simple method to transfer graphene from metallic catalytic substrates to flexible surfaces without chemical etching", Journal of Physics: Conference Series, vol. 433, p. 012 002, Apr. 2013.

[110] F. Bonaccorso, A. Lombardo, T. Hasan, Z. Sun, L. Colombo, and A. C. Ferrari, "Production and processing of graphene and 2d crystals," *Mater. Today,* vol. 15, pp. 564-589, 2012.

[111] R. Muñoz and C. Gómez-Aleixandre, "Review of CVD Synthesis of Graphene," *Chem. Vap. Deposition,* vol. 19, pp. 297-322, 2013.

[112] X. Li, C. W. Magnuson, A. Venugopal, J. An, J. W. Suk, B. Han, *et al.*, "Graphene Films with Large Domain Size by a Two-Step Chemical Vapor Deposition Process," *Nano Lett.,* vol. 10, pp. 4328-4334, 2010/11/10 2010.

[113] S. Bae, H. Kim, Y. Lee, X. Xu, J.-S. Park, Y. Zheng, *et al.*, "Roll-to-roll production of 30-inch graphene films for transparent electrodes," *Nature Nanotech.,* vol. 5, pp. 574-578, 2010.

[114] P. Y. Huang, C. S. Ruiz-Vargas, A. M. van der Zande, W. S. Whitney, M. P. Levendorf, J. W. Kevek, *et al.*, "Grains and grain boundaries in single-layer graphene atomic patchwork quilts," *Nature,* vol. 469, pp. 389-392, 2011.

[115] Z. Cheng, Q. Zhou, C. Wang, Q. Li, C. Wang, and Y. Fang, "Toward intrinsic graphene surfaces: a systematic study on thermal annealing and wet-chemical treatment of SiO2-supported graphene devices," *Nano Lett.,* vol. 11, pp. 767-771, 2011.

[116] C. Berger, Z. Song, X. Li, X. Wu, N. Brown, C. Naud, D. Mayou, T. Li, J. Hass, A. N. Marchenkov, E. H. Conrad, P. N. First, and W. a. de Heer, “Electronic confinement and coherence in patterned epitaxial graphene.", Science (New York, N.Y.), vol. 312, no. 5777, pp. 1191-6, May 2006. doi: 10.1126/science.1125925.

[117] Ashcroft, N. W.; Mermin, N. D. *Solid state physics*; Cengage Learning: Patparganj, Delhi, 2017.

[118] Hass, J., Varchon, F., Millán-Otoya, J. E., Sprinkle, M., Sharma, N., de Heer, W. A., Berger, C., First, P. N., Magaud, L., & Conrad, E. H. (2008). Why multilayer graphene on 4H-SiC (0001) behaves like a single sheet of graphene. *Physical review letters*, *100*(12), 125504.

[119] A. Mattausch and O. Pankratov, Ab initio study of graphene on SiC, Phys. Rev. Lett., 2007, 99, 076802.

[120] F. Varchon, R. Feng, J. Hass, X. Li, B. NgocNguyen, C. Naud, P. Mallet, J. Y. Veuille, C. Berger, E. H. Conrad and L. Magaud, Electronic structure of epitaxial graphene layers on SiC: effect of the substrate, Phys. Rev. Lett., 2007, 99, 126805

[121] W. Norimatsu and M. Kusunoki, "Transitional structures of the interface between graphene and 6H–SiC (0001)", Chem. Phys. Lett. 2009, 468, 52-56.

[122] J. A. Robinson, M. Wetherington, J. L. Tedesco, P. M. Campbell, X. Weng, J. Stitt, M. a. Fanton, E. Frantz, D. Snyder, B. L. VanMil, G. G. Jernigan, R. L. Myers-Ward, C. R. Eddy, and D. K. Gaskill, "Correlating Raman spectral signatures with carrier mobility in epitaxial graphene: a guide to achieving high mobility on the wafer scale.", Nano letters, vol. 9, no. 8, pp. 2873{6, Aug. 2009. doi: 10.1021/nl901073g.

[123] Z. Guo, R. Dong, P. S. Chakraborty, N. Lourenco, J. Palmer, Y. Hu, M. Ruan, J. Hankinson, J. Kunc, J. D. Cressler, C. Berger, and W. a. de Heer, "Record maximum oscillation frequency in C-face epitaxial graphene transistors.", Nano letters, vol. 13, no. 3, pp. 942-7, Mar. 2013. doi: 10.1021/nl303587r.

[124] Gaskill, D. K.; Jernigan, G.; Campbell, P.; Tedesco, J. L.; Culbertson, J.; VanMil, B.; Myers-Ward, R. L.; Eddy, C.; Moon, J.; Curtis, D.; Hu, M.; Wong, D.; McGuire, C.; Robinson, J.; Fanton, M.; Stitt, T.; Stitt, T.; Snyder, D.; Wang, X.; Frantz, E. Epitaxial Graphene Growth on SIC Wafers. *ECS Transactions* 2009, *19* (5), 117–124.

[125] S. M. Song, J. K. Park, O. J. Sul, and B. J. Cho, "Determination of work function of graphene under a metal electrode and its role in contact resistance," *Nano Lett.*, vol. 12, pp. 3887-3892, 2012.

[126] K. Nagashio and A. Toriumi, "Density-of-states limited contact resistance in graphene field-effect transistors," *Jpn. J. Appl. Phys.*, vol. 50, p. 0108, 2011.

[127] T. Mueller, F. Xia, M. Freitag, J. Tsang, and P. Avouris, "Role of contacts in graphene transistors: A scanning photocurrent study," *Phys. Rev. B*, vol. 79, p. 245430, 2009.

[128] E. Watanabe, A. Conwill, D. Tsuya, and Y. Koide, "Low contact resistance metals for graphene based devices," *Diamond Relat. Mater.*, vol. 24, pp. 171-174, 2012.

[129] G. Giovannetti, P. Khomyakov, G. Brocks, V. Karpan, J. Van den Brink, and P. Kelly, "Doping graphene with metal contacts," *Phys. Rev. Lett.*, vol. 101, p. 026803, 2008.

[130] P. Khomyakov, G. Giovannetti, P. Rusu, G. Brocks, J. Van den Brink, and P. Kelly, "First-principles study of the interaction and charge transfer between graphene and metals," *Phys. Rev. B*, vol. 79, p. 195425, 2009.

[131] Y. Ren, S. Chen, W. Cai, Y. Zhu, C. Zhu, and R. S. Ruoff, "Controlling the electrical transport properties of graphene by in situ metal deposition," *Appl. Phys. Lett.*, vol. 97, p. 053107, 2010.

[132] B. Hammer, J.K. Norskov, Why gold is the noblest of all the metals, Nature. 376 (1995) 238–240. doi:10.1038/376238a0.

[133] J. Wintterlin and M. L. Bocquet, "Graphene on metal surfaces," *Surf. Sci.*, vol. 603, pp. 1841-1852, 6/1/ 2009.

[134] P. Merino, M. Švec, A. L. Pinardi, G. Otero, and J. A. Martín-Gago, "Strain-driven moiré superstructures of epitaxial graphene on transition metal surfaces," *ACS Nano*, vol. 5, pp. 5627-5634, 2011.

[135] J. Moon, D. Curtis, M. Hu, D. Wong, C. McGuire, P. Campbell, *et al.*, "Epitaxial-graphene RF field-effect transistors on Si-face 6H-SiC substrates," *IEEE Electron Device Lett.*, vol. 30, pp. 650-652, 2009.

[136] Y. M. Lin, K. A. Jenkins, A. Valdes-Garcia, J. P. Small, D. B. Farmer, and P. Avouris, "Operation of graphene transistors at gigahertz frequencies," *Nano Lett.*, vol. 9, pp. 422-426, 2008.

[137] J. Kedzierski, H. Pei-Lan, P. Healey, P. W. Wyatt, C. L. Keast, M. Sprinkle, *et al.*, "Epitaxial Graphene Transistors on SiC Substrates," *IEEE Trans. Electron Devices*, vol. 55, pp. 2078-2085, 2008.

[138] Y. J. Shin, Y. Wang, H. Huang, G. Kalon, A. T. S. Wee, Z. Shen, *et al.*, "Surface-energy engineering of graphene," *Langmuir*, vol. 26, pp. 3798-3802, 2010.

[139] J. E. Johns and M. C. Hersam, "Atomic covalent functionalization of graphene," *Acc. Chem. Res.*, vol. 46, pp. 77-86, 2012.

[140] V. Georgakilas, M. Otyepka, A. B. Bourlinos, V. Chandra, N. Kim, K. C. Kemp, *et al.*, "Functionalization of graphene: covalent and non-covalent approaches, derivatives and applications," *Chem. Rev.*, vol. 112, pp. 6156-6214, 2012.

[141] J. M. Englert, C. Dotzer, G. Yang, M. Schmid, C. Papp, J. M. Gottfried, *et al.*, "Covalent bulk functionalization of graphene," *Nature Chem.*, vol. 3, pp. 279-286, 2011.

[142] H. Bai, Y. Xu, L. Zhao, C. Li, and G. Shi, "Non-covalent functionalization of graphene sheets by sulfonated polyaniline," *Chem. Commun.*, pp. 1667-1669, 2009.

[143] Kuila, T.; Bose, S.; Mishra, A.K.; Khanra, P.; Kim, N.H.; Lee, J.H. Chemical Functionalization of Graphene and Its Applications. Prog. Mater. Sci. 2012, 57, 1061–1105.

[144] Liu, J.; Tang, J.; Gooding, J.J. Strategies for Chemical Modification of Graphene and Applications of Chemically Modified Graphene. J. Mater. Chem. 2012, 22, 12435.

[145] F. E. Karlický, K. Kumara Ramanatha Datta, M. Otyepka, and R. Zboril, "Halogenated Graphenes: Rapidly Growing Family of Graphene Derivatives," *ACS Nano,* vol. 7, pp. 6434-6464, 2013.

[146] Sreeprasad, T.S.; Berry, V. How Do the Electrical Properties of Graphene Change with Its Functionalization? Small 2012, 9, 341–350.

[147] R. Balog, B. Jørgensen, L. Nilsson, M. Andersen, E. Rienks, M. Bianchi, *et al.*, "Bandgap opening in graphene induced by patterned hydrogen adsorption," *Nature Mater.*, vol. 9, pp. 315-319, 2010.

[148] K. J. Jeon, Z. Lee, E. Pollak, L. Moreschini, A. Bostwick, C. M. Park, *et al.*, "Fluorographene: a wide bandgap semiconductor with ultraviolet luminescence," *ACS Nano,* vol. 5, pp. 1042-1046, 2011.

[149] P. G. Nanocomposites, "Graphene Functionalization: A Review," 2012.

[150] H. Liu, Y. Liu, and D. Zhu, "Chemical doping of graphene," *J. Mater. Chem.,* vol. 21, pp. 3335-3345, 2011.

[151] A. Van der Ziel, *Noise. Sources, characterization, measurement*. Prentice-Hall, 1970.

[152] P. O. Lauritzen, “Low-frequency generation noise in junction field effect transistors,” *Solid. State. Electron.*, vol. 8, pp. 41–58, 1965.

[153] A. Van Der Ziel, “Thermal noise in field-effect transistors,” *Proc. IRE*, no. 5, pp. 1808–1812, 1962.

[154] F. N. Hooge, “On the additivity of generation–recombination spectra. Part 1: Conduction band with two centres,” *Phys. B Condens. Matter*, vol. 311, no. 3–4, pp. 238–249, Feb. 2002.

[155] F. N. Hooge, “On the additivity of generation-recombination spectra. Part 2: 1/f noise,” *Phys. B Condens. Matter*, vol. 336, no. 3–4, pp. 236–251, Aug. 2003.

[156] L. K. J. Vandamme and F. N. Hooge, “On the additivity of generation-recombination spectra Part 3: The McWhorter model for 1/f noise in MOSFETs,” *Phys. B Condens. Matter*, vol. 357, no. 3–4, pp. 507–524, Mar. 2005.

[157] R. P. Jindal, “Model for mobility fluctuation 1/f noise,” *Appl. Phys. Lett.*, vol. 38, no. 4, p. 290, 1981.

[158] A. L. McWhorter, “1/f noise and related surface effects in germanium.,” 1955.

[159] A. Einstein, “On the movement of small particles suspended in stationary liquids required by the molecular-kinetic theory of heat”, *Annalen der Physik*, vol. 17, pp. 549-560, 1905.

[160] J. Johnson, “Thermal Agitation of Electricity in Conductors”, *Physical Review*, vol. 32, no. 1, pp. 97-109, Jul. 1928.

[161] H. Nyquist, “Thermal Agitation of Electric Charge in Conductors”, *Physical Review*, vol. 32, no. 1, pp. 110-113, Jul. 1928.

[162] L. Vandamme, “Noise as a diagnostic tool for quality and reliability of electronic devices”, *Electron Devices, IEEE Transactions on*, vol. 41, no. 11, pp. 2176–2187, 2002.

[163] W. Schottky, “On Spontaneous Current Fluctuations in Various Electricity Conductors”, *Annalen der Physik*, vol. 57, pp. 541-567, 1918.

[164] M. V. Haartman and M. Östling, *Low-frequency noise in advanced MOS devices*. Springer, 2007, p. 216.

[165]] J. Johnson, “The Schottky Effect in Low Frequency Circuits”, *Physical Review*, vol. 26, no. 1, pp. 71-85, Jul. 1925.

[166] R. Voss and J. Clarke, “Flicker (1/f) noise: Equilibrium temperature and resistance fluctuations,” *Phys. Rev. B*, vol. 13, no. 2, pp. 556–573, Jan. 1976.

[167] S. Kogan, *Electronic Noise and Fluctuations in Solids*. Cambridge: Cambridge University Press, 1996.

[168] M. Mihaila, “1/f Noise in Nanomaterials and Nanostructures: Old Questions in a New Fashion”, *Advanced experimental methods for noise research in nanoscale electronic devices*, pp. 19–27, 2005.

[169] F. Hooge and L. K. J. Vandamme, “Lattice scattering causes 1/*f* noise”, *Physics Letters A*, vol. 66, no. 4, pp. 315-316, May. 1978.

[170] G. Ghibaudo and O. Roux-dit-Buisson, “Low Frequency Fluctuations in Scaled Down Silicon CMOS Devices Status and Trends”, in *Solid State Device Research Conference, 1994. ESSDERC’94. 24th European*, 1994, pp. 693–700.

[171] M. Ishigami, J. H. Chen, E. D. Williams, D. Tobias, Y. F. Chen, and M. S. Fuhrer, “Hooge’s constant for carbon nanotube field effect transistors”, *Applied Physics Letters*, vol. 88, no. 20, p. 203116, 2006.

[172] H. W. C. POSTMA, “Carbon nanotube junctions and devices”, University of Delft, 2001.

[173] J. Bernamont, “Fluctuations in the resistance of thin films”, *Proceedings of the Physical Society*, vol. 49, no. 4, pp. 138-139, Aug. 1937.

[174] M. Surdin, “Fluctuations de courant thermionique et le « Flicker effect »“, *Journal de Physique et le Radium*, vol. 10, no. 4, pp. 188-189, 1939.

[175] A. van Der Ziel, “Unified presentation of 1/f noise in electron devices: fundamental 1/f noise sources”, *Proceedings of the IEEE*, vol. 76, no. 3, pp. 233-258, Mar. 1988.

[176] A. Raychaudhuri, “Measurement of 1/f noise and its application in materials science”, *Current Opinion in Solid State and Materials Science*, vol. 6, no. 1, pp. 67-85, Feb. 2002.

[177] M. Jamal Deen, B. Iñiguez, O. Marinov, and F. Lime, “Electrical studies of semiconductor dielectric interfaces”, *Journal of Materials Science: Materials in Electronics*, vol. 17, no. 9, pp. 663-683, Sep. 2006.

[178] L. K. J. Vandamme, “Bulk and surface 1/f noise”, *IEEE Transactions on Electron Devices*, vol. 36, no. 5, pp. 987-992, May. 1989.

[179] F. Hooge, “Discussion of recent experiments on 1/*f* noise”, *Physica*, vol. 60, no. 1, pp. 130-144, Jul. 1972.

[180] A. L. McWhorter, *Semiconductor Surface Physics*. University of Pennsylvania, Philadelphia, 1957, pp. 207–228.

[181] P. Dutta and P. Horn, “Low-frequency fluctuations in solids: 1f noise”, *Reviews of Modern Physics*, vol. 53, no. 3, pp. 497-516, Jul. 1981.

[182] Nyakiti, L.O.; Wheeler, V.D.; Garces, N.Y.; Myers-Ward, R.L.; Eddy, C.R.; Gaskill, D.K. Enabling Graphene-Based Technologies: TowardWafer-Scale Production of Epitaxial Graphene. MRS Bull. **2012**, 37, 1149–1157.

[183] Nath, A.; Koehler, A.D.; Jernigan, G.G.; Wheeler, V.D.; Hite, J.K.; Hernández, S.C.; Robinson, Z.R.; Garces, N.Y.; Myers-Ward, R.L.; Eddy, C.R.; et al. Achieving Clean Epitaxial Graphene Surfaces Suitable for Device Applications by Improved Lithographic Process. Appl. Phys. Lett. **2014**, 104, 224102.

[184] Nath, A.; Currie, M.; Boyd, A.K.; Wheeler, V.D.; Koehler, A.D.; Tadjer, M.J.; Robinson, Z.R.; Sridhara, K.; Hernandez, S.C.; Wollmershauser, J.A.; et al. In Search of Quantum-Limited Contact Resistance: Understanding the Intrinsic and Extrinsic Effects on the Graphene–Metal Interface. 2D Mater. **2016**, 3, 025013.

[185] Lock, E.H.; Prestigiacomo, J.C.; Dev, P.; Nath, A.; Myers-Ward, R.L.; Reinecke, T.L.; Gaskill, D.K.; Osofsky, M.S. Quantum Transport in Functionalized Epitaxial Graphene without Electrostatic Gating. Carbon **2021**, 175, 490–498.

[186] Lock, E.H.; Perkins, F.K.; Boyd, A.K.; Myers-ward, R.L.; Gaskill, D.K.; Nath, A. Graphene-Based ppb Level Sulfur Detector in Fuels. U.S. Patent WO 20190107524, 11 April 2019.

[187] Ratinac, K.R.; Yang,W.; Ringer, S.P.; Braet, F. Toward Ubiquitous Environmental Gas Sensors—Capitalizing on the Promise of Graphene. Environ. Sci. Technol. **2010**, 44, 1167–1176.

[188] Potyrailo, R.A.; Surman, C.; Nagraj, N.; Burns, A. Materials and Transducers Toward Selective Wireless Gas Sensing. Chem. Rev. **2011**, 111, 7315–7354.

[189] Rumyantsev, S.; Liu, G.; Stillman, W.; Shur, M.; Balandin, A.A. Electrical and Noise Characteristics of Graphene Field-Effect Transistors: Ambient Effects, Noise Sources and Physical Mechanisms. J. Phys. Condens. Matter **2010**, 22, 395302.

[190] Liu, G.; Rumyantsev, S.; Shur, M.S.; Balandin, A.A. Origin of 1/f Noise in Graphene Multilayers: Surface vs. Volume. Appl. Phys. Lett. **2013**, 102, 093111.

[191] Xia, F.; Perebeinos, V.; Lin, Y.-ming; Wu, Y.; Avouris, P. The Origins and Limits of Metal–Graphene Junction Resistance. Nat. Nanotechnol. **2011**, 6, 179–184.

[192] Chae, H.K.; Siberio-Pérez, D.Y.; Kim, J.; Go, Y.B.; Eddaoudi, M.; Matzger, A.J.; O'Keeffe, M.; Yaghi, O.M. A Route to High Surface Area, Porosity and Inclusion of Large Molecules in Crystals. Nature 2004, 427, 523–527.

[193] Yavari, F.; Koratkar, N. Graphene-Based Chemical Sensors. J. Phys. Chem. Lett. 2012, 3, 1746–1753.

[194] Boukhvalov, D.W.; Katsnelson, M.I. Chemical Functionalization of Graphene. J. Phys. Condens. Matter 2009, 21, 344205

[195] Yan, L.; Zheng, Y.B.; Zhao, F.; Li, S.; Gao, X.; Xu, B.; Weiss, P.S.; Zhao, Y. Chemistry and Physics of a Single Atomic Layer: Strategies and Challenges for Functionalization of Graphene and Graphene-Based Materials. Chem. Soc. Rev. 2012, 41, 97–114.

[196] Parrish, K.N.; Akinwande, D. Impact of Contact Resistance on the Transconductance and Linearity of Graphene Transistors. Appl. Phys. Lett. 2011, 98, 183505.

[197] Lee, J.; Kim, Y.; Shin, H.-J.; Lee, C.S.; Lee, D.; Moon, C.-Y.; Lim, J.; Chan Jun, S. Clean Transfer of Graphene and Its Effect on Contact Resistance. Appl. Phys. Lett. 2013, 103, 103104.

[198] Pirkle, A.; Chan, J.; Venugopal, A.; Hinojos, D.; Magnuson, C.W.; McDonnell, S.; Colombo, L.; Vogel, E.M.; Ruoff, R.S.;Wallace, R.M. The Effect of Chemical Residues on the Physical and Electrical Properties of Chemical Vapor Deposited Graphene Transferred to SiO_2. Appl. Phys. Lett. 2011, 99, 122108.

[199] Venugopal, A.; Colombo, L.; Vogel, E.M. Contact Resistance in Few and Multilayer Graphene Devices. Appl. Phys. Lett. 2010, 96, 013512.

[200] Russo, S.; Craciun, M.F.; Yamamoto, M.; Morpurgo, A.F.; Tarucha, S. Contact Resistance in Graphene-Based Devices. Phys. E Low Dimens. Syst. Nanostruct. 2010, 42, 677–679.

[201] Robinson, J.A.; LaBella, M.; Zhu, M.; Hollander, M.; Kasarda, R.; Hughes, Z.; Trumbull, K.; Cavalero, R.; Snyder, D. Contacting Graphene. Appl. Phys. Lett. 2011, 98, 053103.

[202] Li, W.; Liang, Y.; Yu, D.; Peng, L.; Pernstich, K.P.; Shen, T.; Hight Walker, A.R.; Cheng, G.; Hacker, C.A.; Richter, C.A.; et al. Ultraviolet/Ozone Treatment to Reduce Metal-Graphene Contact Resistance. Appl. Phys. Lett. 2013, 102, 183110.

[203] Gahoi, A.; Wagner, S.; Bablich, A.; Kataria, S.; Passi, V.; Lemme, M.C. Contact Resistance Study of Various Metal Electrodes with CVD Graphene. Solid-State Electron. 2016, 125, 234–239.

[204] Moon, J.S.; Antcliffe, M.; Seo, H.C.; Curtis, D.; Lin, S.; Schmitz, A.; Milosavljevic, I.; Kiselev, A.A.; Ross, R.S.; Gaskill, D.K.; et al. Ultra-Low Resistance Ohmic Contacts in Graphene Field Effect Transistors. Appl. Phys. Lett. 2012, 100, 203512.

[205] Balandin, A.A. Low-Frequency 1/f Noise in Graphene Devices. Nat. Nanotechnol. 2013, 8, 549–555.

[206] von Haartman, M. Low-Frequency Noise Characterization, Evaluation and Modeling of Advanced Si- and SiGe-Based CMOS Transistors. Doctoral Dissertation, Royal Institute of Technology (KTH), Stockholm, Sweden, 2006.

[207] Hooge, F.N. 1/f Noise Sources. IEEE Trans. Electron Devices 1994, 41, 1926–1935.

[208] Peng, S.; Jin, Z.; Ma, P.; Zhang, D.; Shi, J.; Niu, J.; Wang, X.; Wang, S.; Li, M.; Liu, X.; et al. The Sheet Resistance of Graphene under Contact and Its Effect on the Derived Specific Contact Resistivity. Carbon 2015, 82, 500–505.

[209] Ishigami, M.; Chen, J.H.; Cullen,W.G.; Fuhrer, M.S.;Williams, E.D. Atomic Structure of Graphene on SiO2. Nano Lett. 2007, 7, 1643–1648.

[210] Der Ziel, A.V. Noise: Sources, Characterization, Measurement; Prentice-Hall: Englewood Cliffs, NJ, USA, 1971.

[211] Galstyan, V.; Comini, E.; Kholmanov, I.; Faglia, G.; Sberveglieri, G. Reduced Graphene Oxide/Zno Nanocomposite for Application in Chemical Gas Sensors. RSC Adv. 2016, 6, 34225–34232.

[212] Fu, H.; Jiang, Y.; Ding, J.; Zhang, J.; Zhang, M.; Zhu, Y.; Li, H. Zinc Oxide Nanoparticle Incorporated Graphene Oxide as Sensing Coating for Interferometric Optical Microfiber for Ammonia Gas Detection. Sens. Actuators B Chem. 2018, 254, 239–247.

[213] Zhang, X.; Wu, Z.; Zheng, H.; Ren, Q.; Zou, Z.; Mei, L.; Zhang, Z.; Xia, Y.; Lin, C.-T.; Zhao, P.; et al. High-Quality Graphene Transfer via Directional Etching of Metal Substrates. Nanoscale 2019, 11, 16001–16006.

[214] Chen, J.; Gao, X. Directional Dependence of Electrical and Thermal Properties in Graphene-Nanoplatelet-Based Composite Materials. Results Phys. 2019, 15, 102608.

[215] Cho, J.; Lee, H.; Nam, K.-H.; Yeo, H.; Yang, C.-M.; Seong, D.G.; Lee, D.; Kim, S.Y. Enhanced Electrical Conductivity of Polymer Nanocomposite Based on Edge-

Selectively Functionalized Graphene Nanoplatelets. Compos. Sci. Technol. **2020**, 189, 108001.
[216] Schroder, D.K. Semiconductor Material and Device Characterization; John Wiley & Sons: New York, NY, USA, 1998.

[217] Wang, L.; Meric, I.; Huang, P.Y.; Gao, Q.; Gao, Y.; Tran, H.; Taniguchi, T.; Watanabe, K.; Campos, L.M.; Muller, D.A.; et al. One-Dimensional Electrical Contact to a Two-Dimensional Material. Science 2013, 342, 614–617.

[218] Datta, S. Electronic Transport in Mesoscopic Systems; Cambridge University Press: Cambridge, UK, 1997.

[219] Horowitz, P.; Hill,W. The Art of Electronics; Cambridge University Press: Cambridge, 2014.

[220] Shao, Q.; Liu, G.; Teweldebrhan, D.; Balandin, A.A.; Rumyantsev, S.; Shur, M.S.; Yan, D. Flicker Noise in Bilayer Graphene Transistors. IEEE Electron. Device Lett. 2009, 30, 288–290.

[221] Kalmbach, C.-C.; Ahlers, F.J.; Schurr, J.; Müller, A.; Feilhauer, J.; Kruskopf, M.; Pierz, K.; Hohls, F.; Haug, R.J. Nonequilibrium Mesoscopic Conductance Fluctuations as the Origin of 1/f Noise in Epitaxial Graphene. Phys. Rev. B 2016, 94, 205430.

[222] Heller, I.; Chatoor, S.; Männik, J.; Zevenbergen, M.A.; Oostinga, J.B.; Morpurgo, A.F.; Dekker, C.; Lemay, S.G. Charge Noise in Graphene Transistors. Nano Lett. 2010, 10, 1563–1567.

[223] Moon, J.S.; Curtis, D.; Zehnder, D.; Kim, S.; Gaskill, D.K.; Jernigan, G.G.; Myers-Ward, R.L.; Eddy, C.R.; Campbell, P.M.; Lee, K.-M.; et al. Low-Phase-Noise Graphene FETs in Ambipolar RF Applications. IEEE Electron. Device Lett. 2011, 32, 270–272.

[224] Li, X.; Lu, X.; Li, T.; Yang,W.; Fang, J.; Zhang, G.;Wu, Y. Noise in Graphene Superlattices Grown on Hexagonal Boron Nitride. ACS Nano 2015, 9, 11382–11388.

[225] Snow, E.S.; Novak, J.P.; Lay, M.D.; Perkins, F.K. 1/f Noise in Single-Walled Carbon Nanotube Devices. Appl. Phys. Lett. 2004, 85, 4172–4174.

[226] Yasar, M.; Ede, R. K.; Kalkan, A. K. Trace Level Sulfur Sensor for Fuel Cells. ASME 2011 9th International Conference on Fuel Cell Science, Engineering and Technology 2011.

[227] Conover, J.; Husted, H.; MacBain, J.; McKee, H.; Logistics and Capability Implications of a Bradley Fighting Vehicle with a Fuel Cell Auxiliary Power Unit. SAE Technical Paper Series 2004.

[228] Patil, A. S.; Dubois, T. G.; Sifer, N. Bostic, E.; Gardner, K.; Quah, M.; Bolton, C. Portable Fuel Cell Systems for America's Army: Technology Transition to the Field. Journal of Power Sources 2004, 136 (2), 220–225.

[229] Wilberforce, T.; Alaswad, A.; Palumbo, A.; Dassisti, M.; Olabi, A. G. Advances in Stationary and Portable Fuel Cell Applications. International Journal of Hydrogen Energy 2016, 41 (37), 16509–16522.

[230] Lux, S.; Binder, M.; Holcomb, F.; Josefik, N. The DOD Residential PEM Fuel Cell Demonstration Program. Fuel Cells Bulletin 2003, 2003 (10), 11–15.

[231] Shivananju, B. N.; Yu, W.; Liu, Y.; Zhang, Y.; Lin, B.; Li, S.; Bao, Q. The Roadmap of Graphene-Based Optical Biochemical Sensors. Advanced Functional Materials 2016, 27 (19), 1603918.

[232] F. L. Meng, Z. Guo, and X. J. Huang, "Graphene-based hybrids for chemiresistive gas sensors," *TrAC Trends Anal. Chem.*, vol. 68, pp. 37–47, May 2015.

[233] Wang, T.; Huang, D.; Yang, Z.; Xu, S.; He, G.; Li, X.; Hu, N.; Yin, G.; He, D.; Zhang, L. A Review on Graphene-Based Gas/Vapor Sensors with Unique Properties and Potential Applications. *Nano-Micro Letters* 2015, *8* (2), 95–119.

[234] Mackin, C.; Fasoli, A.; Xue, M.; Lin, Y.; Adebiyi, A.; Bozano, L.; Palacios, T. Chemical Sensor Systems Based on 2D and Thin Film Materials. *2D Materials* 2020, *7* (2), 022002.

[235] Kim, K. S.; Zhao, Y.; Jang, H.; Lee, S. Y.; Kim, J. M.; Kim, K. S.; Ahn, J.-H.; Kim, P.; Choi, J.-Y.; Hong, B. H. Large-Scale Pattern Growth of Graphene Films for Stretchable Transparent Electrodes. *Nature* 2009, *457* (7230), 706–710.

[236] Bogue, R. Nanomaterials for Gas Sensing: A Review of Recent Research. *Sensor Review* 2014, *34* (1), 1–8.

[237] Chen, G.; Paronyan, T. M.; Harutyunyan, A. R. Sub-ppt Gas Detection with Pristine Graphene. *Applied Physics Letters* 2012, *101* (5), 053119.

[238] Ricciardella, F.; Vollebregt, S.; Polichetti, T.; Miscuglio, M.; Alfano, B.; Miglietta, M. L.; Massera, E.; Di Francia, G.; Sarro, P. M. Effects of Graphene Defects on Gas Sensing Properties towards NO_2 Detection. *Nanoscale* 2017, *9* (18), 6085–6093.

[239] Ben Aziza, Z.; Zhang, Q.; Baillargeat, D. Graphene/MICA Based Ammonia Gas Sensors. *Applied Physics Letters* 2014, *105* (25), 254102.

[240] Choi, H. K.; Jeong, H. Y.; Lee, D.-S.; Choi, C.-G.; Choi, S.-Y. Flexible No2Gas Sensor Using Multilayer Graphene Films by Chemical Vapor Deposition. *Carbon letters* 2013, *14* (3), 186–189.

[241] Wu, W.; Liu, Z.; Jauregui, L. A.; Yu, Q.; Pillai, R.; Cao, H.; Bao, J.; Chen, Y. P.; Pei, S.-S. Wafer-Scale Synthesis of Graphene by Chemical Vapor Deposition and Its Application in Hydrogen Sensing. *Sensors and Actuators B: Chemical* 2010, *150* (1), 296–300.

[242] Zhang, Z.; Zou, X.; Xu, L.; Liao, L.; Liu, W.; Ho, J.; Xiao, X.; Jiang, C.; Li, J. Hydrogen Gas Sensor Based on Metal Oxide Nanoparticles Decorated Graphene Transistor. *Nanoscale* 2015, *7* (22), 10078–10084.

[243] Nemade, K. R.; Waghuley, S. A. Role of Defects Concentration on Optical and Carbon Dioxide Gas Sensing Properties of SB_2O_3/Graphene Composites. *Optical Materials* 2014, *36* (3), 712–716.

[244] Nemade, K. R.; Waghuley, S. A. Highly Responsive Carbon Dioxide Sensing by Graphene/Al_2O_3 Quantum Dots Composites at Low Operable Temperature. *Indian Journal of Physics* 2014, *88* (6), 577–583.

[245] Kumar, R.; Avasthi, D. K.; Kaur, A. Fabrication of Chemiresistive Gas Sensors Based on Multistep Reduced Graphene Oxide for Low Parts per Million Monitoring of Sulfur Dioxide at Room Temperature. *Sensors and Actuators B: Chemical* 2017, *242*, 461–468.

[246] Zhang, D.; Liu, J.; Jiang, C.; Li, P.; Sun, Y. High-Performance Sulfur Dioxide Sensing Properties of Layer-by-Layer Self-Assembled Titania-Modified Graphene Hybrid Nanocomposite. *Sensors and Actuators B: Chemical* 2017, *245*, 560–567.

[247] Cuong, T. V.; Pham, V. H.; Chung, J. S.; Shin, E. W.; Yoo, D. H.; Hahn, S. H.; Huh, J. S.; Rue, G. H.; Kim, E. J.; Hur, S. H.; Kohl, P. A. Solution-Processed ZnO-Chemically Converted Graphene Gas Sensor. *Materials Letters* 2010, *64* (22), 2479–2482.

[248] Choi, S. J.; Choi, C.; Kim, S.-J.; Cho, H.-J.; Hakim, M.; Jeon, S.; Kim, I. D. Highly Efficient Electronic Sensitization of Non-Oxidized Graphene Flakes on Controlled Pore-Loaded WO_3 Nanofibers for Selective Detection of H_2S Molecules. *Scientific Reports* 2015, *5* (1).

[249] Zhou, L.; Shen, F.; Tian, X.; Wang, D.; Zhang, T.; Chen, W. Stable Cu_2O Nanocrystals Grown on Functionalized Graphene Sheets and Room Temperature H_2S Gas Sensing with Ultrahigh Sensitivity. *Nanoscale* 2013, *5* (4), 1564.

[250] Gautam, M.; Jayatissa, A. H. Detection of Organic Vapors by Graphene Films Functionalized with Metallic Nanoparticles. *Journal of Applied Physics* 2012, *112* (11), 114326.

[251] Khan, M. A.; Thomson, B.; Motayed, A.; Li, Q.; Rao, M. V. Functionalization of Gan Nanowire Sensors with Metal Oxides: An Experimental and DFT Investigation. *IEEE Sensors Journal* 2020, *20* (13), 7138–7147.

[252] Khan, M. A.; Thomson, B.; Yu, J.; Debnath, R.; Motayed, A.; Rao, M. V. Scalable Metal Oxide Functionalized Gan Nanowire for Precise SO_2 Detection. *Sensors and Actuators B: Chemical* 2020, *318*, 128223.

[253] Xu, G.; Zhang, L.; He, C.; Ma, D.; Lu, Z. Adsorption and Oxidation of NO on Various SNO_2(1 1 0) Surfaces: A Density Functional Theory Study. *Sensors and Actuators B: Chemical* 2015, *221*, 717–722.

[254] Tian, F. H.; Gong, C.; Peng, Y.; Xue, X. H_2 Sensing Mechanism under Different Oxygen Concentration on the Hexagonal WO_3 (001) Surface: A Density Functional Theory Study. *Sensors and Actuators B: Chemical* 2017, *244*, 655–663.

[255] Nah, J.; Perkins, F. K.; Lock, E. H.; Nath, A.; Boyd, A.; Myers-Ward, R. L.; Gaskill, D. K.; Osofsky, M.; Rao, M. V. Electrical and Low Frequency Noise Characterization of Graphene Chemical Sensor Devices Having Different Geometries. *Sensors* 2022, *22* (3), 1183.

[256] Kohn, W.; Sham, L. J. Self-Consistent Equations Including Exchange and Correlation Effects. *Physical Review* 1965, *140* (4A).

[257] Perdew, J. P.; Burke, K.; Ernzerhof, M. Generalized Gradient Approximation Made Simple. *Physical Review Letters* 1996, *77* (18), 3865–3868.

[258] Shao, L.; Chen, G.; Ye, H.; Wu, Y.; Qiao, Z.; Zhu, Y.; Niu, H. Sulfur Dioxide Adsorbed on Graphene and Heteroatom-Doped Graphene: A First-Principles Study. *The European Physical Journal B* 2013, *86* (2).

[259] Aarons, J.; Verga, L. G.; Hine, N. D.; Skylaris, C. K. Atom-Projected and Angular Momentum Resolved Density of States in the ONETEP Code. *Electronic Structure* 2019, *1* (3), 035002.

[260] Møller, M. F. A Scaled Conjugate Gradient Algorithm for Fast Supervised Learning. *Neural Networks* 1993, *6* (4), 525–533.

[261] G., W. R. W. *Crystal Structures*; Interscience Publishers: New York, 1966.

[262] Tamvakos, A.; Korir, K.; Tamvakos, D.; Calestani, D.; Cicero, G.; Pullini, D. No2 Gas Sensing Mechanism of ZnO Thin-Film Transducers: Physical Experiment and Theoretical Correlation Study. *ACS Sensors* 2016, *1* (4), 406–412.

[263] Waldmann, D.; Jobst, J.; Speck, F.; Seyller, T.; Krieger, M.; Weber, H. B. Bottom-Gated Epitaxial Graphene. *Nature Materials* 2011, *10* (5), 357–360.

[264] X. Liu, S. T. Cheng, H. Liu, S. Hu, D. Q. Zhang, H. S. Ning, A survey on gas sensing technology, Sensors 12 (2012) 9635–9665.

[265] J. G. Stevens, L. H. Bowen, K. M. Whatley, Moessbauer spectroscopy. Anal. Chem. 62(12), 125R–139R (1990). doi:10.1021/ac00211a003

[266] J. Janata, Chemical sensors. Anal. Chem. 64(12), 196–219 (1992). doi:10.1021/ac0 0036a012

[267] H. K. Imad, H. A. Hassan, Q. N. Abdullah, Hydrogen gas sensor based on nanocrystalline SnO_2 thin film grown on bare Si substrates. Nano-Micro Lett. 7(2), 97–120 (2015). doi:10.1007/s40820-015-0057-1

[268] G. Yang, C. Lee, J. Kim, F. Ren, S. J. Pearton, Flexible graphene- based chemical sensors on paper substrates. Phys. Chem. Chem. Phys. 15(6), 1798–1801 (2013). doi:10.1039/c2cp43717a

[269] M. R. Mohammadi, D. J. Fray, Development of nanocrystalline TiO_2-Er_2O_3 and TiO_2-Ta_2O_5 thin film gas sensors: controlling the physical and sensing properties. Sens. Actuators B 141(1), 76–84 (2009). doi:10.1016/j.snb.2009.05.026

[270] J. S. Lee, O. S. Kwon, S. J. Park, E. Y. Park, S. A. You, H. Yoon, J. Jang, Fabrication of ultrafine metal-oxide-decorated carbon nanofibers for DMMP sensor application. ACS Nano 5(10), 7992–8001 (2011). doi:10.1021/nn202471f

[271] D. Wang, A. Chen, A.K. Jen, Reducing cross-sensitivity of TiO_2-(B) nanowires to humidity using ultraviolet illumination for trace explosive detection. Phys. Chem. Chem. Phys. 15(14), 5017–5021 (2013). doi:10.1039/c3cp43454k

[272] S. Capone, A. Forleo, L. Francioso, R. Rella, P. Siciliano, J. Spadavecchia, et al., Solid state gas sensors: State of the art and future activities, J. Optoelectron. Adv. Mater. 5 (2003) 1335–1348.

[273] M. K. Patra, K. Manzoor, M. Manoth, S. C. Negi, S. R. Vadera, N. Kumar, Nano-technology applications for chemical and biological sensors, Defence Sci. J. 58(2008) 636–649.

[274] S. Sharma, M. Madou, A new approach to gas sensing with nanotechnology, Phil. Trans. R. Soc. A 370 (2012) 2448–2473.

[275] Y. Cui, Q. Q. Wei, H. K. Park, C. M. Lieber, Nanowire nanosensors for highly sensitive and selective detection of biological and chemical species, Science 293(2001) 1289–1292.

[276] C. A. Jeffrey, and C. Berger, "Highly ordered graphene for two dimensional electronics," Applied Physics Letters, vol. 89, p. 143106, Oct. 2006.

[277] E. W. Hill, A. Vijayaragahvan and K. Novoselov, IEEE Sens. J., 2011, 11, 3161–3170.

[278] R. A. Potyrailo, C. Surman, N. Nagraj and A. Burns, Chem. Rev., 2011, 111, 7315–7354.

[279] M. Pumera, A. Ambrosi, A. Bonanni, E. L. K. Chng and H. L. Poh, TrAC, Trends Anal. Chem., 2010, 29, 954–965.

[280] T. Kuila, S. Bose, P. Khanra, A. K. Mishra, N. H. Kim and J. H. Lee, Biosens. Bioelectron., 2011, 26, 4637–4648.

[281] K. S. Novoselov, A. K. Geim, S. V. Morozov, D. Jiang, M. I. Katsnelson, I. V. Grigorieva, S. V. Dubonos and A. A. Firsov, Nature, 2005, 438, 197–200.

[282] Du, X.; Skachko, I.; Barker, A.; Andrei, E. Y. Approaching Ballistic Transport in Suspended Graphene. Nat. Nanotechnol. 2008, 3, 491−495.

[283] Moseley, P. T. Solid State Gas Sensors. Meas. Sci. Technol. 1997, 8, 223−237.

[284] H. Choi, H. Y. Jeong, D. S. Lee, S. Y. Choi, C. G. Choi, Flexible NO2 Gas Sensor Using Multilayer Graphene Films by Chemical Vapor Deposition. Carbon Lett. vol. 14, pp. 186−189, 2013.

[285] A. Nourbakhsh, M. Cantoro, T. Vosch, G. Pourtois, F. Clemente, M. H. van der Veen, J. Hofkens, M. M. Heyns, S. D. Gendt, and B. F Sels, “Bandgap opening in oxygen plasma-treated graphene,” *Nanotechnology*, vol. 21, no. 43, p. 435203, Oct. 2010.

[286] J. Ito, J. Nakamura, and A. Natori, “Semiconducting nature of the oxygen-adsorbed graphene sheet,” *Appl. Phys. Lett.*, vol. 103, no. 11, pp. 113712-1–113712-5, Jun. 2008.

[287] M. Baraket, S. G. Walton, E. H. Lock, J. T. Robinson, and F. K. Perkins, “The functionalization of graphene using electron-beam generated plasmas,” *Appl. Phys. Lett.*, vol. 96, no. 23, pp. 231501-1–231501-3, Jun. 2010.

[288] Nyakiti, L. O.; Wheeler, V. D.; Garces, N. Y.; Myers-Ward, R. L.; Eddy, C. R.; Gaskill, D. K. Enabling Graphene-Based Technologies: Toward Wafer-Scale Production of Epitaxial Graphene. *MRS Bulletin* 2012, *37* (12), 1149–1157.

[289] Bancroft, W. D.; Davis, H. L. Raoult's Law. *The Journal of Physical Chemistry* 1929, *33* (3), 361–370.

[290] H. J. Yoon, D. H. Junb, J. H. Yanga, Z. Zhouc, and S. S. Yangb, "Carbon dioxide gas sensor using a graphene sheet," *Sens. Actuators B, Chem.*, vol. 157, no. 1, pp. 310–313, Sep. 2011.

[291] T. O. Wehling *et al.*, "Molecular doping of graphene," *Nano Lett.*, vol. 8, no. 1, pp. 173–177, Dec. 2008.

[292] O. Leenaerts, B. Partoens, and F. M. Peeters, "Paramagnetic adsorbates on graphene: A charge transfer analysis," *Appl. Phys. Lett.*, vol. 92, Mar. 2008, Art. no. 243125.

[293] O. Leenaerts, B. Partoens, and F. M. Peeters, "Adsorption of small molecules on graphene," *Microelectron. J.*, vol. 40, pp. 860–862, Apr. 2009.

[294] G. Lu *et al.*, "Toward practical gas sensing with highly reduced graphene oxide: A new signal processing method to circumvent run-to-run and device-to-device variations," *ACS Nano*, vol. 5, no. 2, pp. 1154–1164, Jan. 2011.

[295] S. G. Chatterjee, S. Chatterjee, A. K. Ray, and A. K. Chakraborty, "Graphene–metal oxide nanohybrids for toxic gas sensor: A review," *Sens. Actuators B, Chem.*, vol. 221, pp. 1170–1181, Dec. 2015.

[296] S. S. Varghese, S. Lonkar, K. K. Singh, S. Swaminathan, and A. Abdala, "Recent advances in graphene based gas sensors," *Sens. Actuators B, Chem.*, vol. 218, pp. 160–183, Oct. 2015.

[297] T. Wagner, S. Haffer, C. Weinberger, D. Klaus, and M. Tiemann, "Mesoporous materials as gas sensors," *Chem. Soc. Rev.*, vol. 42, no. 9, pp. 4036–4053, 2013.

[298] C. Li, G. Shi, Three-dimensional graphene architectures. Nanoscale, vol. 4, no. 18, pp. 5549–5563, 2012.

[299] G. Yang, C. Lee, J. Kim, F. Ren, S. J. Pearton, Flexible graphene-based chemical sensors on paper substrates. Phys. Chem. Chem. Phys, vol. 15, no. 6, pp. 1798–1801, 2013.

[300] Z. Chen, J. Appenzeller, J. Knoch, Y.M. Lin, P. Avouris, The role of metal-nanotube contact in the performance of carbon nanotube field-effect transistors. Nano Lett, vol. 5, no. 7, pp. 1497–1502, 2005.

[301] W. J. Yuan, G. Q. Shi, Graphene-based gas sensors. J. Mater. Chem. A, vol. 1, no. 35, pp. 10078–10091, 2013, doi:10.1039/C3ta11774j.

[302] T. Seiyama, A. Kato, K. Fujiishi, M. Nagatani, A new detector for gaseous components using semiconductive thin films. Anal. Chem, vol. 34, no. 11, pp. 1502–1503, 1962, doi:10.1021/ac60191a001.

[303] P.J. Shaver, Activated tungsten oxide gas detectors. Appl. Phys. Lett, vol. 11, no. 8, pp. 255, 1967. doi:10.1063/1.1755123.

[304] R. Burdett, "Amplitude Modulated Signals - The Lock-in Amplifier". Handbook of Measuring System Design (Wiley). ISBN 978-0-470-02143-9, 2005.

[305] Meade M L. Lock-in Amplifiers: Principles and Applications. Peter Peregrinus Ltd; 1983.

[306] Lock-in amplifiers and pre-amplifiers. Princeton Appl Res Corp Data Sheets; 1971.

[307] Lock-in amplifiers, Appl Notes. Stanford Res Sys Data Sheets; 1999.

[308] Zurich Instruments, “Lock-in amplifiers,” 2016. [Online]. Available: www.zhinst.com/

[309] Anfatec Instruments, “Lock-in amplifiers,” 2014. [Online]. Available: www.anfatec.de/index.html

[310] Stanford Res. Syst., “Lock-in amplifiers,” 2017. [Online]. Available: www.thinksrs.com/

[311] P. M. Maya Hernandez, M. T. Sanz Pascual, and B. Calvo, “Micropower CMOS lock-in amplifier for portable applications,” *Electron. Lett.*, vol. 52, no. 10, pp. 828–830, 2016.

[312] G. Gervasoni, M. Carminati, and G. Ferrari, “A general purpose lock-in amplifier enabling sub-ppm resolution,” *Procedia Eng.*, vol. 168, pp. 1651–1654, 2016.

[313] D. Garcia-Romeo, M. R. Valero, N. Medrano, B. Calvo, and S. Celma, “A high performance LIA-based interface for battery powered sensing devices,” *MDPI Sensors*, vol. 15, pp. 25260–25276, 2015.

[314] 2019. [Online]. Available: http://www.resistorguide.com/wirewound-resistor/

[315] 2019. [Online]. Available: https://www.analog.com/media/en/technical documentati -on /data-sheets/6657fd.pdf

[316] Palumbo G., Pennini S., Filter circuits synthesis with CFOA based differentiators. Proc. of the IMAC'99, vol. 1, pp. 546-550, 1999.

[317] Martínez P.A, Sabadell J., Aldea C., Celma S., Variable frequency sinusoidal oscillators based on CCII+. IEEE Trans. Circuits and Systems I, vol. 46, no. 11, pp. 1386-1390, 1999.

[318] Tielo-Cuautle, E., Sanchez-Lopez, C., Moro-Frias, D. Symbolic analysis of (MO) (I) CCI (II) (III)-based analog circuits. International Journal of Circuit Theory and Applications, vol. 38, no. 6, pp. 649-659, 2010.

[319] Ahmed M. Soliman. "Two integrator loop quadrature oscillators: A review". Journal of Advanced Research, vol. 4, pp. 1–11, 2013.

[320] Maya-Hernandez, P. M., Sanz-Pascual, M. T. and Calvo, B.,"A 1.8V–0.18μm CMOS lock-in amplifier for portable applications", IEEE International Symposium on Circuits and Systems (ISCAS), 2012.

[321] D'Amico, A., De Marcellis, A., DiCarlo, C., Di Natale, C., Ferri, G., Martinelli, E., Paolesse R. and Stornelli, V., "Low-voltage low-power integrated analog lock-in amplifier for gas sensor applications", Sensors and Actuators, vol. 44, no. 2, pp. 400-406, 2008.

[322] Gnudi, A., Colalongo, L. and Baccarani, G., "Integrated lock-in amplifier for sensor applications", IEEE Solid-State Circuits Conference (ESSCIRC), pp. 58-61, 1999.

[323] 2011. [Online]. Available:https://www.analog.com/media/en/technical-documentation/data-sheets/AD620.pdf

[324] 2011. [Online]. Available: http://www.ti.com/lit/ds/slos525/slos525.pdf

[325] 2019. [Online]. Available:https://www.analog.com/media/en/technical-documentation/data-sheets/AD8220.pdf

[326] 2010. [Online]. Available:https://www.analog.com/media/en/technical-documentation/data-sheets/AD8553.pdf

[327] 2012. [Online]. Available:https://www.analog.com/media/en/technical-documentation/data-sheets/AD8675.pdf

[328] 2017. [Online]. Available: https://www.analog.com/media/en/technical-documentation/data-sheets/AD8429.pdf

[329] 2017. [Online]. Available: https://www.ti.com/lit/ds/symlink/opa27.pdf

[330] D. P. Blair, “Phase sensitive detection as a means to recover signals buried in noise”, J. Phys E: Sci. Instrum. vol. 8, 1975.

[331] J. Xu, G. Meynants, P. Merken, “Low-power lock-in amplifier for complex impedance measurement”, in Proc. 3rd Int. Workshop on Advances on sensors and interfaces, pp. 110-114, 2009.

[332] U. Marschner, H. Gratz, B Jettkant, D. Ruwisch, G. Woldt, W. J. Fischer, B. Clasbrummel, “Integration of a wireless lock-in measurement of hip prosthesis vibrations for loosening detection”, in Proc. Eurosensors 2008, pp. 789-792, Dresden, 2008.

[333] Wolfson, R. Am. J. Phys, vol. 59, pp. 569–572, 1991.

[334] Horlick, G.; Betty, K. R. Anal. Chem., vol. 47, pp. 363–366, 1975.

[335] Temple, P. A. Am. J. Phys, vol. 43, pp. 801–807, 1975.

[336] J. L. Guinon, et al, Lock-in amplifier response simulation using Mathcad, *Dept. of Ingenieria Quimicay Nuclear, University of Spain*.

[337] Darren Wenn, Implementing digital lock-in amplifiers using the dsPIC DSC, *Application Note 1115, Microchip Technology Inc.,* 2007.

[338] M. Song and F. Liu, “Design and Implementation of the phase-locked amplifier”, international journal of signal processing, vol. 8, no. 5, pp. 231-238, 2015

[339] Low Cost Analog Multiplier - AD633, 2015. [Online]. Available: https://www.analog.com/media/en/technical-documentation/data-sheets/AD633.pdf

[340] G. de Graaf and R. F. Wolffenbuttel, "Lock-in amplifier techniques for low-frequency modulated sensor applications," *2012 IEEE International Instrumentation and Measurement Technology Conference Proceedings*, Graz, 2012, pp. 1745-1749. doi: 10.1109/I2MTC.2012.6229510

[341] A. D. Marcellis, E. Palange, N. Liberatore, and S. Mengali, “Low-cost portable 1 MHz lock-in amplifier for fast measurements of pulsed signals in sensing applications”, IEEE Sensor Letters, vol. 1, no. 4, 2017.

[342] P. K. Dash and S. Hasan, “A fast recursive algorithm for the estimation of frequency, amplitude, and phase of noisy sinusoid,” *IEEE Trans. Ind. Electron.*, vol. 58, no. 10, pp. 4847–4856, Oct. 2011.

[343] M. R. Nabavi and S. Nihtianov, “Eddy-current sensor interface for advanced industrial applications,” *IEEE Trans. Ind. Electron.*, vol. 58, no. 9, pp. 4414–4423, Sep. 2011.

[344] P. R.Gray, P. J. Hurst, S. H. Lewis, and R.G.Meyer, *Analysis and Design of Analog Integrated Circuits*, 4th ed. Hoboken, NJ, USA: Wiley, 2001.

[345] PSPICE user’s guide [2000]. Available: https://www.seas.upenn.edu/~jan/spice/PSpice_UserguideOrCAD.pdf

[346] 2016. [Online]. Available: https://www.analog.com/media/en/technical-documentation/data-sheets/AD630.pdf

[347] 2020. [Online]. Available: https://www.electronics-tutorials.ws/opamp/op-amp-multivibrator.html

[348] 2020. [Online]. Available: https://webench.ti.com/filter-design-tool/filter-type

[349] R. P. Sallen and E. L. Key, "A practical method of designing RC active filters," in *IRE Transactions on Circuit Theory*, vol. 2, no. 1, pp. 74-85, March 1955.

[350] 2002. [Online]. Available: http://www.ti.com/lit/an/sloa024b/sloa024b.pdf, “Analysis of the Sallen-key Architecture”

[351] “Pink Noise Generator for Audio Testing”, R. Elliot, Elliot Sound Products, 1999; https://sound-au.com/project11.htm; retrieved 5/12/2020

BIOGRAPHY

JongBong Nah received the B.S. degree in Electrical & Computer Engineering from George Mason University, Fairfax, VA, USA, and the M.S. degree in Electrical & Computer Engineering from Old Dominion University, Norfolk, VA, USA, in 2012. He is currently pursuing the Ph.D. degree at the Electrical & Computer Engineering, George Mason University, Fairfax VA, USA. His current research interests include epitaxial graphene-based electronic sensors, functionalization of graphene, and low frequency noise for characterization and fluctuation sensing.